



저작자표시-비영리-변경금지 2.0 대한민국

이용자는 아래의 조건을 따르는 경우에 한하여 자유롭게

- 이 저작물을 복제, 배포, 전송, 전시, 공연 및 방송할 수 있습니다.

다음과 같은 조건을 따라야 합니다:



저작자표시. 귀하는 원저작자를 표시하여야 합니다.



비영리. 귀하는 이 저작물을 영리 목적으로 이용할 수 없습니다.



변경금지. 귀하는 이 저작물을 개작, 변형 또는 가공할 수 없습니다.

- 귀하는, 이 저작물의 재이용이나 배포의 경우, 이 저작물에 적용된 이용허락조건을 명확하게 나타내어야 합니다.
- 저작권자로부터 별도의 허가를 받으면 이러한 조건들은 적용되지 않습니다.

저작권법에 따른 이용자의 권리는 위의 내용에 의하여 영향을 받지 않습니다.

이것은 [이용허락규약\(Legal Code\)](#)을 이해하기 쉽게 요약한 것입니다.

[Disclaimer](#)

공학박사 학위논문

**Asymmetric photonic mode
conversion in waveguides and
metasurfaces**

도파로와 메타표면에서의

비대칭 광모드 변환

2017년 2월

서울대학교 대학원

전기·컴퓨터공학부

김 준 수

Abstract

Asymmetric photonic mode conversion in waveguides and metasurfaces

Joonsoo Kim

Department of Electrical Engineering and Computer Science

College of Engineering

Seoul National University

In this dissertation, asymmetric characteristics of photonic mode conversion structures in waveguides and metasurfaces have been discussed. More specifically, I propose design schemes for i) adjustment of mode conversion asymmetry in tri-mode waveguide system, ii) compact unidirectional mode converter in plasmonic waveguide and iii) unidirectional scattering of polarization-converted wave from bilayer metasurface.

Firstly, a Lorentz reciprocal mode conversion asymmetry in reflectionless tri-mode waveguide system with weak waveguide gratings is discussed. In particular, the dark-mode which is the photonic analogue of atomic dark-state has been exploited for independent design of forward and backward direction characteristics. Due to the stationary property of the dark-mode, the mode conversion characteristics in one propagation direction could be fixed regardless of the length of the grating that defines the dark-mode. By carefully selecting the dark-mode and the length of the waveguide grating, the mode conversion asymmetry could be controlled.

Secondly, a compact spatial plasmonic mode converter with unidirectional mode conversion characteristics is proposed. By combining mode-selective blockers with simple stub mode converter, unidirectional mode conversion characteristics could be achieved. Furthermore, it was found

that the redundant scattering and the backward reflection can be completely eliminated by mode filtering and destructive interference, respectively. An application of the design strategy using the mode-selective blockers is also presented for the problem of near-complete out-coupling from subwavelength nanoslits.

Lastly, a bilayer metasurface which transmits polarization converted signal only to the forward direction is proposed. The bilayer metasurface was designed by assembling two identical thin metasurfaces, the property of which is well-known. After numerical design of the bilayer metasurface, the designed structure was fabricated and its transmission and reflection characteristics were measured. It was found that the reflectance of the fabricated structure is successfully suppressed. The issue of amplitude distortion and its compensation is discussed and experimentally verified.

The results on the dark-mode based asymmetric conversion device offer a method to control the transmission asymmetry and this capability can pave a way to actively tunable asymmetry of optical systems. Furthermore, by using mode selective blockers, asymmetric mode converters can be constructed in a compact form which is suitable for nanophotonic applications. The bilayer metasurface can be easily extended to the reflection-type and the multiplexing of transmitted signal and reflected signal can be made possible by making a supercell of a transmission-type cell and a reflection-type cell. This opens a new way of metasurface function multiplexing.

Keywords: Photonic mode converter, waveguide, metasurface, Lorentz reciprocity, asymmetric mode conversion, reflection cancellation, multiplexing, polarization

Student Number: 2012-20755

Contents

Abstract	i
Contents	iii
List of Tables	vi
List of Figures	vii
Chapter 1 Introduction	1
1.1 Overview	1
1.1.1 Asymmetric transmission characteristics in multimode systems	2
1.1.2 Metasurfaces	6
1.2 Motivation and organization of this dissertation	9
Chapter 2 Adjustment of waveguide mode conversion asymmetry by using photonic dark-states	13
2.1 Introduction	13
2.1.1 Asymmetric transmission in tri-mode waveguide system allowed by Lorentz reciprocity	13
2.1.2 Photonic analogue of dark-state in coupled-mode theory	14
2.2 Designed asymmetry by using dark-modes	16
2.3 Specification of dark-mode	21
2.4 Asymmetric mode conversion by cascaded gratings	25
2.5 Conclusion	33
Chapter 3 Compact plasmonic spatial mode converter with mode conversion asymmetry	34
3.1 Introduction	34
3.1.1 Asymmetric spatial mode converters in waveguides	34
3.1.2 Mode conversion by using mode-selective blocking filters	35
3.2 Plasmonic spatial mode conversion by using a stub mode converter	37
3.2.1 Dispersion relation of the plasmonic waveguide	37

3.2.2 Stub mode converter	39
3.3 Asymmetric mode conversion by using spatial mode filters	44
3.3.1 Configuration of the proposed structure	44
3.3.2 Design of the anti-symmetric mode barrier (F2)	45
3.3.3 Design of the notch filter (F1)	47
3.3.4 Unidirectional mode conversion characteristics of the whole structure.....	50
3.4 Tuning of the mode-selective cavity for idle scattering component elimination.....	51
3.4.1 Modelling of the mode-selective cavity and optimization conditions	51
3.4.2 Cavity length optimization.....	54
3.5 Application of the design strategy to out-coupler design problem....	56
3.5.1 Scattering components at the end of nanoslit	56
3.5.2 Trench-type antenna near nanoslit and its working principle.....	57
3.5.3 Design of the SPP blocking trench	60
3.5.4 Radiation pattern from the optimized structure.....	63
3.6 Conclusion.....	66
Chapter 4 Unidirectional launching of polarization-converted waves from bilayer metasurfaces	67
4.1 Introduction	67
4.1.1 Properties of thin, single layer metasurfaces and the symmetry of scattering characteristics	67
4.1.2 Multiplexing of the transmitted and reflected wavefronts	70
4.2 Numerical design	72
4.2.1 Configuration of the bilayer metasurface and reduction into a single layer metasurface design problem	72
4.2.2 Unit cell structure and gap distance optimization.....	75
4.2.3 Effective material parameter point of view	78

4.2.4 Amplitude distortion and its compensation.....	79
4.3 Experiment	82
4.3.1 Fabrication and experimental setup	82
4.3.2 Antenna resonance condition specification.....	85
4.3.3 Transmission and reflection characterization	87
4.3.4 Amplitude distortion and its reduction by polarization basis change	90
4.4 Conclusion.....	92
Chapter 5 Summary.....	93
Bibliography.....	96
Appendix	105
초 록	106

List of Tables

Table 1.1 Cases of Lorentz reciprocal transmission/reflection asymmetry.....	8
--	---

List of Figures

Figure 1.1 (a) Optical isolation via time-dependent permittivity [1]. (b) Time-varying cavity for optical isolation [3]. (c) Integrated magneto-optic optical isolator [6]. (d) Optical isolation by using optical nonlinearity [5].	3
Figure 1.2 Asymmetric polarization conversion characteristics of metasurface (a) in the linear polarization basis [15] and (c) circular polarization basis [22]. (c) Asymmetric power transmission through hyperbolic metamaterial sandwiched by diffraction gratings [30]. (d) Asymmetric mode conversion in PT symmetric grating [7].	5
Figure 1.3 (a) Nanoantennas with designed scattering characteristics and planar lens constructed by arranging nanoantennas [45]. (b) Concept of geometric metasurface [46]. (c) Function multiplexed metasurface [48].	7
Figure 1.4 Organization of this dissertation.	12
Figure 2.1 (a) A schematic of the proposed device. A silicon waveguide ($\epsilon_{\text{Si}} = 12.15$) of width $w_1 = 400$ nm and a SiO_2 waveguide ($\epsilon = 2.25$) of width $w_2 = 400$ nm are aligned in parallel with an air gap of width $g = 100$ nm. The half-infinite areas above the waveguide II and beneath the waveguide I are set to air. (b) When mode 1 is incident from the left, the grating α converts mode 1 to the dark-mode at the grating β and the dark-mode appears at the output because the dark-mode is stationary in the grating β . (c) When mode 1 is incident from the right, mode transitions in the grating β is not prohibited. As a result, various linear combinations of mode 1, 2 and 3 can appear at the output.	17
Figure 2.2 (a) The dispersion relations of three modes considered in my configuration. The widths of two waveguide are adjusted so that	

$\Delta k_{23} \approx \Delta k_{12}$ for simultaneous coupling of modes. Normalized power flow inside the grating β when (b) $\Lambda_\beta = 1530$ nm and (c) $\Lambda_\beta = 1550$ nm. Electric field (E_y) distribution inside the grating β when (d) $\Lambda_\beta = 1530$ nm and (e) $\Lambda_\beta = 1550$ nm.23

Figure 2.3 (a) Normalized power flow in the grating β when the dark-mode is launched. (b) E_y field distribution of the dark-mode in the grating β . Normalized power flow of mode 3 in grating β when there is (c) a variation of normalized input power flow of mode 3 ($P_{3,in}$) and (d) a variation of relative phase of mode 3 ($\Delta\phi$) with respect to the exact dark-mode condition at the entrance of grating β25

Figure 2.4 (a) Normalized power flow inside the grating α tuned for the transition from mode 1 to 3. (b) Normalized power flow through two cascaded gratings when a wrong value of D is chosen ($D = 5.6$ μm). (c) Normalized power transmission after the two cascaded gratings depending on D . The length of the grating β is 40 periods. (d) Normalized power flow inside two cascaded gratings when $D = 5.25$ μm27

Figure 2.5 (a) Normalized power flows for the right-to-left propagation case. (b) Normalized power flows inside the grating β for the case of mode 1 incidence. Normalized power flows when the length of the grating β is set to 11 periods (c) for the left-to-right and (d) right-to-left propagation cases. (e) and (f) are those for the 16 periods long grating β29

Figure 2.6 E_y field distributions when the length of the grating β is set to 11 periods (a) for left-to-right and (b) right-to-left propagation cases. (c) and (d) are those when the length of the grating is set to 16 periods.32

Figure 3.1 Unidirectional reflection of plasmonic waveguide mode by asymmetrically configured stub structures [11].	35
Figure 3.2 Abstract illustration of 4-port mode converter when the input mode is incident from (a) port 1 (left) and (b) port 1' (right).	36
Figure 3.3 (a) Schematic of the silver-silicon-silver plasmonic waveguide. Dispersion relations for the plasmonic waveguide when the width of the waveguide (w) is (a) 200 nm, (b) 180 nm and (c) 400 nm. The solid blue and red lines represent the symmetric and the anti-symmetric modes. The black dashed line represent the light line of the silicon and the yellow, purple lines represent the photonic modes.	38
Figure 3.4 (a) Schematic of the stub mode converter. (b) Mode conversion at the boundary of the stub structure. Transmittance in the forward direction (t_{ij}) and reflectance in the backward direction (r'_{ij}) for the stub boundary.	40
Figure 3.5 Illustration of mode conversion pathways, one of which is (a) non-resonant and the other one is (b) resonant. (c) Transmittance products which show relative contribution of two pathways to mode conversion. (d) Mode conversion efficiency depending on the width of the stub where the depth of the stub is fixed to 70 nm.	42
Figure 3.6 Transmission of the symmetric mode when the anti-symmetric mode is launched to the stub converter. (b) $ H_y $ distribution for the mode conversion stub when the anti-symmetric mode is incident from the left.	43
Figure 3.7 The schematic of the proposed mode converter. The MIM anti-symmetric mode is incident from the left. For material parameters, we used $\epsilon_{Ag} = -122 + 2.83i$ [65] (at $\lambda = 1550$ nm), $\epsilon_{Si} = 12.15$ and $\epsilon_{silica} = 2.25$.	45
Figure 3.8 Dispersion relations of plasmonic waveguides with silicon and silic	

a core. Solid blue and red lines represent the symmetric and the anti-symmetric modes for silicon core and the dashed blue and red lines represent ones for the silica core (cut-off frequency of the anti-symmetric mode for the silica core waveguide is shifted to 1.68 eV). The dashed black lines are the light lines for the silica and the silicon The solid yellow line represents the photonic TM mode for the silicon core. Transmission (solid line) and reflection (dashed line) of the F2 for (b) the symmetric and (c) the anti-symmetric mode incidence.	46
Figure 3.9 Power transmission map of the notch filter for (a) the symmetric mode and (b) the anti-symmetric mode incidence. $ H_y $ distributions for the optimized notch filter when (c) the symmetric and (d) the anti-symmetric mode is incident from the left.	47
Figure 3.10 (a) Power transmission and (b) absorption of the notch filter when $w_n = 150$ nm. (c) Power transmission and (d) absorption of the notch filter when $w_n = 240$ nm. Solid blue and red lines represent the cases for the symmetric mode and the anti-symmetric mode incidence, respectively.	48
Figure 3.11 $ H_y $ distributions for the optimized notch filter when (a) the symmetric and (b) the anti-symmetric mode is incident from the left.	49
Figure 3.12 $ H_y $ field distributions for the cases when the symmetric mode is incident from the left (upper left) and right (upper right). Those for anti-symmetric mode incidence is shown in the lower left and lower right of the figure, respectively.	50
Figure 3.13 Block representation of the proposed mode converter. The layer 1 includes F1, region α and the stub while the layer 2 is the same as F2. Due to the mode-selective transmission characteristics of F1 and F2, the reflection of the symmetric mode	

and the transmission of the anti-symmetric mode are not expressed.....	52
Figure 3.14 (a) Schematic of the layer 1 and major terms which contribute to r_{aa} . (b) $ r_{aa} ^2$ and corresponding (c) $f(L_a)$ depending on L_a	54
Figure 3.15 (a) Reflected power of the anti-symmetric mode for the whole structure as a function of L_β . (b) $ H_y $ field distribution for the optimized structure when the anti-symmetric mode is incident from the left.....	55
Figure 3.16 (a) Scattering at the end of nano-slit when MIM plasmonic mode is launched from the bottom ($\epsilon_{Ag} = -17.3 + 0.193i$, $\epsilon_{silica} = 2.25$). The scattered wave can be decomposed into free space modes, SPP mode and backward reflection. (b) Dependence of power proportion for each scattered wave component.....	57
Figure 3.17 (a) Schematic diagram of the proposed structure. MIM plasmonic mode is launched from the bottom. (b) Schematic depiction of the scattering coefficients at the exit of the nano-slit and the trench. (c) Multiple reflections that occur inside the cavity formed by the trench structures.....	58
Figure 3.18 (a) The reflection ($ \gamma_0 ^2$, solid line) and the SPP coupling ($2 \kappa ^2$, dashed line) at the exit of nano-slit without the trenches. (b) The h dependence of the target reflectance ($ r_0 $, solid line) calculated by Eq. (2) and the SPP reflectance ($ r $, dashed line) at the trench when $ t \approx 0$ is satisfied.....	61
Figure 3.19 Two routes for SPP transmission through the trench structure (a) the free space route and (b) the trench cavity route. κ_{step} , t_{step} and r_{step} represent scattering coefficients at the edge of the trench. SPP transmittance as a function of trench length L when the depth of the trench is fixed at (c) $d = 30$ nm and (d) $d = 50$ nm. The solid black line represents SPP transmittance of the trench and the	

dashed red line represents the theoretical fitting of the trench cavity route.....	62
Figure 3.20 (a) Normalized power flows of the reflection (solid line) and SPP leakage (dashed line) varying with the trench position (Δx). $ H_y $ field distributions when (b) the trenches are removed from the optimized structure, and for the two optimized cases when (c) $\Delta x = 300$ nm and (d) $\Delta x = 530$ nm.....	64
Figure 4.1 (a) Schematic of a thin metasurface where polarization eigenmode is incident from the bottom. Areas of realizable (b) transmittance, reflectance and (c) scattering amplitude for 50 nm-thick Au film at the wavelength of 980 nm.	69
Figure 4.2 (a) Thin metasurface surrounded by heterogeneous materials where LCP is incident from the bottom. The polarization converted components are emitted in asymmetric fashion. (b) Realizable transmittance and reflectance for silica-Au (50 nm)-air configuration at the wavelength of 980 nm.....	70
Figure 4.3 (a) Multiplexing scheme using transmission type (T-type) cells and reflection type (R-type) cells. (b) Schematic of the metallic bilayer based T-type cell and the R-type cell.....	71
Figure 4.4 Schematic of the proposed bilayer metasurface. (a) The bilayer metasurface should be designed to emit right-circular polarized light (RCP) only in the upward direction when left-circular polarized (LCP) light is incident from the bottom. (b) Unit cell structure of the bilayer metasurface.....	72
Figure 4.5 (a) Parametrization of the reflectance which covers region of realizable reflectances. (b) It can be found that the reflectance of single layer metasurface should be placed close to the green line. The maps for (c) ρ_y and (d) ϕ_y as functions of ρ_x and ϕ_x	74
Figure 4.6 Conceptual diagrams of single layer design procedure.	76

Figure 4.7 Transmittance (blue) and reflectance (red) (a) trajectories on complex plane and (b) the graph of normalized power. Normalized power flow of the cross-polarization component for the bilayer metasurface.	77
Figure 4.8 (a) Schematic diagram when the metasurface is modeled as a metamaterial slab. Effective (b) refractive index and (c) wave impedance of the bilayer structure when $L_1 = L_2 = L_3 = L$	78
Figure 4.9 (a) Schematic of the unit cell structure with rotated anisotropic antenna. (b) Amplitude distortion of the designed metasurface. (c), (d) Amplitude and (e), (f) phase (unwrapped) of the transmittance and reflectance matrix elements. Blue, red, black lines represent the cases $i=j=x$, $i=j=y$, $i=x, j=y$, respectively.	80
Figure 4.10 (a) Aperture antenna under elliptically polarized light incidence. (b) Reflected power flow of cross-polarization component. The blue, red and black lines represent the cases $e = 0.1$, $e = 0.5$ and $e = 0.9$, respectively.	82
Figure 4.11 Fabricated nanoaperture array of 48 by 48 unit cells.	83
Figure 4.12 Schematic and actual realization of experimental setup for measurement of transmitted and reflected signal. The position of IRCCD and polarization filter at the detecting end are switched depending on the type of measurement.	84
Figure 4.13 FIB image of the fabricated sample. Antenna length condition is varied from 300 nm to 540 nm and 4 copies have been fabricated for averaging.	85
Figure 4.14 (a) Focused laser beam and the fabricated sample. Light from the fabricated antenna array came from white light source illuminated from the behind of the sample. (b) Dark images of the fabricated antenna array.	86
Figure 4.15 CCD images when the focused optical beam is aligned to the	

antenna array with the fabrication condition (a) $L_1 = 300$ nm and (b) $L_1 = 480$ nm. (c) Reflection that depends on the aperture antenna length L_1	87
Figure 4.16 Fabricated 40 by 40 array of nanoantennas. Anisotropic antenna tilt distribution is given to induce anomalous refraction.	88
Figure 4.17 Transmitted image of the 40 by 40 cell array when (a) no polarization filtering components are placed and (b) when a linear polarizer and a quarter wave plate is placed in front of IRCCD camera.	88
Figure 4.19 Fringe patterns of cross-polarized reflection when the quarter wave plate in front of laser source is rotated.	91

Chapter 1 Introduction

1.1 Overview

In linear optics, any electromagnetic fields can be expressed as linear combinations of electromagnetic fields of different frequencies, spatial distributions and polarizations. Often, it is convenient to employ eigenmodes of symmetry transformations such as translation or rotation as basis fields since they are invariant under symmetry transformations and can be labelled by the eigenvalues that implies their nature. For instance, plane waves and waveguide modes are eigenmodes of translation and optical vortices can be viewed as eigenmodes of rotation. The eigenvalues for translation show the linear momenta or propagation constants while those for rotation show the angular momenta or topological charges of optical fields. When symmetry is perturbed in the path of light propagation, the eigenmodes couple each other to exhibit modal transition behaviors. In the optical mode point of view, optical components can be regarded as symmetry-breaking obstacles that cause optical mode transitions.

When there are only few optical modes to be considered, modal transitions by optical components can be designed sophisticatedly to reveal intriguing coherent interactions. Such components include couplers which have single mode waveguide ports, multimode waveguide systems, subwavelength period antenna arrays which do not generate multiple

diffraction orders and so on. Particularly, it has been found that mode conversion phenomena are related to the asymmetry of optical transmission and reflection which provoked controversy on optical isolation. Besides theoretical interest regarding unidirectional optical power transmission, control of transmission/reflection asymmetry can also be useful for practical purposes such as directional optical function multiplexing. In the following subsections, I will firstly introduce asymmetric transmission characteristics in various multimode systems. Then, the metasurfaces which can be regarded as a practical example of few-mode system will be introduced. The issues that I would like to address in this dissertation will be put forward in the next section of this chapter.

1.1.1 Asymmetric transmission characteristics in multimode systems

Unidirectional propagation of light has been attracting many researchers largely due to the importance of optical isolation and interesting analogy with electrical diodes. Due to the Lorentz reciprocity theorem which states the amplitude of scattering from port A to port B is the same as the one from port B to port A, optical isolation is prohibited in non-magnetic, passive linear systems. Therefore, in the strict sense, optical isolator must violate at least one condition for Lorentz reciprocity. For instance, most common optical isolators exploit magneto-optic effect to violate non-magnetic condition. In recent years, novel nanophotonic structures with non-reciprocal light propagation characteristics have been proposed and massive amount of subsequent researches have followed. Yu and his colleagues have shown that

active permittivity perturbation can induce non-reciprocal waveguide mode conversion and the concept has been experimentally verified [1, 2]. More recently, Alù proposed an appealing way to reduce the footprint of the active optical isolator by using a ring resonator which signifies the potential for practical uses [3, 4]. On the other hand, optical nonlinearity has also been exploited to realize unidirectional light propagation in the integrated photonic waveguides, which opens a way to non-magnetic passive optical isolation [5].

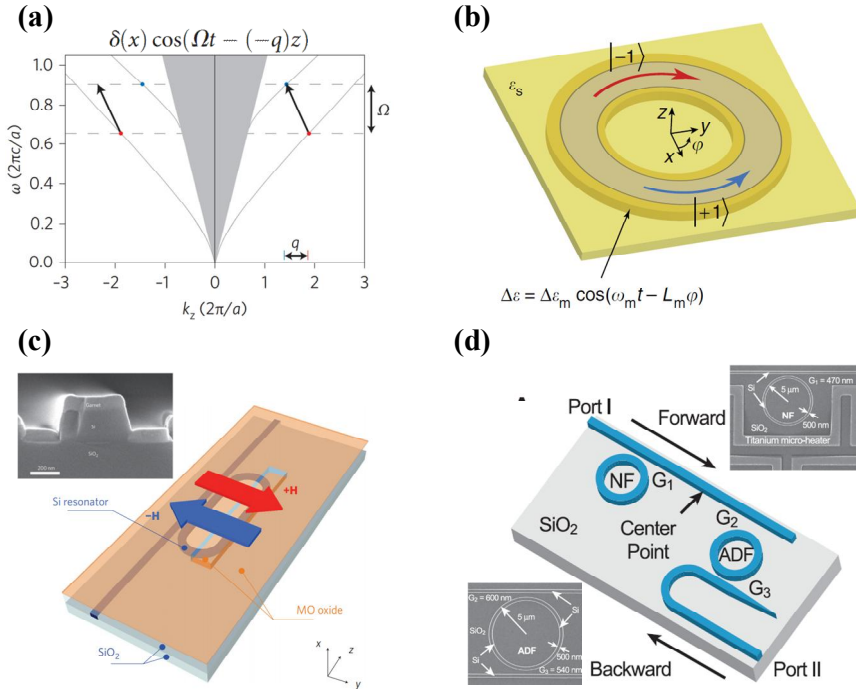


Figure 1.1 (a) Optical isolation via time-dependent permittivity [1]. (b) Time-varying cavity for optical isolation [3]. (c) Integrated magneto-optic optical isolator [6]. (d) Optical isolation by using optical nonlinearity [5].

Besides the photonic modes with inherent unidirectionality and truly Lorentz non-reciprocal devices using magneto-optic effect, time-dependent modulation or optical nonlinearity, several Lorentz reciprocal optical structures which exhibit unidirectional light transmission have been reported [7-40]. Though such structures cannot be used for optical isolation, unidirectional optical power transmission via asymmetric mode transition in multimode system is possible without violating Lorentz reciprocity. Figure 1.2 and Table 1.1 show the examples of mode conversion structures with asymmetric transmission characteristics.

Asymmetric mode conversion is often achieved by using asymmetric configuration of cascaded structures. Since light passes through the cascaded layers in different orders depending on the incident direction, asymmetric configuration generally results in asymmetric mode conversion characteristics. For example, multilayered planar metallic nanostructures shown in Fig. 1.2(a) and 1.2(b) are found to exhibit asymmetric polarization conversion characteristics for both linear polarization [15] and circular polarization [22], respectively. For asymmetric optical power transmission characteristics, metal-dielectric stack (hyperbolic metamaterial) sandwiched by gratings with different periods have been proposed. Non-cascaded photonic mode converters with asymmetric mode conversion characteristics also exist. Especially, parity-time symmetric (PT symmetric) complex permittivity gratings are found to exhibit unidirectional mode conversion under special design condition which corresponds to the eigenvalue transition point of the PT symmetric mode-coupling matrix. [7, 8]. Surprising connection between unidirectionality in photonic structures and

eigenvalue phase transition of PT symmetric transition attracted many researchers and extension to various aspects of optics including nonlinear optics and imaging have followed [42, 43].

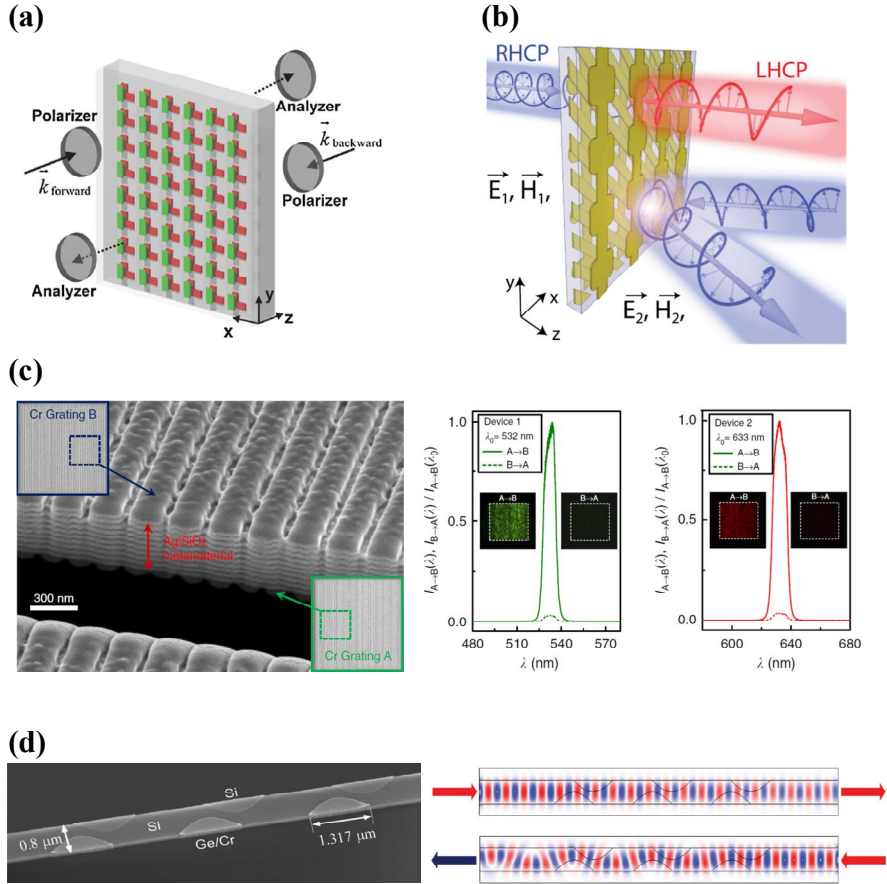


Figure 1.2 Asymmetric polarization conversion characteristics of metasurface (a) in the linear polarization basis [15] and (c) circular polarization basis [22]. (c) Asymmetric power transmission through hyperbolic metamaterial sandwiched by diffraction gratings [30]. (d) Asymmetric mode conversion in PT symmetric grating [7].

1.1.2 Metasurfaces

Optical metamaterials refer to artificial materials, which are generally composed of subwavelength structures, designed to obtain macroscopic optical property in need. Metamaterials can be designed to have optical properties which are not found in nature before, such as negative refractive index or epsilon-near-zero (ENZ) properties. Due to their exotic optical properties, the potential of metamaterials as a route to breakthrough in photonic technologies are actively being researched.

Metasurfaces refer to two-dimensional metamaterials which are capable of generating optical wavefronts in a way similar to phased antenna arrays [44, 45]. Usually, a set of nanoantennas are designed to have span an amplitude or phase range for scattered light and the designed nanoantennas are arranged to form a target amplitude or phase profile of scattered field. Focusing lenses, holograms by using metasurfaces are successful examples of wavefront synthesis. I note that polarization-converted component is considered as signal waves in most cases since dc-component that bypasses antenna array can be filtered out by using waveplates and polarizers. Hence, nanoantenna design problem can often be considered as 4-port polarization converter design problem. The polarization converting nanoantennas should be design to have certain scattering magnitude and phase in need.

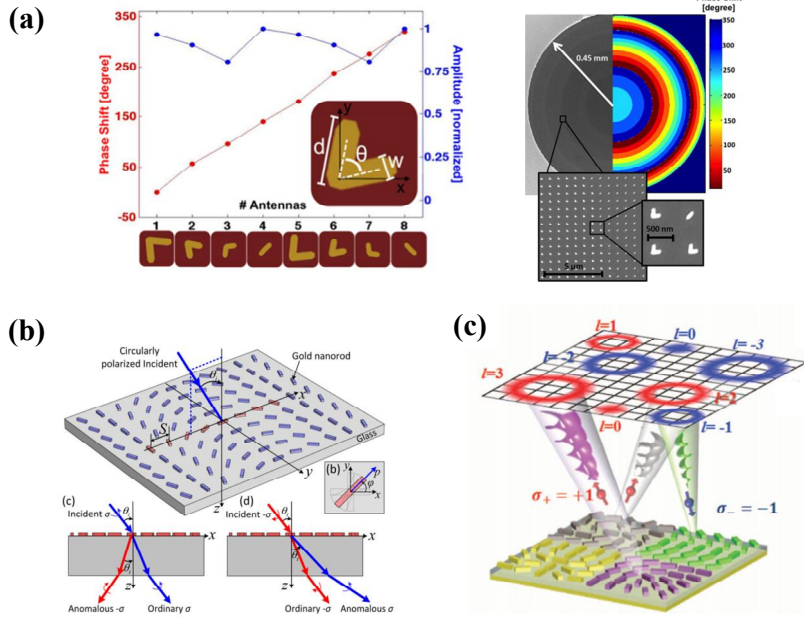


Figure 1.3 (a) Nanoantennas with designed scattering characteristics and planar lens constructed by arranging nanoantennas [45]. (b) Concept of geometric metasurface [46]. (c) Function multiplexed metasurface [48].

A simple way to control the phase of scattered light has been proposed soon after the proposal of metasurface concept [46]. When circular polarized light is incident on a metasurface with distribution of nanoantenna orientation ($\theta(x,y)$), helicity-converted scattering components acquire phase distribution that corresponds to the doubled orientation angle distribution ($\Delta\phi(x,y) = 2\theta(x,y)$). The phase that originates from antenna orientation is called the geometric phase and the metasurfaces which exploit geometric phase for phase profile synthesis are called the geometric metasurfaces. Since full phase range is covered by simply rotating nanoantennas, geometric dimensions of nanoantennas can be tuned to improve polarization conversion

efficiency or frequency response of metasurfaces [47]. By exploiting strong phase controllability of geometric metasurfaces, multi-objective designs such as polarization-multiplexing, multi-wavelength design and wide-angle design are being studied and some successful results have already been reported [48-50].

Table 1.1 Cases of Lorentz reciprocal transmission/reflection asymmetry

Mechanism	Platform	
Asymmetric configuration	Waveguide [11]	<ul style="list-style-type: none"> • Unidirectional reflection (single mode) • Asymmetrically configured stubs
	Metasurface [23-30]	<ul style="list-style-type: none"> • Unidirectional transmission • Cascade of gratings with different periods
	Metasurface [15-22]	<ul style="list-style-type: none"> • Unidirectional polarization conversion • Aligned multi-layer of metasurfaces
PT symmetry breaking	Waveguide [7,8]	<ul style="list-style-type: none"> • Unidirectional transmission/reflection • PT symmetric complex permittivity gratings
	Metasurface [41]	<ul style="list-style-type: none"> • Directional scattering in the lateral direction • PT symmetric nanoantennas

1.2 Motivation and organization of this dissertation

In the previous sections, I reviewed asymmetric mode conversion allowed by Lorentz reciprocity theorem and the metasurfaces, the design problem of which resembles the spatial mode converters in waveguides. In this dissertation, I would like to address three issues of asymmetric mode conversion: i) adjustment of asymmetry, ii) compact asymmetric mode converter and iii) Novel type of directional multiplexing by using asymmetric scattering.

Firstly, I note that design of asymmetric mode conversion property requires multi-objective design for forward and backward propagation directions. It is very simple to obtain asymmetric transmission/reflection characteristics for thick structures which can be configured in an asymmetric fashion. However, it is not easy to control transmission/reflection characteristics independently so that one can freely control asymmetry because altering characteristics in one direction affects the characteristics in the opposite direction in an unexpected fashion.

In the chapter 2 of this dissertation, I propose a design scheme of asymmetric mode conversion characteristics for waveguide system with three input ports and three output ports. Here, I note that there are two reasons why I added a pair of additional waveguide ports to conventionally studied two input/output port pairs. First, it can be easily checked that for a Lorentz reciprocal system with two input and two output ports to have asymmetric mode conversion characteristics, energy loss is necessary. Though coherent interaction cannot be identified with a placement of lossy material, additional waveguide channel can act as an energy leak channel which allows asymmetric transmission characteristics. Second, when I

consider a mode converter based on photonic interband transitions, interesting three-mode interference phenomena can be exploited. As will be explained later, a stationary supermode in permittivity grating can be exploited for simultaneous design of transmission characteristics for forward direction and backward direction.

Though permittivity grating in three mode waveguide system offers firm theoretical ground for functionality design, the footprint of the mode converter generally extends to several tens of the operational wavelengths, making the application of grating-based mode converter to nanophotonics challenging [51-56]. Simple stub structures attached to waveguides can be used for compact mode converter or mode-selective filters but their operational principle in multimode waveguides is not studied much.

In chapter 3, I propose a design strategy for photonic mode converters based on mode-selective blocking structures. After brief introduction to design strategy, I propose a compact plasmonic spatial mode converter based on a mode-selective cavity which unidirectionally transmits light. The proposed structure is designed to be compact compared to tapered converters or PIT-based converters. Moreover, I found that the redundant scattering components other than the target output can be eliminated by tuning the mode-selective cavity. The designed converter has simple geometric shape compared to topology/shape optimized converters [57-59]. Lastly, I propose an nearly perfect outcoupler for nanoslits as an example of the application of the mode conversion design strategy using the mode-selective blocking structures.

When it becomes possible to control asymmetric scattering from

nanostructures, it is possible to implement directional multiplexing schemes by combining scattering mode with different symmetric properties. Though asymmetric responses depending on light incidence direction have been extensively studied, attempts to manage asymmetry between transmission and reflection of metasurfaces under single incidence direction can be rarely found.

In chapter 4, I present a bilayer metasurface which can be used for multiplexing of transmission and reflection. Though asymmetric polarization conversion characteristics of multilayer metasurfaces have been reported in various forms, asymmetry between polarization-converted (cross-polarization) transmission and reflection has not been discussed much. Unlike thin single layer metasurfaces which emits cross-polarization waves both in forward and backward directions, bilayer metasurfaces can be designed to emit cross-polarization wave in only one direction. If one has managed to design a transmission-type and a reflection-type cell and combine them to form a supercell, it is possible to multiplex two functions, one of which for transmission side and the other one for reflection side. In this dissertation, I consider two identical layers of aperture antenna arrays in metallic films separated by a dielectric gap for the design of transmission-type cell. This is because the reflection-type cell can be immediately obtained when the transmission-type cell is designed. Converting one of two layers into reflector gives the reflection-type cell. Hence, the fabrication of the multiplexed metasurface requires only one milling process.

Lastly, I make concluding remarks on this dissertation in chapter 5. The significance of the whole dissertation is briefly explained.

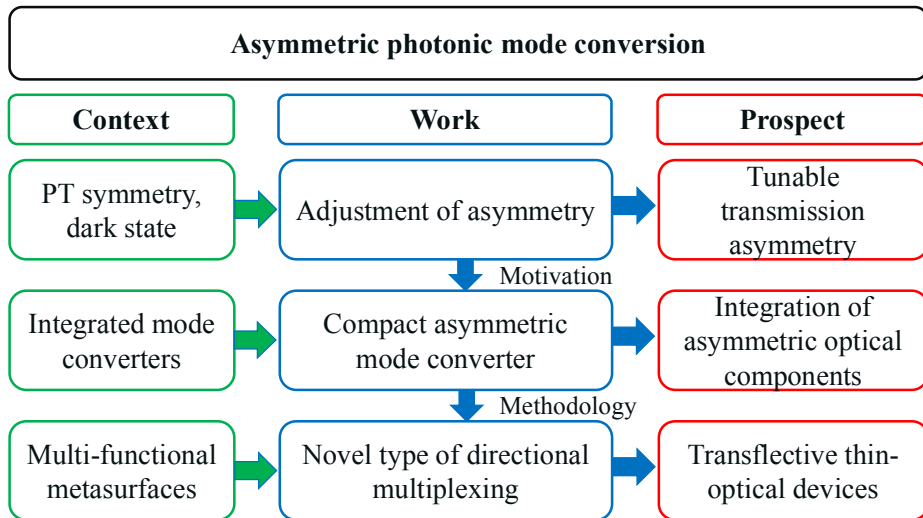


Figure1.4 Organization of this dissertation.

Chapter 2 Adjustment of waveguide mode conversion asymmetry by using photonic dark-states

2.1 Introduction

2.1.1 Asymmetric transmission in tri-mode waveguide system

allowed by Lorentz reciprocity

As referred in the previous chapter, the Lorentz reciprocity poses restriction on the realizable asymmetric scattering characteristics. Here, I illustrate the possible transmission asymmetry in the waveguide system with weak gratings. Assume the gratings couple co-propagating modes so that reflection can be neglected. Firstly, consider a lossless waveguide system with two modes expressed by the transmittance matrices:

$$T_{\text{forward}} = \begin{bmatrix} t_{11} & t_{12} \\ t_{21} & t_{22} \end{bmatrix}, \quad T_{\text{backward}} = \begin{bmatrix} t'_{11} & t'_{12} \\ t'_{21} & t'_{22} \end{bmatrix}. \quad (2.1)$$

Due to the Lorentz reciprocity, $t_{ij} = t'_{ji}$ and the energy conservation implies $|t_{11}|^2 + |t_{21}|^2 = |t'_{11}|^2 + |t'_{21}|^2$. One can easily verify that $|t'_{12}| = |t_{21}| = |t'_{21}| = |t_{12}|$ when loss and reflection are absent. Therefore, no transmission asymmetry is allowed for two-mode system without loss and reflection.

When a new waveguide mode appears in addition to the previously

considered two modes (named the mode 3), the third mode can act as an energy leakage channel to allow asymmetric transmission. When the transmittance matrix for the tri-mode waveguide system is given by the following:

$$T_{\text{forward}} = \begin{bmatrix} t_{11} & t_{12} & t_{13} \\ t_{21} & t_{22} & t_{23} \\ t_{31} & t_{32} & t_{33} \end{bmatrix}, \quad T_{\text{backward}} = \begin{bmatrix} t'_{11} & t'_{12} & t'_{13} \\ t'_{21} & t'_{22} & t'_{23} \\ t'_{31} & t'_{32} & t'_{33} \end{bmatrix}, \quad (2.2)$$

it can be found out that the Lorentz reciprocity does not pose any restriction on the ratio $|t_{21}|/|t'_{21}|$. Hence, asymmetric transmission with various asymmetric mode conversion ratios can be realized in tri-mode system without loss and reflection. The remaining question is how to adjust the asymmetric mode conversion ratio. In this chapter, I exploit the dark-mode which is a supermode defined in waveguide gratings that simultaneously couple three waveguide modes for asymmetric mode conversion characteristics design.

2.1.2 Photonic analogue of dark-state in coupled-mode theory

In this subsection, the concept of the dark-mode in coupled mode theory (CMT) is briefly reviewed. A system of waveguides with weak perturbation can be described by the CMT [60, 61]. I start from a general form of CMT for three-mode system:

$$\begin{aligned} ik_1 \frac{da_1}{dz} &= \mu_{12} a_2 e^{i\Delta_{12}z} + \mu_{13} a_3 e^{i\Delta_{13}z}, \\ ik_2 \frac{da_2}{dz} &= \mu_{12}^* a_1 e^{-i\Delta_{12}z} + \mu_{23} a_3 e^{i\Delta_{23}z}, \\ ik_3 \frac{da_3}{dz} &= \mu_{13}^* a_1 e^{-i\Delta_{13}z} + \mu_{23}^* a_2 e^{-i\Delta_{23}z}. \end{aligned} \quad (2.3)$$

where a_i , k_i are modal coefficients and propagation constants of i^{th} mode and μ_{ij} are coupling coefficients and detuning parameters between i^{th} and j^{th} modes. For simplicity, it is assumed that the permittivity perturbation has the form of a cosine function. i.e. $\Delta\epsilon(x,y,z) = \sum_{i < j=1,2,3} \delta\epsilon_{ij}(x,y)\cos(q_{ij}z)$ and $k_1 > k_2 > k_3$. Now, I consider the case when there is no coupling between mode 1 and 3 and the condition $\Delta_{12} = -\Delta_{23} = \Delta$ is satisfied. Then, Eq. (2.3) can be simplified to,

$$i \frac{d}{dz} \begin{bmatrix} a_1 \\ a_2 \\ a_3 \end{bmatrix} = \begin{bmatrix} 0 & \mu_{12} e^{i\Delta z} / k_1 & 0 \\ \mu_{12}^* e^{-i\Delta z} / k_2 & 0 & \mu_{23} e^{-i\Delta z} / k_2 \\ 0 & \mu_{23}^* e^{i\Delta z} / k_3 & 0 \end{bmatrix} \begin{bmatrix} a_1 \\ a_2 \\ a_3 \end{bmatrix}. \quad (2.4)$$

When the amplitude ratio of mode is set to $[a_1 \ a_2 \ a_3] = [-\mu_{23} \ 0 \ \mu_{12}^*]$, the right-hand side of the Eq. (2.4) vanishes. This means that the state is stationary despite there are couplings between modes. The cancellation of the right-hand side in the second line of Eq. (2.4) can be interpreted as a destructive interference between two transition amplitudes: one is a transition amplitude from the mode 1 to mode 2, and the other is one from the mode 3 to mode 2. This stationary state is known as the dark-mode in weak waveguide gratings [62]. Due to the resemblance of coupled mode equation and Schrödinger equation, direct analogy could be made in guided wave optics.

2.2 Designed asymmetry by using dark-modes

In this chapter, I propose an example of asymmetric transmission structure taking advantage of the dark-mode. Figure 2.1(a) shows the schematic of the proposed device. A silicon waveguide (waveguide I) is designed to support both of the symmetric and anti-symmetric modes whereas the SiO₂ waveguide (waveguide II) can only support a symmetric mode. Waveguides are placed close enough to each other so that the waveguide modes can be coupled via gratings in the silicon waveguide. In this paper, the mode 1, 2, and 3 refer to the symmetric mode of waveguide I, the anti-symmetric mode of waveguide I, and the symmetric mode of waveguide II, respectively. As depicted in Fig. 2.1(a), there are two cascaded waveguide gratings of different periods. The grating α is perfectly tuned for the transition from mode 1 to mode 3. The grating β , which is tuned by the condition $\Delta_{12} = -\Delta_{23} = \Delta$, couples mode 2 with modes 1 and 3 simultaneously. Between the gratings α and β , a spacing of length D is introduced for adjustment of relative phase between each mode as will be explained later. For numerical analysis, rigorous coupled wave analysis (RCWA) is used [63].

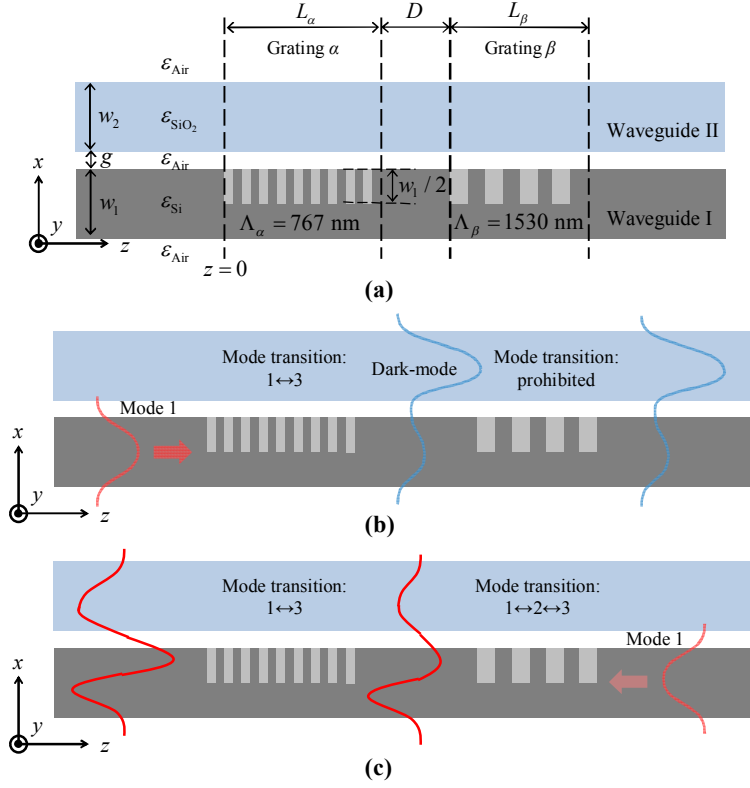


Figure 2.1 (a) A schematic of the proposed device. A silicon waveguide ($\epsilon_{\text{Si}} = 12.15$) of width $w_1 = 400$ nm and a SiO_2 waveguide ($\epsilon_{\text{SiO}_2} = 2.25$) of width $w_2 = 400$ nm are aligned in parallel with an air gap of width $g = 100$ nm. The half-infinite areas above the waveguide II and beneath the waveguide I are set to air. (b) When mode 1 is incident from the left, the grating α converts mode 1 to the dark-mode at the grating β and the dark-mode appears at the output because the dark-mode is stationary in the grating β . (c) When mode 1 is incident from the right, mode transitions in the grating β is not prohibited. As a result, various linear combinations of mode 1, 2 and 3 can appear at the output.

To observe left-to-right transmission characteristics, the mode 1 is launched from the left and enters the grating α . Since the coupled mode equation for grating α can be obtained by setting $\mu_{12} = \mu_{23} = 0$, $\mu_{13} = \mu_{13}^{(\alpha)}$ and $\Delta_{12} = 0$ in Eq. (2.3), the coupled mode equation and its general solution can be derived as follows:

$$i \frac{d}{dz} \begin{bmatrix} a_1 \\ a_2 \\ a_3 \end{bmatrix} = \begin{bmatrix} 0 & 0 & \mu_{13}^{(\alpha)} / k_1 \\ 0 & 0 & 0 \\ \mu_{13}^{(\alpha)*} / k_3 & 0 & 0 \end{bmatrix} \begin{bmatrix} a_1 \\ a_2 \\ a_3 \end{bmatrix}, \quad (2.5)$$

$$\begin{aligned} a_1(z) &= a_1(0) \cos \Omega_{13}^{(\alpha)} z - i \sqrt{\frac{k_3 \mu_{13}^{(\alpha)}}{k_1 \mu_{13}^{(\alpha)*}}} a_3(0) \sin \Omega_{13}^{(\alpha)} z, \\ a_2(z) &= a_2(0), \\ a_3(z) &= a_3(0) \cos \Omega_{13}^{(\alpha)} z - i \sqrt{\frac{k_1 \mu_{13}^{(\alpha)*}}{k_3 \mu_{13}^{(\alpha)}}} a_1(0) \sin \Omega_{13}^{(\alpha)} z, \end{aligned} \quad (2.6)$$

where I define $\Omega_{ij}^{(\zeta)2} = |\mu_{ij}^{(\zeta)}|^2 / k_i k_j$ ($i < j = 1, 2, 3$ and $\zeta = \alpha, \beta$). Here, I designed the length of grating α (L_α) and the length D such that the following condition is satisfied:

$$\begin{bmatrix} \cos \Omega_{13}^{(\alpha)} L_\alpha \\ 0 \\ -i \sqrt{\mu_{13}^{(\alpha)*} k_1 / \mu_{13}^{(\alpha)} k_3} \sin \Omega_{13}^{(\alpha)} L_\alpha \end{bmatrix} = N \begin{bmatrix} \mu_{23}^{(\beta)} e^{-i 2\pi(L_\alpha + D)/\Lambda_\beta} \\ 0 \\ -\mu_{12}^{(\beta)*} e^{i 2\pi(L_\alpha + D)/\Lambda_\beta} \end{bmatrix}, \quad (2.7)$$

where N is a normalization constant and are coupling coefficients of the grating β . Since the governing equation of the grating β is the Eq. (2.4), Eq. (2.7) implies that the dark-mode is formed at the entrance of the grating β . Note that the dark-mode expression on the right-hand side of Eq. (2.7) has an additional phase factor that represents the phase compensation due to the

shift of grating position from the origin. Due to the fact that the dark-mode is stationary in region 2, the output on the right is the same as the left-hand side of Eq. (2.7).

On the other hand, when the mode 1 is launched from the right, the sequence of interaction is reversed. Unlike in the case of left-to-right propagation, the grating in region 2 induces modal transitions because the incident mode is not the dark-mode. The general solution for Eq. (2.4) is given by the following:

$$\begin{aligned}
 \begin{bmatrix} a_1 \\ a_2 e^{i\Delta z} \\ a_3 \end{bmatrix} &= C_1 \begin{bmatrix} \mu_{23}^{(\beta)} \\ 0 \\ -\mu_{12}^{(\beta)*} \end{bmatrix} + C_2 \begin{bmatrix} \mu_{12}^{(\beta)} / k_1 \\ \Omega_- \\ \mu_{23}^{(\beta)*} / k_3 \end{bmatrix} e^{-i\Omega_- z} + C_3 \begin{bmatrix} \mu_{12}^{(\beta)} / k_1 \\ -\Omega_+ \\ \mu_{23}^{(\beta)*} / k_3 \end{bmatrix} e^{i\Omega_+ z}, \\
 C_1 &= \frac{\mu_{23}^{(\beta)*} a_1(0)}{|\mu_{23}^{(\beta)}|^2 + k_3 |\mu_{12}^{(\beta)}|^2 / k_1} - \frac{\mu_{12}^{(\beta)} a_3(0)}{|\mu_{12}^{(\beta)}|^2 + k_1 |\mu_{23}^{(\beta)}|^2 / k_3}, \\
 C_2 &= \frac{1}{2\Omega} \left(\frac{k_3 \mu_{12}^{(\beta)*} \Omega_+ a_1(0)}{|\mu_{23}^{(\beta)}|^2 + k_3 |\mu_{12}^{(\beta)}|^2 / k_1} + a_2(0) + \frac{k_1 \mu_{23}^{(\beta)} \Omega_+ a_3(0)}{|\mu_{12}^{(\beta)}|^2 + k_1 |\mu_{23}^{(\beta)}|^2 / k_3} \right), \\
 C_3 &= \frac{1}{2\Omega} \left(\frac{k_3 \mu_{12}^{(\beta)*} \Omega_- a_1(0)}{|\mu_{23}^{(\beta)}|^2 + k_3 |\mu_{12}^{(\beta)}|^2 / k_1} - a_2(0) + \frac{k_1 \mu_{23}^{(\beta)} \Omega_- a_3(0)}{|\mu_{12}^{(\beta)}|^2 + k_1 |\mu_{23}^{(\beta)}|^2 / k_3} \right),
 \end{aligned} \tag{2.8}$$

where $\Omega = \sqrt{\Omega_{12}^{(\beta)2} + \Omega_{23}^{(\beta)2} + \Delta^2 / 4}$ and $\Omega_{\pm} = \Omega \pm \Delta / 2$. Using Eq. (2.6) and Eq. (2.8), it can be proved that the output for the right-to-left transmission case is:

$$\begin{aligned}
 |a_1| &= \cos \Omega_{13}^{(\alpha)} L_{\alpha}, \\
 |a_2| &= \frac{k_3 |\mu_{12}^{(\beta)}|}{|\mu_{23}^{(\beta)}|^2 + k_3 |\mu_{12}^{(\beta)}|^2 / k_1} \left(\frac{\Omega_{12}^{(\beta)2} + \Omega_{23}^{(\beta)2}}{\Omega} \sin \Omega L_{\beta} \right).
 \end{aligned} \tag{2.9}$$

Note that $|a_1|^2$ is the same for left-to-right and right-to-left transmissions, which means consistency with Lorentz reciprocity and $|a_3|^2$ can be determined by the energy conservation condition $k_1|a_1|^2 + k_2|a_2|^2 + k_3|a_3|^2 = k_1$. The scenario of asymmetric mode conversion is summarized in the Fig. 2.1(b) and 2.1(c). As can be figured out from Eq. (2.7) and Eq. (2.9), the amplitudes of left-to-right transmission characteristic do not depend on L_β whereas those of right-to-left characteristic depend on L_β . Hence, it is possible to adjust $|a_2|/|a_3|$ for right-to-left transmission without changing left-to-right transmission characteristics.

For clear understanding, I would like to summarize the design mechanism of the proposed asymmetric transmission structure. First, the ratio between coupling coefficients $\mu_{23}^{(\beta)}$ and $\mu_{12}^{(\beta)}$ of the grating β determines the dark-mode condition. Then, the period, length of grating α and the value of D are determined to convert mode 1 to the dark-mode at the grating β . As a result, the output for the left-to-right transmission case is the dark-mode at the grating β regardless of L_β given that appropriate values for Λ_α , L_α and D are chosen. After that, right-to-left transmission characteristics can be controlled by the value of L_β . The advantage of the proposed structure is that the left-to-right transmission characteristics are not affected by the tuning of the right-to-left transmission characteristics. This observation implies that it is possible to design left-to-right and right-to-left transmission characteristics one by one. In the following sections, I demonstrate an example of asymmetric mode converter in detail.

2.3 Specification of dark-mode

In order to define a dark-mode, a grating that makes two simultaneous couplings must be designed. Figure 2.2(a) shows the dispersion relation of the modes 1, 2 and 3. Since the dark-mode can exist only when the condition $\Delta_{12} = -\Delta_{23}$ is satisfied, the period of the grating β must be tuned at $4\pi/(k_1 - k_3)$. At the same time, $|\Delta_{12}| = |\Delta_{23}| = |\Delta|$ should be small compared to $\sqrt{\Omega_{12}^{(\beta)2} + \Omega_{23}^{(\beta)2}}$ because, as can be predicted from Eq. (2.9), the accessible range of $|a_2|$ for right-to-left transmission case decreases as $|\Delta|$ increases. Hence, the widths of waveguides are adjusted so that propagation constants of three modes satisfy the condition $k_1 - k_2 \approx k_2 - k_3$. In the case of mine, I chose $w_1 = 400$ nm and $w_2 = 400$ nm. The waveguides are designed at the freespace wavelength of 1550 nm and the gap width is set to 100 nm to retain coupling with the adjacent waveguide.

In order to check whether the grating is tuned, I consider a particular solution of Eq. (2.4) when $a_2(0) = 1$ and $a_1(0) = a_3(0) = 0$;

$$\begin{bmatrix} a_1(z) \\ a_2(z) \\ a_3(z) \end{bmatrix} = \begin{bmatrix} -(i\mu_{12}^{(\beta)} / k_1 \Omega) e^{i\Delta z/2} \cos \Omega z \\ e^{-i\Delta z/2} \cos \Omega z + i(\Delta / 2\Omega) e^{-i\Delta z/2} \sin \Omega z \\ -(i\mu_{23}^{(\beta)*} / k_3 \Omega) e^{i\Delta z/2} \cos \Omega z \end{bmatrix}. \quad (2.10)$$

This particular solution implies in-phase modal coefficient oscillation of mode 1 and 3. When the grating is not tuned, one can expect the oscillation pattern would be distorted. For coupling of three modes, a binary grating inside the waveguide I is used. Though I used cosine permittivity modulation in our theoretical framework, the analysis in section 2.2 is still valid since the binary and cosine gratings of the same period are almost equivalent except

that relatively weak higher order transitions may occur for binary gratings [60]. The grating occupies the half of the waveguide I to maximize coupling coefficients which are proportional to mode overlap integral. The permittivity difference and the fill factor of the binary grating are set to -1 and 0.5, respectively, but we note that it is possible to choose other values given that the grating can be considered as a weak grating. Figure 2.2(b)-2(e) show the modal population evolution along propagation direction and E_y field distributions when we launched mode 2 from the left. When Λ_β is set at 1530 nm, the grating is tuned and in-phase oscillation of mode 1 and 3 can be clearly observed as expected in Eq. (2.10). On the other hand, when we set $\Lambda_\beta = 1550$ nm, the in-phase oscillation pattern is severely distorted.

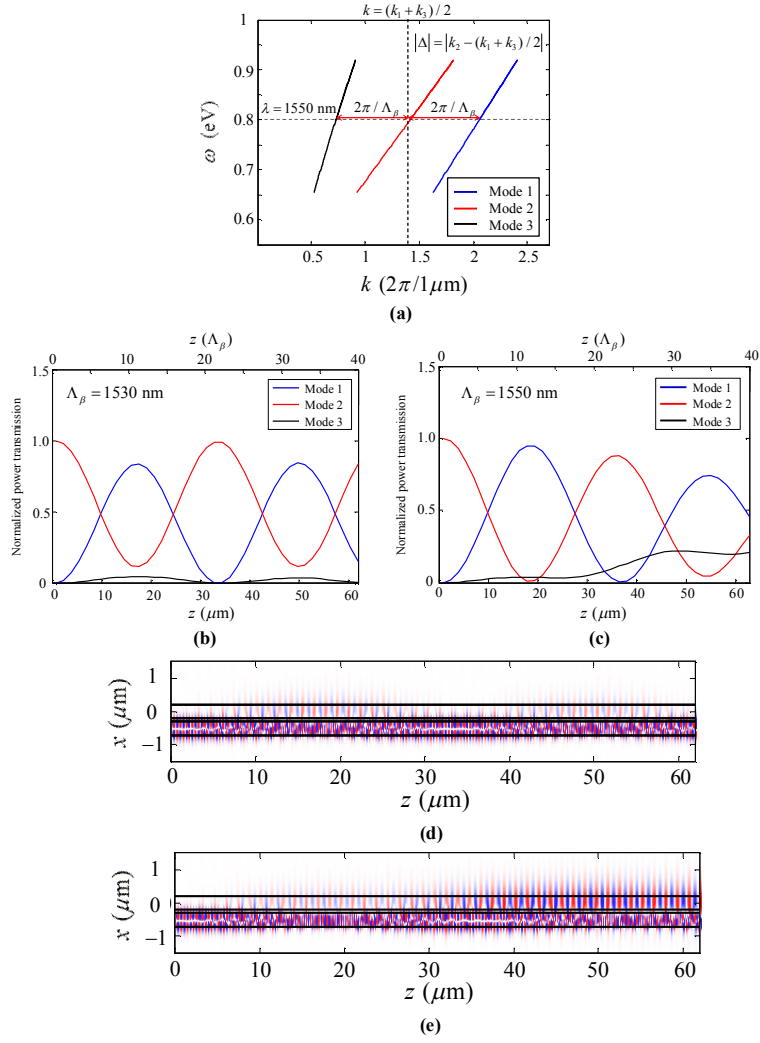


Figure 2.2 (a) The dispersion relations of three modes considered in my configuration. The widths of two waveguide are adjusted so that $\Delta k_{23} \approx \Delta k_{12}$ for simultaneous coupling of modes. Normalized power flow inside the grating β when (b) $\Lambda_\beta = 1530 \text{ nm}$ and (c) $\Lambda_\beta = 1550 \text{ nm}$. Electric field (E_y) distribution inside the grating β when (d) $\Lambda_\beta = 1530 \text{ nm}$ and (e) $\Lambda_\beta = 1550 \text{ nm}$.

After tuning of the grating, the dark-mode condition should be specified. A parametric study has been done to find out that the power flow ratio for mode 1 and 3 should be 5:95 to form a dark-mode in the previously designed grating β . Figure 2.3(a) shows that the power flow of mode 1 and 3 is almost constant within the grating β when the dark-mode condition is well-satisfied. Electric field distribution (E_y) of the dark-mode shown in Fig 2.3(b) indicates that the dark-mode is not affected by the grating β . The dependence on the variation of incident power flow ratio and relative phase is investigated in Figs. 2.3(c) and 2.3(d), respectively. Unlike the case of exact dark-mode incidence, the normalized power flow of mode 3 changes along the propagation within the grating β when the input amplitude ratio and relative phase between the mode 1 and 3 is changed from the dark-mode condition. These results show that the stationary state shown in Fig. 2.3(b) is only achievable under the exact dark-mode condition which implies the destructive interference of modal transition amplitudes from mode 1 to mode 2 and that from mode 3 to mode 2.

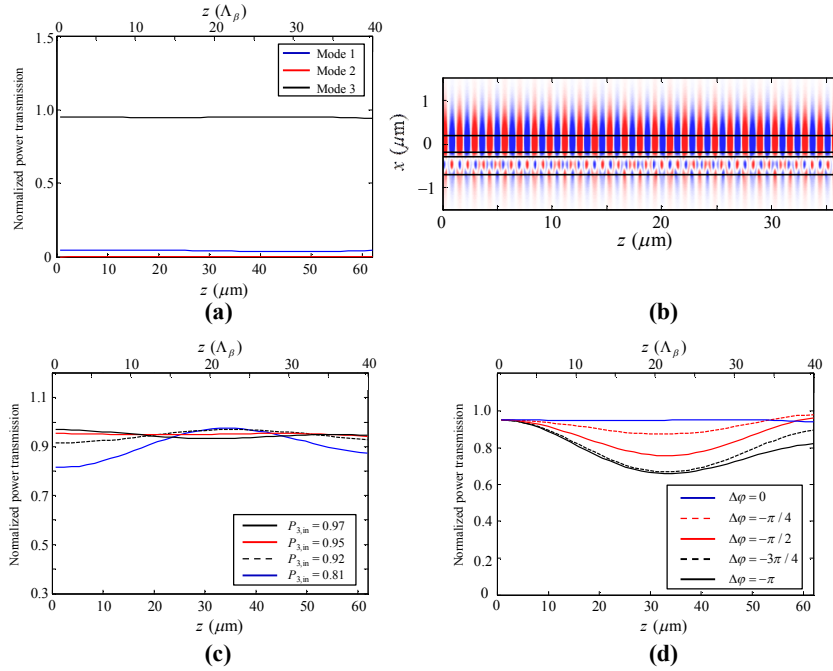


Figure 2.3 (a) Normalized power flow in the grating β when the dark-mode is launched. (b) E_y field distribution of the dark-mode in the grating β . Normalized power flow of mode 3 in grating β when there is (c) a variation of normalized input power flow of mode 3 ($P_{3,\text{in}}$) and (d) a variation of relative phase of mode 3 ($\Delta\phi$) with respect to the exact dark-mode condition at the entrance of grating β .

2.4 Asymmetric mode conversion by cascaded gratings

Now, I focus on the design of grating α of Fig. 2.1(a) which converts mode 1 to the dark-mode at the grating β . As we mentioned in section 3.2, the length of grating α should be designed to match the modal population ratio of the dark-mode condition at the end of the grating. The transverse profile of the permittivity perturbation is the same as the grating β , but the

grating period is set to 767 nm to couple mode 1 and 3. Figure 2.4(a) shows the normalized power flows inside the grating α when the grating is exactly tuned for the transition from the mode 1 to mode 3. It was found that 67 periods are required for power flow ratio of 5:95 that we specified as the dark-mode condition. Next, the length D for relative phase adjustment should be determined, otherwise modal transitions occur in the grating β since the relative phase between the modes 1 and 3 at the entrance of grating β is also important for dark-mode condition. Figure 2.4(b) shows left-to-right transmission characteristics when only the amplitude condition of the dark-mode in the grating β is satisfied, but a wrong value of D is chosen. Oscillation of power flows inside the grating β clearly shows that correct choice of D is critical for our design of asymmetric mode converter. To find the correct value of D , transmitted power flow at the end of the grating β is calculated for different values of D as shown in Fig. 2.4(c). Since L_β does not affect left-to-right transmission characteristic when the dark-mode condition is satisfied, the length of the grating β is temporarily set to 40 periods, which is long enough to clearly observe the stationary nature of the dark-mode. The value of D is changed from 5 μm to 5.75 μm since the period of beating for mode 1 and 3 is roughly 750 nm. As marked in Fig. 2.4(c), the transmitted power for mode 2 vanishes when $D = 5.25 \mu\text{m}$ and the power flow ratio of mode 1 and 3 was found to be the same as the dark-mode. Figure 2.4(d) shows the modal power flows through two cascaded gratings for well-designed values of Λ_α , L_α , and D ; it is clearly shown that modal power flows do not fluctuate in the grating β , which means that the dark-mode is incident on the grating β as I intended.

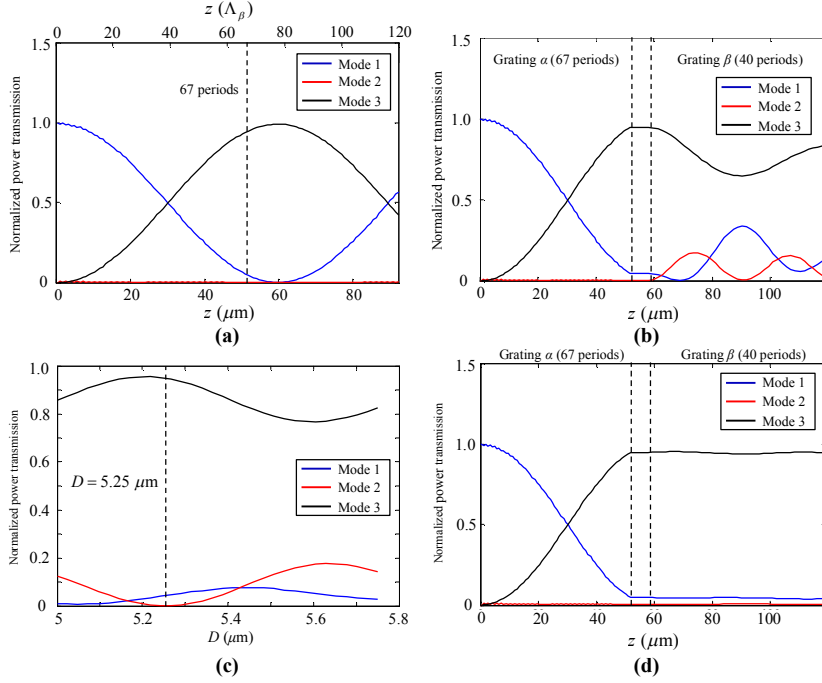


Figure 2.4 (a) Normalized power flow inside the grating α tuned for the transition from mode 1 to 3. (b) Normalized power flow through two cascaded gratings when a wrong value of D is chosen ($D = 5.6 \mu\text{m}$). (c) Normalized power transmission after the two cascaded gratings depending on D . The length of the grating β is 40 periods. (d) Normalized power flow inside two cascaded gratings when $D = 5.25 \mu\text{m}$.

Now, let me consider the case of right-to-left transmission. As the length of the grating β does not affect left-to-right transmission characteristic for dark-mode incidence, it is possible to change right-to-left characteristics without changing left-to-right characteristics by adjusting L_β . Here, recall that the grating α is not tuned neither for the transition from mode 2 to mode 1 nor one from mode 2 to mode 3. Hence, when these transitions are

neglected, the output power flow of the mode 2 for the right-to-left transmission case is not changed from the power flow of the mode 2 at the exit of the grating β . The power flow inside the two cascaded gratings that I designed to obtain (Fig. 2.4(d)) is shown in Fig. 2.5(a) for right-to-left propagation case. It can be observed that the power flow of the mode 2 does not change significantly in the grating α as I predicted. To determine the output power for the mode 2, modal energy transfer inside the grating β is investigated for mode 1 incidence as shown in Fig. 2.5(b). Depending on the value of L_β , the normalized power flow of the mode 2 can be tuned from 0 to 0.84. Therefore, it is possible to access wide range of right-to-left transmission characteristics. For clear demonstration of adjustable asymmetric transmission characteristics, we compared two cases in which the length of the grating β are set to 11 and 16 periods in Figs. 2.5(c)-5(f).

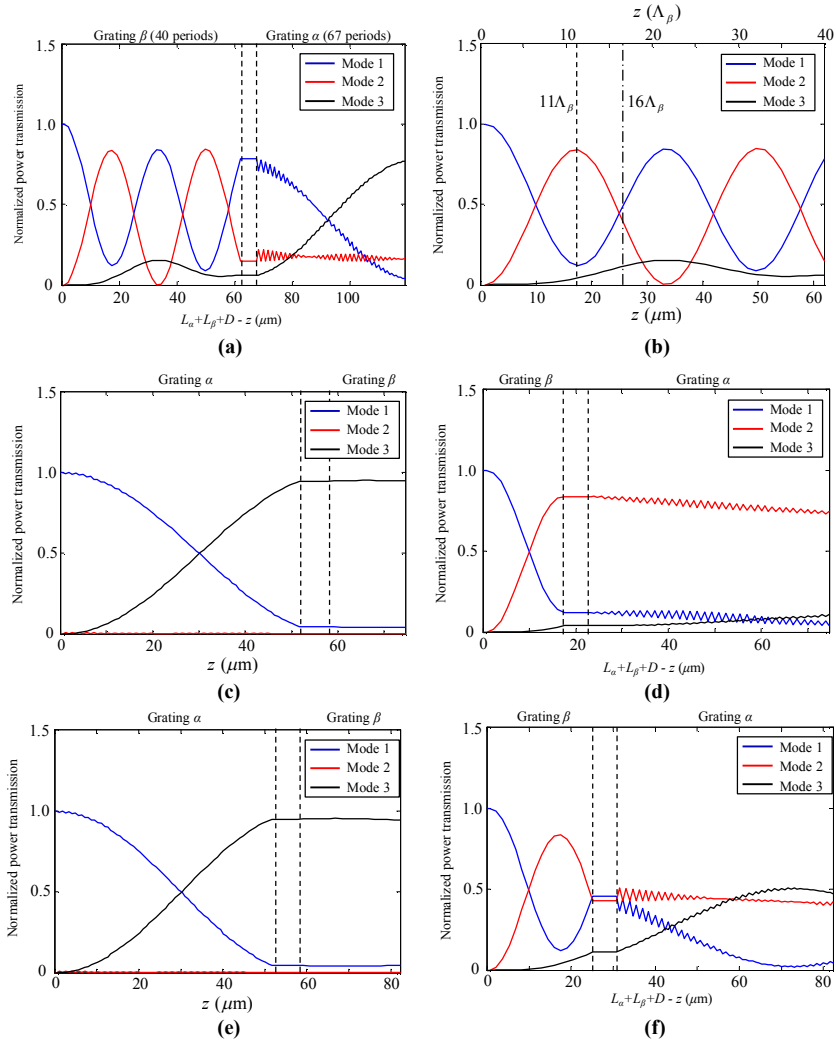


Figure 2.5 (a) Normalized power flows for the right-to-left propagation case. (b) Normalized power flows inside the grating β for the case of mode 1 incidence. Normalized power flows when the length of the grating β is set to 11 periods (c) for the left-to-right and (d) right-to-left propagation cases. (e) and (f) are those for the 16 periods long grating β .

Figure 2.5(c)-(d) and Fig. 2.6(a)-(b) show the power flow dynamics and E_y field distributions for left-to-right and right-to-left propagation when the length of grating β is set to 11 periods whereas Fig. 2.5(e)-(f) and Fig. 2.6(c)-(d) show those when the length of grating β is set to 16 periods. When L_β is altered, the left-to-right transmission does not change as shown in Fig. 2.5(c) and 2.5(e) and the transmitted field distribution for left-to-right propagation depicted in Fig. 2.6(a) and 2.6(c) is that of the dark-mode. On the other hand, for right-to-left transmission as shown in Fig. 2.5(d) and 2.5(f), the output power flow ratio of mode 2 and 3 is changed as L_β increases. Hence, the asymmetric transmission characteristics in both directions are successfully designed. Note that the slight energy loss (< 1.2 dB) is due to the leakage.

Before I conclude this section, some remarks must be made regarding small power flow oscillation of the mode 1 and 2 in the grating α . This oscillation is due to the coupling of mode 1 and 2 which cannot be completely neglected, though the grating α is severely detuned with respect to the transition between the mode 1 and 2. The reason why the amplitude of small oscillation varies by cases in Fig. 2.5 is because the oscillation amplitude depends on the ratio of modal coefficients which is a_2/a_1 in our case. For simple illustration of this effect, we consider a two level system which is described by the following coupled equations:

$$\begin{aligned}\frac{da_1}{dz} &= i\frac{\Omega}{2}a_2e^{i\Delta z}, \\ \frac{da_2}{dz} &= i\frac{\Omega}{2}a_1e^{-i\Delta z},\end{aligned}\tag{2.11}$$

where Ω and Δ represent coupling strength and detuning, respectively. When I set $a_2(0) = \kappa a_1(0)$, the Eq. (2.11) can be solved to obtain the following:

$$|a_1(z)|^2 = \left(\frac{1 + (\kappa\Omega - \Delta)^2}{2} - \frac{(\kappa^2 - 1)\Omega^2 - 2\Delta\kappa\Omega}{2(\Omega^2 + \Delta^2)} \cos(\sqrt{\Omega^2 + \Delta^2} z) \right) |a_1(0)|^2. \quad (2.12)$$

Hence, if $\Omega \neq 0$, oscillation amplitude depends on κ . More intuitive graphical explanation is possible using the Bloch's formulation of two level atoms which can be found in [64].

Now, I would like to conclude the section by briefly commenting on the limitations of proposed design scheme. In principle, if the dispersion relation of three modes are carefully tuned so that $\Delta = 0$ for the grating β , my design scheme enables design of arbitrary transmission characteristics in one direction, which was the right-to-left propagation case in my example. However, transmitted wave for the other propagation direction must be a dark-mode which is a linear combination of only two modes. Therefore, output power of one of three modes must be zero for one propagation direction. Moreover, my scheme itself does not provide a way to design transmission characteristics for every input mode or design of both transmission and reflection characteristics, which is much more challenging. Another shortcoming of the proposed scheme is the long length of the device extending over several tens of μm due to the use of weak gratings. Therefore, development of compact mode converters is necessary for further improvements.

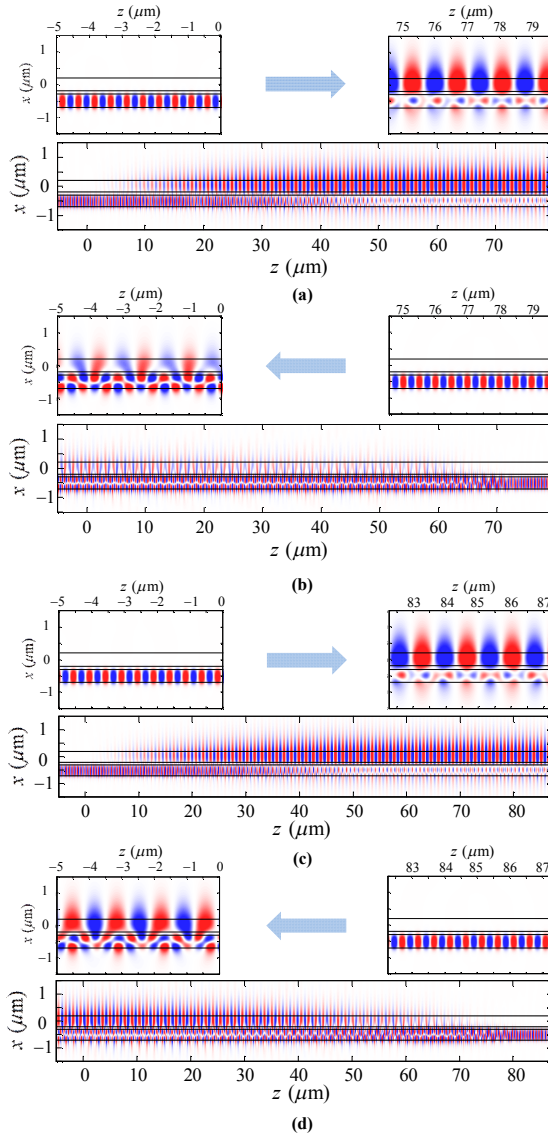


Figure 2.6 E_y field distributions when the length of the grating β is set to 11 periods (a) for left-to-right and (b) right-to-left propagation cases. (c) and (d) are those when the length of the grating is set to 16 periods.

2.5 Conclusion

In this chapter, a scheme for designing asymmetric transmission devices in waveguide systems that support three modes is proposed. The proposed scheme exploits dark-mode which can be defined by a grating that couples one mode to two other modes simultaneously. Stationary property of the dark-mode fixes transmission characteristic in one direction, and it enables the independent design of transmission characteristics for left-to-right and right-to-left directions. Therefore, the scheme enables access to wide range of asymmetric transmission characteristics and the design process is purely sequential. Since the proposed scheme is applicable for various three-mode waveguide systems, asymmetric mode converters can be designed in different platforms following identical design process. Moreover, the design of active asymmetric transmission devices can be easier especially when it is required to tune the transmission characteristics in one direction and fix the transmission characteristics in the opposite direction. Therefore, the proposed scheme may find its applications in tunable, active asymmetric transmission devices.

Chapter 3 Compact plasmonic spatial mode converter with mode conversion asymmetry

3.1 Introduction

3.1.1 Asymmetric spatial mode converters in waveguides

In the previous chapter, I proposed an adjustable asymmetric waveguide mode converter based on the Bragg grating structures which induce photonic interband transitions. Though exploitation of photonic interband transition offers interesting functionality design capability on the firm ground of coupled mode theory, the length needed for efficient mode conversion generally extends to several tens of operation wavelength. Since asymmetric configuration can result in asymmetric mode conversion characteristics, various mode conversion mechanisms other than photonic interband transition can be used to design asymmetric mode converters. Huang et al. has proposed a plasmonic waveguide with series stub structures with unidirectional reflection characteristics and analyzed unidirectional reflection characteristics in terms of exceptional points related to PT symmetry breaking [11]. As shown in Fig. 3.1, unidirectional reflection has been successfully achieved by employing two stub structures configured in

asymmetric fashion. Since stub structures only require few effective wavelengths of the waveguide modes in terms of footprint, structures with asymmetric transmission and reflection characteristics can be constructed in a compact space. In multi-mode waveguides, asymmetric mode conversion in transmission can be realized by using stub-based mode conversion structures. In this chapter, I propose a compact spatial mode converter in a plasmonic waveguide with asymmetric mode conversion characteristics.

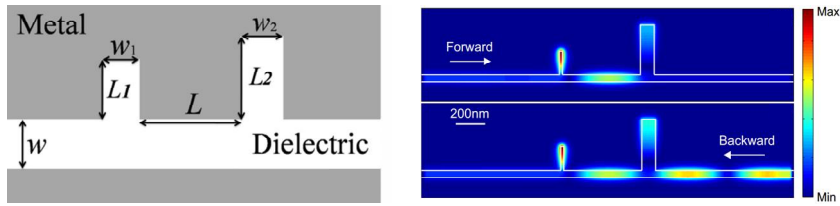


Figure 3.1 Unidirectional reflection of plasmonic waveguide mode by asymmetrically configured stub structures [11].

3.1.2 Mode conversion by using mode-selective blocking filters

In this subsection, I briefly explain design strategy for the asymmetric mode converter which I propose in this chapter. Figure 3.2 shows conceptual diagram of mode converter with 4 ports. The ports 1 (or 2) and 1' (or 2') represent identical waveguide mode ports placed on the left and right side of the mode converter, respectively. When a reflective blocker is placed at the port 1' while leaving the port 1 opened, the total structure exhibits asymmetric mode conversion characteristics. When light is incident from the port 1, the incident light can enter into the mode conversion structure making converted output at the port 2' as shown in Fig. 2.3(a). On the other hand, when the light is incident from the port 1', the incident light is simply blocked at the entrance of the mode conversion structure as depicted in Fig.

2.3(b). Therefore, one can conclude that combination of mode conversion structure and a mode selective blocking structure simply gives unidirectional mode conversion characteristics.

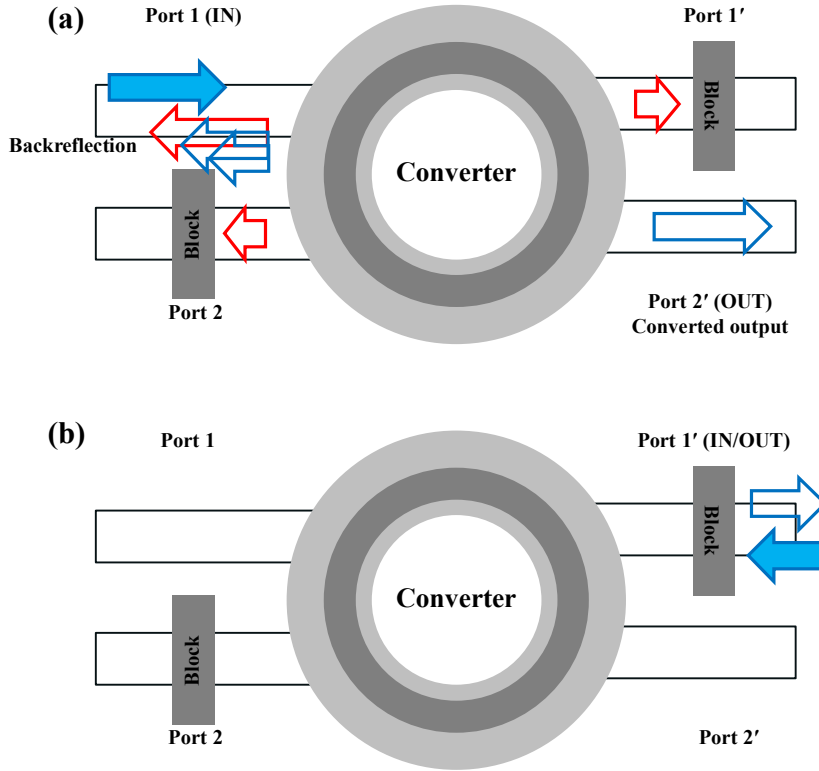


Figure 3.2 Abstract illustration of 4-port mode converter when the input mode is incident from (a) port 1 (left) and (b) port 1' (right).

Interestingly, mode selective blockers can be used to eliminate the redundant scattering components other than the target output mode. For instance, the blocking structure at port 1' not only blocks light incident from port 1', but also blocks transmission through port 1' when the light is incident from the port 1. Similarly, when another blocker is placed at port 2 as depicted in Fig. 3.2, the reflection to the port 2 can be suppressed. The

reflected waves from the blockers can affect backreflection to the input port and it is even possible to cancel out the backreflection by tuning of mode-selective cavity formed by the mode-selective blockers. The elimination of idle scattering components enables easier integration of the mode converter in complex photonic networks and the conversion efficiency can be enhanced by energy recycling process.

In the following section, I firstly propose a simple stub plasmonic spatial mode converter combined with mode-selective filters and show their asymmetric mode conversion characteristics. Then, I tune the cavity formed by the mode-selective filters to eliminate all the idle scattering components.

3.2 Plasmonic spatial mode conversion by using a stub mode converter

3.2.1 Dispersion relation of the plasmonic waveguide

In this subsection, I analyze dispersion characteristics of the metal-insulator-metal (MIM) plasmonic waveguide modes. The waveguide under consideration is composed of a silicon core ($\epsilon_{\text{Si}} = 12.15$) and surrounding half-infinite silver layers as shown in Fig 3.3(a). For modeling electromagnetic response of the metal, I used the Drude model: $\epsilon(\omega) = \epsilon_{\infty} - \omega_p^2/(\omega^2 + i\Gamma\omega)$ where ϵ_{∞} , ω_p and Γ are the relative permittivity at high frequency limit, the plasma frequency and the damping constant, respectively. I used the parameters for the silver ($\epsilon_{\infty} = 3.7$, $\omega_p = 9$ eV and $\Gamma = 0.018$ eV) [65]. The operating wavelength is fixed to $\lambda = 1550$ nm. For numerical simulation, rigorous coupled wave analysis (RCWA) is used [63].

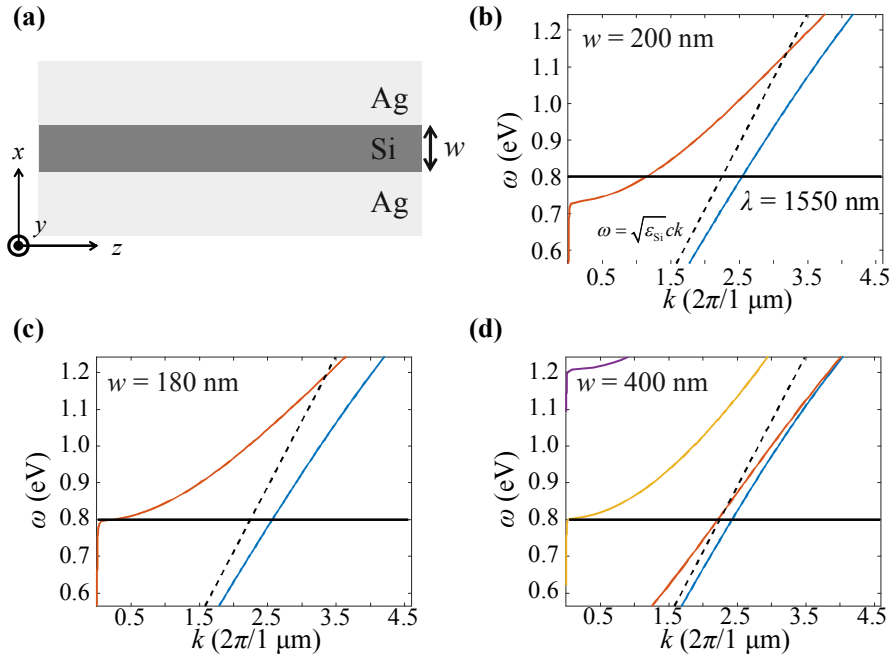


Figure 3.3 (a) Schematic of the silver-silicon-silver plasmonic waveguide.

Dispersion relations for the plasmonic waveguide when the width of the waveguide (w) is (a) 200 nm, (b) 180 nm and (c) 400 nm. The solid blue and red lines represent the symmetric and the anti-symmetric modes. The black dashed line represents the light line of the silicon and the yellow, purple lines represent the photonic modes.

Figures 3.3(b)-(d) show the dispersion relations of the plasmonic waveguide for three different core widths. When w is set at 200 nm, the plasmonic waveguide supports two plasmonic modes, one of which has symmetric magnetic field profile (symmetric mode) and the other one has anti-symmetric magnetic field profile (anti-symmetric mode). At the operating wavelength 1550 nm, two plasmonic modes are both supported.

When the width of the core is decreased, the cut-off frequency of the anti-symmetric mode is lowered. As shown in Fig. 3.3(c), the anti-symmetric mode becomes cut-off at $\lambda = 1550$ nm, when $w = 180$ nm. When the width of the core is increased, photonic modes can be supported inside the waveguide. As shown in Fig. 3.3(d), lowest order photonic TM mode's cut-off wavelength reaches the operating wavelength. In the following parts of this chapter, the width of the main waveguide is fixed to 200 nm.

3.2.2 Stub mode converter

Now I analyze the mechanism of the mode converter using a simple stub structure. Figure 3.4(a) shows the schematic of the stub mode converter of width w_{stub} and depth L_{stub} . Since the stub converter has spatial inversion symmetry with respect to a line parallel to the x -axis, the stub mode converter does not exhibit asymmetric mode conversion characteristics.

In order to analyze the stub structure, I assume that the stub is shallow in the sense only the symmetric and the anti-symmetric plasmonic modes can propagate in the z -direction inside the stub structure. Since photonic modes start to appear inside the stub when $w + L_{\text{stub}}$ exceeds 400 nm (refer to Fig. 3.3), I mainly focused on the cases where $L_{\text{stub}} < 200$ nm. Assuming shallow stub, the mode conversion characteristics of the stub converter can be understood by investigating mode conversion at the boundary of the stub mode converter. I define the transmittance and reflectance matrices for the forward and backward cases as (t_{ij}, r_{ij}) and (t'_{ij}, r'_{ij}) , respectively, where the indices s, a represent the symmetric and the anti-symmetric plasmonic modes. Here, the forward direction refers to the case when the light is incident from the left in Fig. 3.4(b). As can be found in Fig. 3.4(c) and 3.4(d),

abrupt change of tendency is found near $L_{\text{stub}} = 200$ nm where a photonic mode comes into play. The transmittance data can be understood in terms of modal overlap. When the symmetric mode is incident in the forward direction, the ratio of the symmetric mode and the anti-symmetric mode approaches to 1:1 as the depth of the stub increases. For the anti-symmetric mode incidence, overall transmission decreases when the depth of the stub increases because the mode profile in the stub becomes flattened resulting in small modal overlap integral.

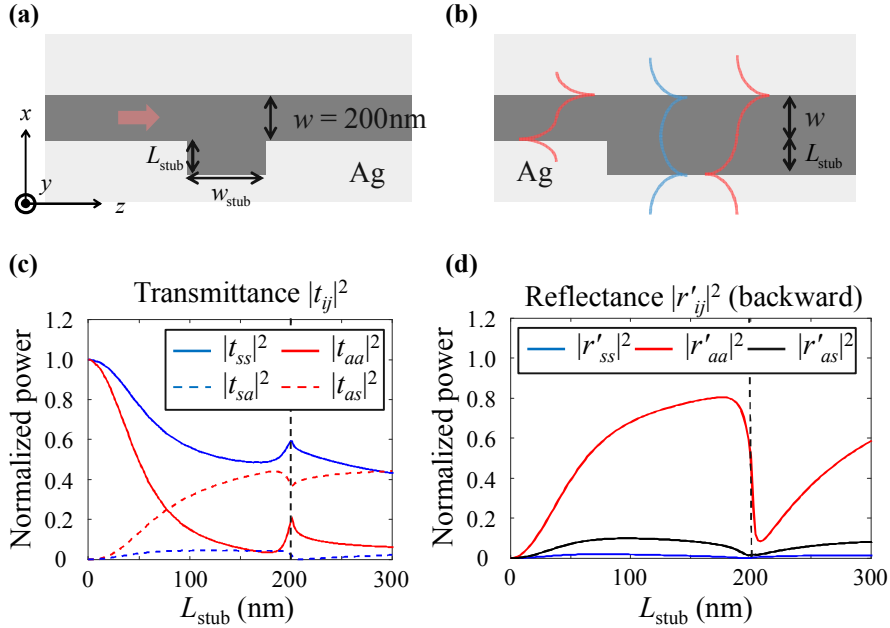


Figure 3.4 (a) Schematic of the stub mode converter. (b) Mode conversion at the boundary of the stub structure. Transmittance in the forward direction (t_{ij}) and reflectance in the backward direction (r'_{ij}) for the stub boundary.

Now, based on the transmittance and the reflectance matrices for the stub boundaries, I investigate the mechanism of the mode conversion from

the anti-symmetric plasmonic mode to symmetric plasmonic mode. Note that every transmissive mode conversion coefficient of the stub structure is the same due to Lorentz reciprocity and spatial inversion symmetry. There are two major pathways of mode conversion from the anti-symmetric mode to the symmetric mode, which are expressed in Fig. 3.5(a) and 3.5(b). The first path corresponds to the case in which the anti-symmetric plasmonic mode incident from the left is converted to the symmetric plasmonic mode inside the stub at the entrance of the stub. Because the symmetric plasmonic mode inside the stub can be coupled out with negligible reflection as shown in Fig. 3.4(d), Fabry-Pérot resonance would be weak. The second path corresponds to the case in which the anti-symmetric mode incident from the left enters in to the stub structure through the anti-symmetric mode inside the stub and then couples out to the symmetric mode on the right side. Since anti-symmetric plasmonic mode inside the stub experiences strong reflection inside the stub, the stub structure acts as a cavity resulting in Fabry-Pérot resonances. Comparing the absolute value of transmittance products $|t_{as}t_{ss}|$ and $|t_{aa}t_{as}|$ as shown in Fig. 3.5(c), the terms which correspond to the two paths have the same order of magnitude, meaning that both terms should be taken into account to understand the mode conversion by stub structure. Figure 3.5(d) shows the mode conversion efficiency ($|t_{sa,stub}|^2$) depending on the stub width (w_{stub}) when the depth of the stub is fixed to 70 nm. As can be expected, Fabry-Pérot resonance peaks appearing with the interval of half the effective wavelength of the anti-symmetric mode inside the stub ($\lambda/2n_{a,stub}$). Also, oscillation of peak intensity appear with the period corresponds to the beating length inside the stub ($\lambda/(n_{s,stub} - n_{a,stub})$). Hence, the mode conversion

mechanism of the stub structure has been revealed: interference of a non-resonant pathway which leads to long term beating and a cavity-resonant pathway which results in short term peaks.

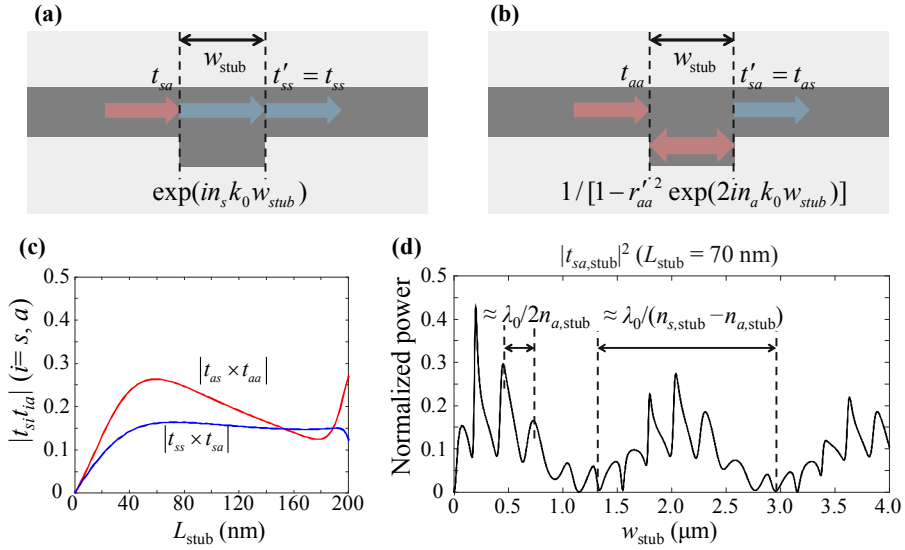


Figure 3.5 Illustration of mode conversion pathways, one of which is (a) non-resonant and the other one is (b) resonant. (c) Transmittance products which show relative contribution of two pathways to mode conversion. (d) Mode conversion efficiency depending on the width of the stub where the depth of the stub is fixed to 70 nm.

Though the above analysis reveals the mechanism inside the cavity, the explicit condition for optimal mode conversion could not be derived. One can simply guess from the Fig. 3.5(c) that the depth of the stub should in the range of 40~150 nm to ensure enough mode-mixing by the stub and the width of the stub should meet the Fabry-Pérot resonance condition for the anti-symmetric mode inside the stub. Hence, I implement a parametric study in the vicinity of the expected optimal condition and determine the mode

conversion stub parameters: w_{stub} and L_{stub} . From the mode conversion efficiency map shown in Fig. 3.6(a), I chose $w_{\text{stub}} = 200$ nm and $L_{\text{stub}} = 70$ nm (marked by the black circle in Fig. 3.6(a)) so that the normalized power transmission of the symmetric mode is around 43% when the anti-symmetric mode is incident. At this condition, the transmission of the anti-symmetric mode is 24%, and the reflections of the symmetric and the anti-symmetric mode are 5% and 15%, respectively. The $|H_y|$ field distribution in Fig. 3.6(b) shows the partial mode conversion of the optimized stub structure. In the next section, I will transform this stub mode converter to asymmetric mode converter by using mode-selective filters.

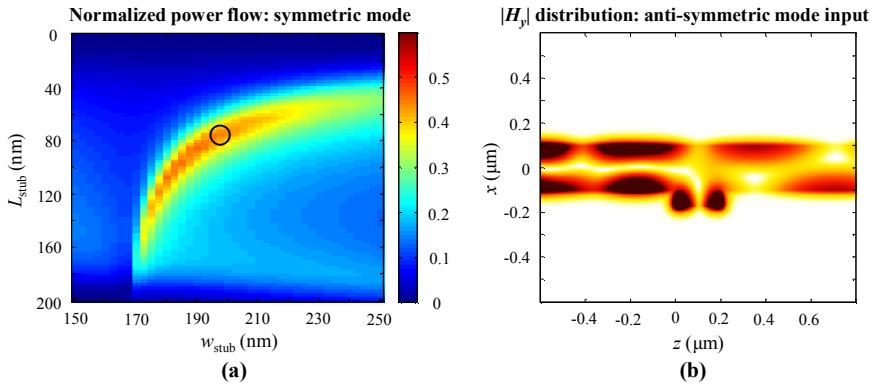


Figure 3.6 Transmission of the symmetric mode when the anti-symmetric mode is launched to the stub converter. (b) $|H_y|$ distribution for the mode conversion stub when the anti-symmetric mode is incident from the left.

3.3 Asymmetric mode conversion by using spatial mode filters

3.3.1 Configuration of the proposed structure

In this subsection, I outline the plasmonic mode converter with asymmetric mode conversion characteristics. As the schematic in Fig. 3.7 shows, the proposed structure is composed of three functional components. The first one at the left end is a notch filter (F1) which completely blocks the symmetric mode. The filter is symmetric with respect to the central line of MIM waveguide to ensure no coupling between the MIM symmetric and anti-symmetric modes. At the right end, a barrier (F2) using low permittivity core is placed [65]. Due to the low permittivity of the core, the MIM anti-symmetric mode becomes cut-off inside the barrier. When the thickness of the barrier becomes thick enough, the MIM anti-symmetric mode can be completely blocked and reflected. Note that the barrier has symmetric configuration just as the notch filter. Between the two filters F1 and F2, the stub mode converter which is designed in the previous section is placed. The two waveguide regions between the filters and the stub mode converter are named region α and β . The filters F1 and F2 correspond to mode-selective blockers described in the subsection 3.1.2 and one can expect asymmetric mode conversion characteristics of the overall structure.

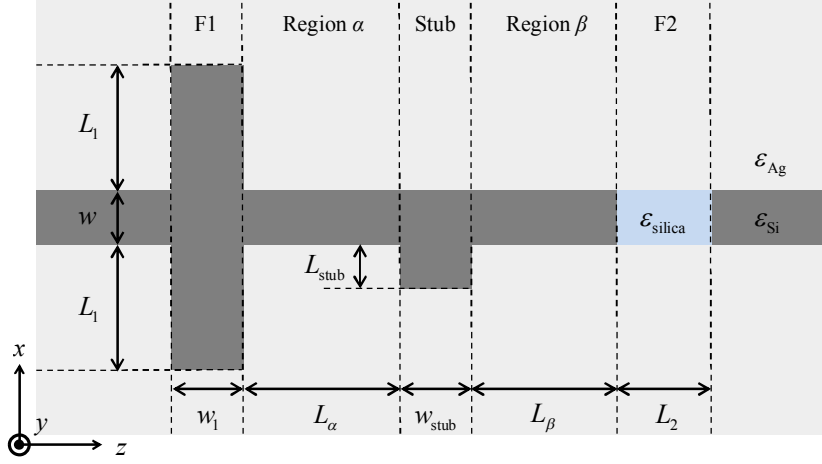


Figure 3.7 The schematic of the proposed mode converter. The MIM anti-symmetric mode is incident from the left. For material parameters, we used $\epsilon_{\text{Ag}} = -122 + 2.83i$ [65] (at $\lambda = 1550$ nm), $\epsilon_{\text{Si}} = 12.15$ and $\epsilon_{\text{silica}} = 2.25$.

3.3.2 Design of the anti-symmetric mode barrier (F2)

In order to design the anti-symmetric mode barrier, the dispersion relation of the MIM waveguide must be investigated first. In Fig. 3.8(a), the dispersion relations of the MIM waveguides with different core permittivity are shown. Due to the cut-off condition for the anti-symmetric mode, the anti-symmetric mode is not supported for low permittivity core. The transmission through the low core permittivity barrier is investigated for varying barrier length L_2 as shown in Figs. 3.8(b) and 3.8(c) and the behaviors are consistent with the previous research [65]. To completely block the anti-symmetric mode, L_2 must be at least 150 nm. For efficient transmission of the symmetric mode, L_2 should be set at integer multiple of 470 nm. To minimize footprint and energy loss, I set L_2 at 470 nm.

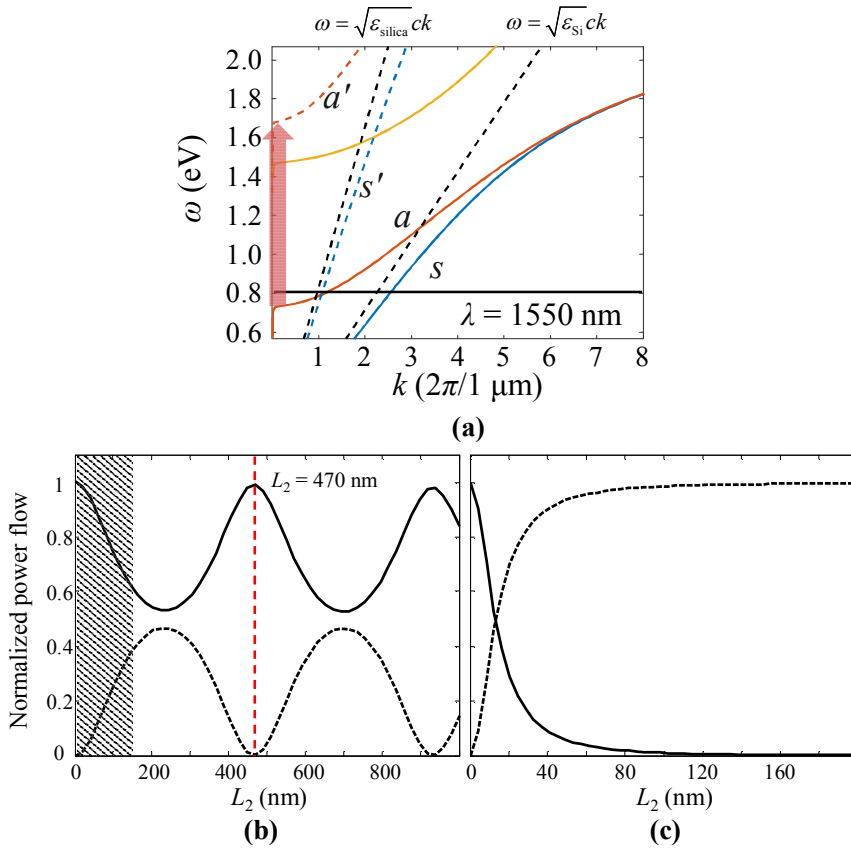


Figure 3.8 Dispersion relations of plasmonic waveguides with silicon and silica core. Solid blue and red lines represent the symmetric and the anti-symmetric modes for silicon core and the dashed blue and red lines represent ones for the silica core (cut-off frequency of the anti-symmetric mode for the silica core waveguide is shifted to 1.68 eV). The dashed black lines are the light lines for the silica and the silicon. The solid yellow line represents the photonic TM mode for the silicon core. Transmission (solid line) and reflection (dashed line) of the F2 for (b) the symmetric and (c) the anti-symmetric mode incidence.

3.3.3 Design of the notch filter (F1)

Now, I optimize the notch filter (F1). The design parameters are w_n and L_n as expressed in Fig. 3.9(a). Due to the mirror symmetry of the notch filter with respect to the central line of the main waveguide, cavity modes with symmetric (or anti-symmetric) magnetic field profile can be excited when symmetric (or anti-symmetric) plasmonic mode is incident on the notch filter as shown in Fig. 3.9(b) and 3.9(c). As a result, mode conversion does not occur in the notch filter. The responses of the notch filter differ by the number of modes supported by the side waveguides. Here, I compare two cases: 1) only the symmetric mode is supported in the side waveguides ($w_n < 200$ nm) and 2) the symmetric and the anti-symmetric mode is supported in the side waveguides ($w_n > 200$ nm).

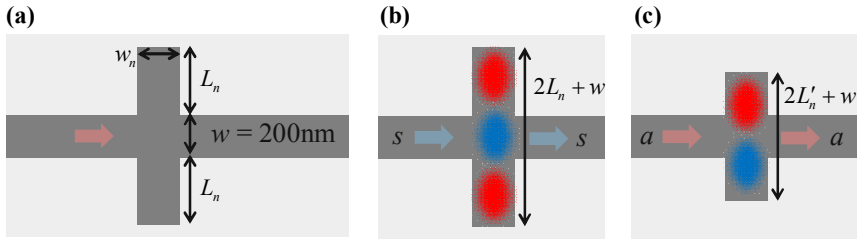


Figure 3.9 Power transmission map of the notch filter for (a) the symmetric mode and (b) the anti-symmetric mode incidence. $|H_y|$ distributions for the optimized notch filter when (c) the symmetric or (d) the anti-symmetric mode is incident from the left.

Figure 3.10(a) and 3.10(b) show the power transmission and absorption of the notch filter depending on the length of the side waveguide L_n when w_n is set at 150 nm. The alternating absorption peaks signify the cavity mode

resonances and corresponding transmission dips appear for symmetric mode incidence and transmission peaks for anti-symmetric mode incidence. The interval of the resonances corresponds to the half of the effective wavelength for the side waveguides as expected.

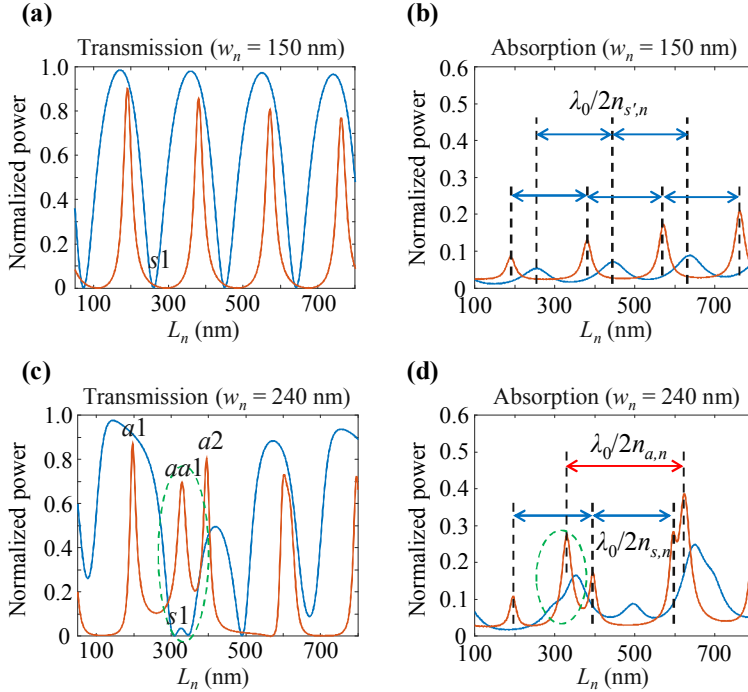


Figure 3.10 (a) Power transmission and (b) absorption of the notch filter when $w_n = 150$ nm. (c) Power transmission and (d) absorption of the notch filter when $w_n = 240$ nm. Solid blue and red lines represent the cases for the symmetric mode and the anti-symmetric mode incidence, respectively.

Condition for near zero symmetric mode transmission can be easily found but the anti-symmetric mode transmission is too low at the symmetric mode blocking condition since the transmission dips for the symmetric mode incidence are positioned between the transmission peaks for anti-symmetric

mode incidence. Similar tendency observed for the case $w_n < 200$ nm; hence, the desired condition for notch filter is not found. When w_n is set at 240 nm, additional resonances which originated from the anti-symmetric mode in the side waveguide appear in the Fig. 3.10(c) and 3.10(d). Since the difference of effective indices of the symmetric and the anti-symmetric mode depends on w_n , the relative position of the transmission dip for the symmetric mode incidence (named as $s1$) and the transmission peak for the anti-symmetric mode incidence (named as $aa1$) can be aligned as shown in Fig. 3.10(c). Consequently, symmetric mode blocking and anti-symmetric mode transmission can be achieved. Here, the optimal condition $w_1 = 240$ nm and $L_1 = 330$ nm is found. The power transmissions of the symmetric and the anti-symmetric mode are 3% and 70%, respectively. The $|H_y|$ field distributions for the optimized notch filter are also shown in Figs. 3.11(a) and 3.11(b).

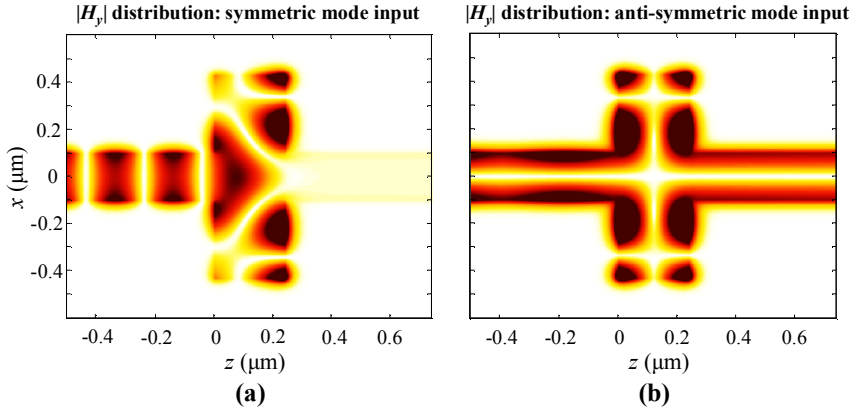


Figure 3.11 $|H_y|$ distributions for the optimized notch filter when (a) the symmetric or (b) the anti-symmetric mode is incident from the left.

3.3.4 Unidirectional mode conversion characteristics of the whole structure

By combining the stub mode converter and the mode-selective filters, unidirectional mode conversion characteristics is obtained. The filters and the stub mode converter are configured as shown in Fig. 3.7 and the constituent components are separated by 300 nm.

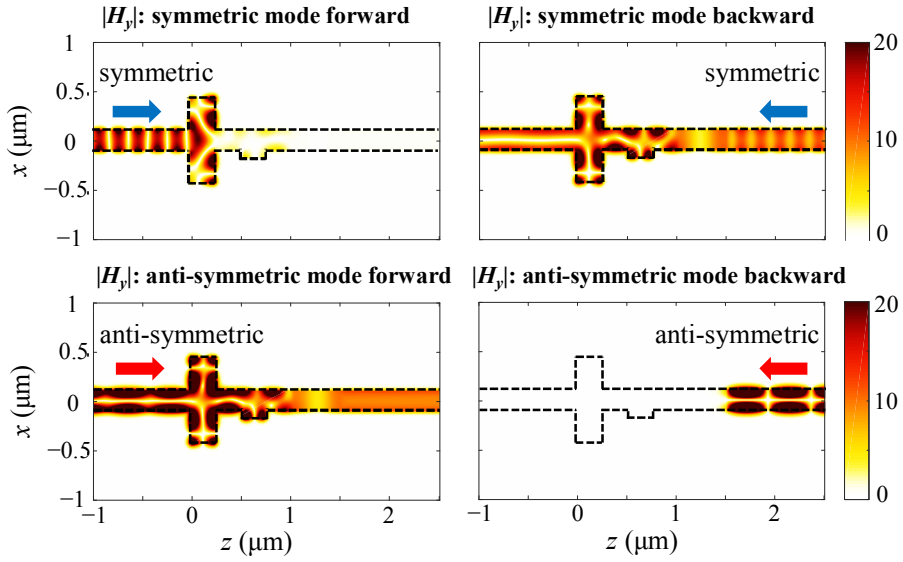


Figure 3.12 $|H_y|$ field distributions for the cases when the symmetric mode is incident from the left (upper left) and right (upper right). Those for anti-symmetric mode incidence are shown in the lower left and lower right of the figure, respectively.

Figure 3.12 shows that the symmetric mode can be converted to the anti-symmetric mode only when the light is incident from the right and the anti-symmetric mode can be converted to the symmetric mode only when the anti-symmetric mode is incident from the left. Therefore, unidirectional

mode convertor described in the subsection 3.1.2 has been successfully constructed. Note that there are standing wave patterns at the input ports even for the cases where mode converted transmission exists. Recall that this backward reflection to the input port cannot be eliminated by using mode-selective blocker. Since this reflection makes it challenging to cascade this converter with other components, I will show how one can eliminate the reflection by adjusting the intervals between the constituent components.

3.4 Tuning of the mode-selective cavity for idle scattering component elimination

3.4.1 Modelling of the mode-selective cavity and optimization conditions

In this subsection, I present an analytic model for backward reflection cancelling. Here, I show the reflection cancelling for the case when the anti-symmetric mode is incident from the left. Figure 3.13 shows the block diagram of the proposed structure. The layer 1 includes F1, region α and the series stub while the layer 2 corresponds to the F2. Each layer is characterized by the transmittance and reflectance sets such as (t_{ij}, r_{ij}) where the indices $i, j = s, a$ denote the symmetric and anti-symmetric modes, respectively. Note that the layer 1 should be characterized by two sets of transmittance and reflectance since the layer distinguishes left-to-right and right-to-left propagation cases. The layer 2 is characterized by single indexed transmittance and reflectance because there is no coupling between the two modes. Each wave component in the region between two layers is denoted by p^d ($p = s$ (symmetric), a (anti-symmetric) and $d = f$ (forward), b

((backward)) where the indices represent the spatial mode and the propagating direction.

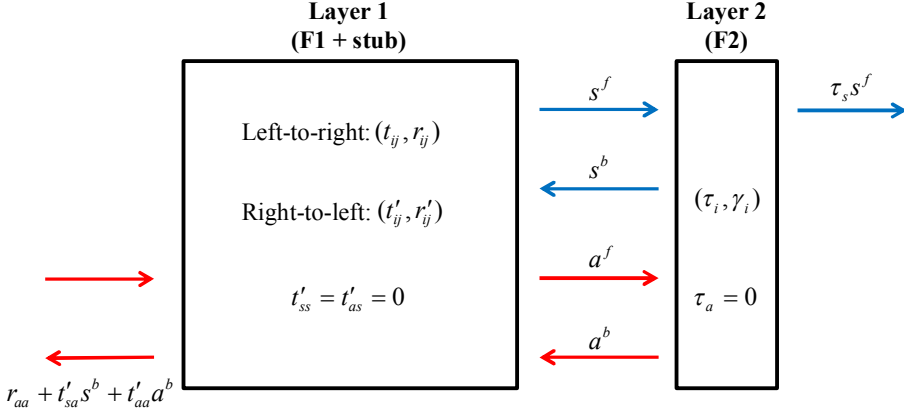


Figure 3.13 Block representation of the proposed mode converter. The layer 1 includes F1, region α and the stub while the layer 2 is the same as F2. Due to the mode-selective transmission characteristics of F1 and F2, the reflection of the symmetric mode and the transmission of the anti-symmetric mode are not expressed.

The equations for the modal coefficients are given as follows:

$$\begin{bmatrix} 1 - r'_{ss} \gamma_s \Phi_s & -r'_{as} \gamma_a \Phi_a \\ -r'_{sa} \gamma_s \Phi_s & 1 - r'_{aa} \gamma_a \Phi_a \end{bmatrix} \begin{bmatrix} s^f \\ a^f \end{bmatrix} = \begin{bmatrix} t_{as} \\ t_{aa} \end{bmatrix}, \quad (3.1)$$

$$\begin{bmatrix} \gamma_s \sqrt{\Phi_s} & 0 \\ 0 & \gamma_a \sqrt{\Phi_a} \end{bmatrix} \begin{bmatrix} s^f \\ a^f \end{bmatrix} = \begin{bmatrix} s^b \\ a^b \end{bmatrix}, \quad (3.2)$$

where I defined the phase factors $\Phi_i = \exp(2ik_i L_\beta)$ ($i = s, a$) and k_s, k_a are propagation constants of symmetric and anti-symmetric modes, respectively. As described in the previous section, the mode-selective filters F1 and F2 are designed to block the MIM symmetric and anti-symmetric mode, respectively ($t'_{ss} = t'_{as} = \tau_a = 0$).

By using Eqs. (3.1) and (3.2), I sequentially determine L_α and L_β for zero reflection instead of investigating the whole two dimensional parameter space by using the analytic expression of the reflectance. Though the full expression for zero reflection condition is complicated, it can be greatly simplified when we assume $\gamma_s = 0$. It was found in the subsection 3.3.2 that this condition is achievable by choosing the length of SiO₂ core. Under the assumption, the expression for the complex reflection coefficient R is given as:

$$R = r_{aa} + \frac{t_{aa}t'_{aa}\gamma_a\Phi_a}{1-r'_{aa}\gamma_a\Phi_a} = \frac{r_{aa} + (t_{aa}t'_{aa} - r_{aa}r'_{aa})\gamma_a\Phi_a}{1-r'_{aa}\gamma_a\Phi_a}. \quad (3.3)$$

The easiest way to modify R would be tuning the phase factor Φ_a which depends on L_β . Though we must consider the propagation loss, the round trip propagation loss in the region β has the order of 5%. Hence, I simply approximate $|\Phi_a| \approx 1$ and express the zero reflection condition as follows:

$$f(L_\alpha) \equiv \frac{1}{|r_{aa}(L_\alpha)|} \left| \det \begin{bmatrix} t_{aa}(L_\alpha) & r_{aa}(L_\alpha) \\ r'_{aa}(L_\alpha) & t_{aa}(L_\alpha) \end{bmatrix} \right| = 1, \quad (3.4)$$

where I used $|\gamma_a| \approx 1$ and the Lorentz reciprocity ($t_{aa} = t'_{aa}$) here. When the Eq. (3.4) is satisfied, there exists L_β such that $R(L_\beta) = 0$ is satisfied. I note that the Eq. (3.4) resembles the perfect absorption condition for 1 port waveguide system. In this case, the determinant of the partial scattering matrix is smaller than unity for two reasons: material loss and energy leakage to the symmetric mode. The in-coupling rejection rate (r_{aa}) should be small to meet the large energy loss of Fabry-Pérot cavity for the anti-symmetric mode formed at the waveguide region β .

3.4.2 Cavity length optimization

In this subsection, I firstly analyze the layer 1's characteristics as an in-coupler for the Fabry-Pérot cavity at the region β . As pointed out in the previous subsection, the small reflectance $r_{aa}(L_a)$ is required to meet the reflection cancelling. Figure 3.14(a) shows the major terms that contribute to the $r_{aa}(L_a)$. The first term corresponds to the initial reflection at the notch filter and the second term corresponds to the reflection at the stub structure. Due to the presence of couplings to multiple modes, higher order scattering terms are generally negligible.

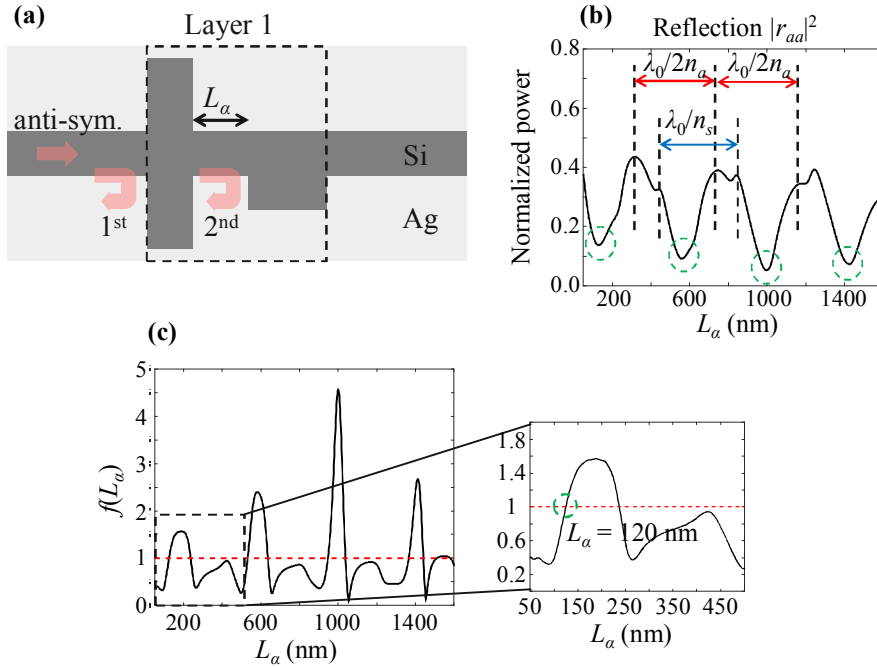


Figure 3.14 (a) Schematic of the layer 1 and major terms which contribute to r_{aa} . (b) $|r_{aa}|^2$ and corresponding (c) $f(L_a)$ depending on L_a .

Figure 3.14(b) shows the reflected power $|r_{aa}|^2$ that depends on L_a and it was found that the major oscillation has period equal to the half of the effective wavelength of the anti-symmetric mode at the main waveguide. The corresponding $f(L_a)$ is plotted in Fig. 3.14(c). As expected, the condition Eq. (3.4) is satisfied in the vicinity of the reflectance dips in Fig. 3.14(b). Here, I chose $L_a = 120$ nm, which is the shortest length that satisfied the design condition.

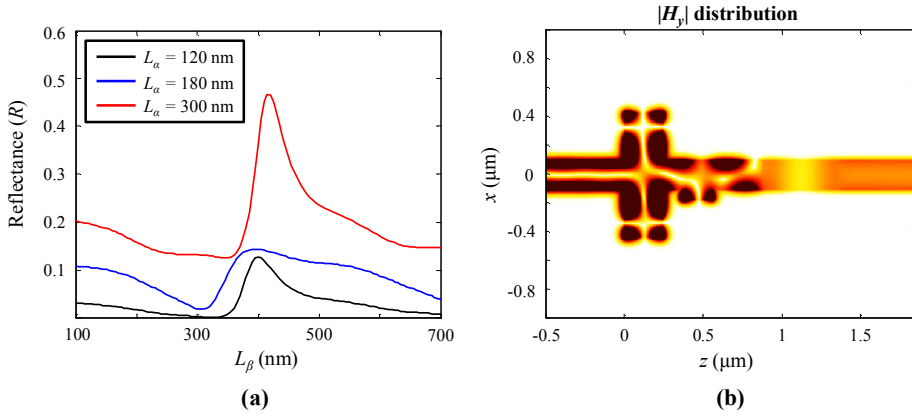


Figure 3.15 (a) Reflected power of the anti-symmetric mode for the whole structure as a function of L_β . (b) $|H_y|$ field distribution for the optimized structure when the anti-symmetric mode is incident from the left.

After setting L_a , the reflection of the anti-symmetric mode at the anti-symmetric mode incidence is calculated for varying L_β . As Fig. 3.15(a) shows, the reflection of the anti-symmetric mode can be smaller than 0.1% by appropriately tuning L_β . In order to check the validity of the theoretical analysis used to determine L_a , similar graphs for different values of L_a are plotted as shown in Figs. 3.15(a). Indeed, the reflectance cannot be completely suppressed when the condition Eq. (3.4) is not satisfied. When L_β

is set at 320 nm, the reflection is successfully suppressed and the overall conversion efficiency is 47%. The $|H_y|$ field distribution of the optimized structure for anti-symmetric mode incidence from the left is shown in Fig. 3.15(b). Therefore, compact unidirectional plasmonic mode converter with efficiency 47% and no residual scattering is designed in the footprint shorter than 1.5 μm .

3.5 Application of the design strategy to out-coupler design problem

The design strategy, which exploits blockers and destructive interference, can also be used for other mode conversion structures. As an example, I design an out-coupling structure for nanoslit which converts plasmonic mode in nanoslit to free space modes.

3.5.1 Scattering components at the end of nanoslit

Before introducing the proposed structure, it is necessary to consider the out-coupling characteristics from MIM waveguide to free space. Throughout the section 3.5, the wavelength is fixed at 633 nm and the permittivity of metal is modeled by using the Drude model; $\varepsilon(\omega) = \varepsilon_\infty - \omega_p^2/(\omega^2 + i\Gamma\omega)$, where the parameters of silver are chosen ($\varepsilon_\infty = 3.7$, $\omega_p = 9$ eV, $\Gamma = 0.018$ eV [65]). The schematic diagram in Fig. 3.16(a) shows the scattered wave components when the MIM (Ag-silica-Ag) plasmonic mode is incident from the bottom. At the end of the waveguide, the input mode is scattered into three components: the backward reflection, the free space radiation and the single interface SPP mode at the metal/air interface. Figure 3.16(b) shows the power flows of scattered waves normalized by the incident power. The

reflection increases as the slit width (w) decreases and that is the main reason for the decrease of the radiation power. The SPP mode also takes away about 20% of the incident power, which further decreases the radiation power. Therefore, suppression of reflection and SPP leakage are necessary to enhance out-coupling efficiency. As a design example, I set the slit width at $w = 50$ nm, where the normalized power flows of the backward reflection and the SPP leakage are 51% and 18%, respectively. However, note that my design scheme can be applied to different widths of the slit, as long as the single-mode condition for MIM waveguide is satisfied.

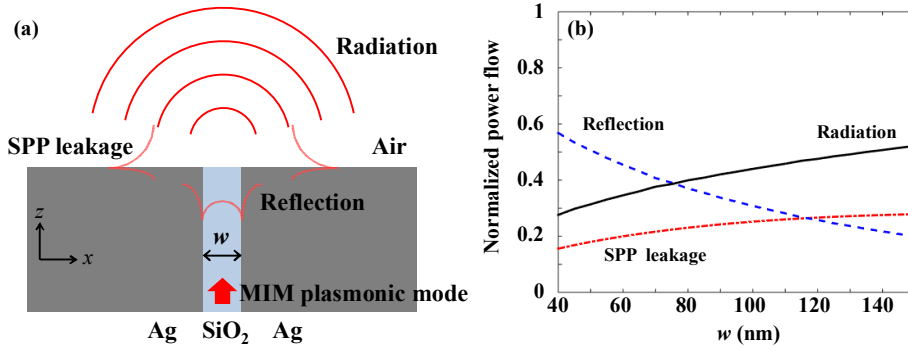
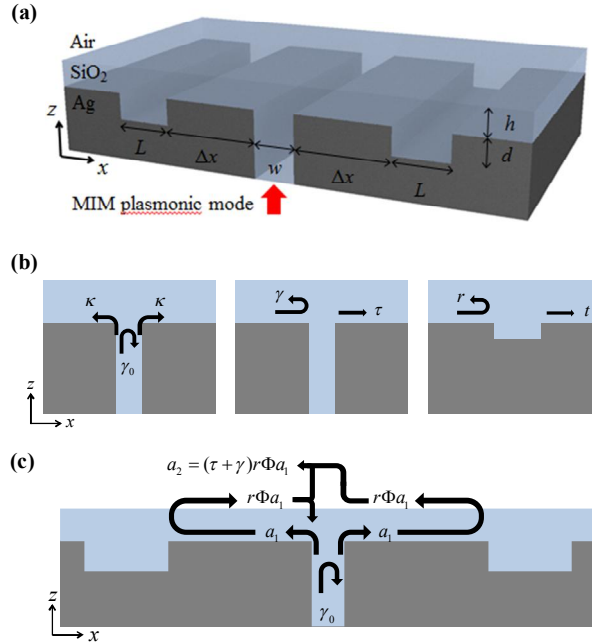


Figure 3.16 (a) Scattering at the end of nano-slit when MIM plasmonic mode is launched from the bottom ($\epsilon_{\text{Ag}} = -17.3 + 0.193i$, $\epsilon_{\text{silica}} = 2.25$). The scattered wave can be decomposed into free space modes, SPP mode and backward reflection. (b) Dependence of power proportion for each scattered wave component.

3.5.2 Trench-type antenna near nanoslit and its working principle

To eliminate the reflection and SPP leakage, a trench-type antenna structure is proposed as shown in Fig. 3.17(a). The trenches are placed on both sides of the waveguide to block the SPP mode [66-68]. Due to the cavity formed by the trenches, SPPs are trapped between the trenches until

they finally escape into free space or return back to the MIM waveguide. By properly adjusting the trench positions (Δx), it is possible to reduce the reflection of the overall structure due to interference of the initial reflection at the waveguide exit and the contribution of the returning SPPs trapped between the trenches. Furthermore, for near-complete cancellation of the reflection, a dielectric (silica) coating is added, because the thickness of the coating (h) can be used to balance the reflection and the SPP leakage at the exit of the nano-slit [69].



The complete out-coupling conditions can be expressed in terms of scattering coefficients. Figure 3.17(b) shows the scattering coefficients needed to calculate the reflection and SPP leakage of the whole structure. κ and γ_0 denote respectively the complex scattering coefficients of SPP leakage and backward reflection at the nano-slit without trenches, when MIM plasmonic mode is launched from the bottom. (τ, γ) and (t, r) are respectively the transmittance and reflectance pairs at the nano-slit and the trench for the SPP incidence from the left. First, the blocking condition of leakage SPP can be easily written as $|t| \approx 0$. Next, the zero-reflection condition can be obtained by calculating complex reflection coefficient of the overall structure. Since the configuration of the proposed structure and the waveguide input possesses the same mirror symmetry, complex coefficients of the SPPs which experienced $n-1$ times of reflections at the trenches (a_n) can be described by single recursive relation. As shown in Fig. 3.17(c), $\{a_n\}$ is a geometric sequence that satisfies $a_{n+1} = (\tau+\gamma)r\Phi a_n$ ($a_1 = \kappa$) where $\Phi = \exp(2ik_{\text{SPP}}\Delta x)$ and k_{SPP} is the complex propagation constant of the SPP mode at the air-dielectric-metal waveguide. Hence, the complex reflectance of the total structure is given as:

$$R(\Phi) = \gamma_0 + 2\kappa r \Phi \sum_{n=1}^{\infty} a_n = \gamma_0 + \frac{2\kappa^2 r \Phi}{1 - r(\tau + \gamma)\Phi}. \quad (3.5)$$

While Δx does not have to be longer than the effective wavelength of SPP ($\lambda_{\text{SPP}} = 2\pi/\text{Re}\{k_{\text{SPP}}\}$) for full-phase adjustment of the Φ , typical propagation lengths of SPPs are as large as tens of λ_{SPP} at the operating wavelength. Therefore, it is valid to assume that $|\Phi| \approx 1$ and the condition for zero reflection ($R(\Phi) = 0$) can be obtained as follows:

$$|\Phi| = \frac{1}{|r|} \cdot \left| \frac{\gamma_0}{\gamma_0(\tau + \gamma) - 2\kappa^2} \right| \approx 1. \quad (3.6)$$

When Eq. (3.6) is satisfied, the reflection becomes nearly zero for some Δx . To sum up, the conditions for complete out-coupling can be expressed as $|t| = 0$ and $|r| \approx |r_0|$, where the reflectance r_0 is defined as $r_0 = \gamma_0/[\gamma_0(\tau + \gamma) - 2\kappa^2]$. It should be noted that t and r depend on L , d and h , while r_0 depends only on h , because the scattering coefficients γ_0 , γ , τ and κ are not related to the trench. The condition $|t| = 0$ can be satisfied by adjusting the trench parameters L and d . As will be shown in the optimization procedure in the next section, there are discrete sets of (L_0, d_0) which lead to $|t| = 0$. When the pairs (L_0, d_0) for a fixed value of h are found, there remain very few choices to balance $|r|$ and $|r_0|$. Hence, the dielectric coating thickness (h), which affects both $|r(L_0(h), d_0(h), h)|$ and $|r_0(h)|$, is used as the balancing parameter of reflectance.

Based on the foregoing observations, the design procedure of the proposed structure can be established. First, the target reflectance $r_0(h)$ should be extracted from the scattering coefficients that depend on the dielectric coating thickness. Next, the maps of t and r on the (L, d) parameter space are obtained for different dielectric coating thicknesses to determine the optimal h . Then, appropriate value of Δx should be found to minimize the reflection. After parameter optimization, the radiation pattern from the structure is discussed.

3.5.3 Design of the SPP blocking trench

As the first step of optimization, the target reflectance r_0 depending on the thickness of the dielectric coating layer is calculated. Only those coating thicknesses which are less than 200 nm are considered here, because the

higher order bound modes can be supported by air-dielectric-metal waveguide when h becomes more than 250 nm [70]. In such a situation, it would be much difficult to block multiple modes by using a single trench structure and the design procedure based on Eqs. (3.5) and (3.6) will no longer be valid. Figure 3.18(a) illustrates the dependence of $|\gamma_0|^2$ and $2|\kappa|^2$ on the coating thickness, and the solid line in Fig. 3.18(b) shows the corresponding dependence of $|r_0|$ due to the change in scattering coefficients. One can predict that decrease of $|\gamma_0|$ and increase of $|\kappa|$ would lead to decrease of $|r_0|$, because less returning SPP is required to cancel the reflection. The tendency that appears in Figs. 3.18(a) and 3.18(b) agrees with the expected trend.

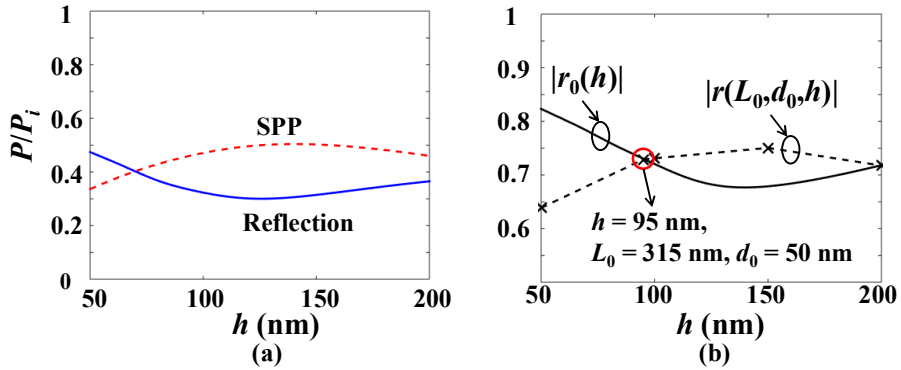


Figure 3.18 (a) The reflection ($|\gamma_0|^2$, solid line) and the SPP coupling ($2|\kappa|^2$, dashed line) at the exit of nano-slit without the trenches. (b) The h dependence of the target reflectance ($|r_0|$, solid line) calculated by Eq. (3.6) and the SPP reflectance ($|r|$, dashed line) at the trench when $|t| \approx 0$ is satisfied.

After the extraction of r_0 , SPP transmission and reflection coefficients depending on the length and depth of the trench for different coating

thicknesses (50 nm, 100 nm, 150 nm, and 200 nm) are calculated. For each coating thickness, zero SPP transmission condition and the SPP reflectance corresponding to the design condition was extracted. Zero SPP transmission condition can be found for each coating thickness where two pathways destructively interfere. Figures 3.19(a) and 3.19(b) show the two pathways for SPP transmission through the trench.

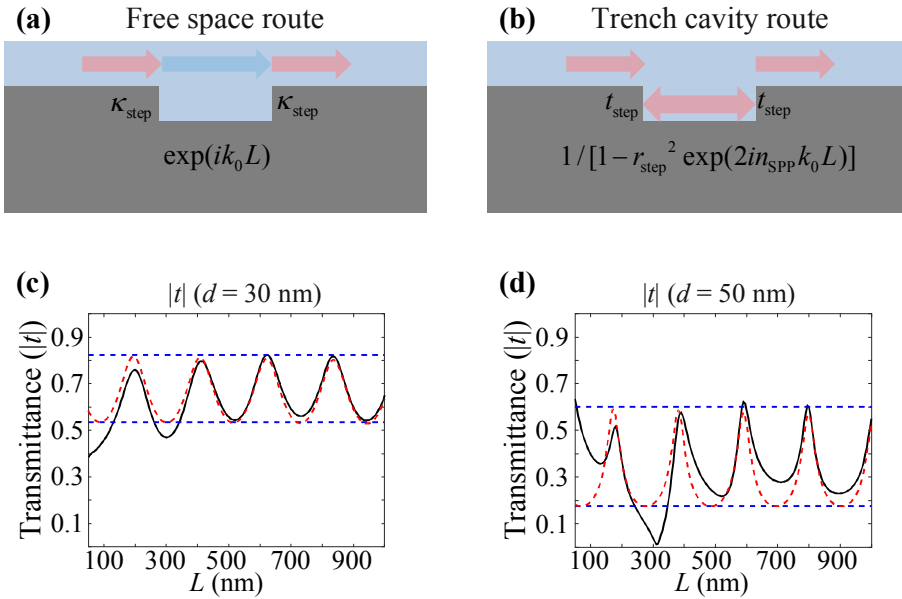


Figure 3.19 Two routes for SPP transmission through the trench structure (a) the free space route and (b) the trench cavity route. κ_{step} , t_{step} and r_{step} represent scattering coefficients at the edge of the trench. SPP transmittance as a function of trench length L when the depth of the trench is fixed at (c) $d = 30$ nm and (d) $d = 50$ nm. The solid black line represents SPP transmittance of the trench and the dashed red line represents the theoretical fitting of the trench cavity route.

When the depth of the trench is too shallow, the SPP couples into the SPP mode in the trench almost adiabatically, resulting in high SPP transmittance as shown in Fig. 3.19(c). Hence, zero SPP transmittance condition is hardly found. As the depth of the trench increases, the transmittance decreases due to the weaker in-coupling to the SPP mode in the trench. Due to the wide range of amplitude and phase covered by the trench cavity term, zero reflectance condition can be found in the trench length range where free-space route does not decay much as shown in Fig. 3.19(d).

Since $|r(L_0, d_0, h)|$ and $|r_0(h)|$ are comparable at the marked point, one can expect that the optimal h , which satisfies $|r|=|r_0|$, can be found. The marked zero transmittance point shifts as h varies and the change of reflectance $|r(L_0, d_0, h)|$ is shown in Fig. 3.18(b). Fine tuning near $h=100$ nm reveals that $h=95$ nm satisfies the condition $|r|=|r_0|$; the corresponding L_0 and d_0 for zero SPP transmittance are 315 nm and 50 nm, respectively.

3.5.4 Radiation pattern from the optimized structure

Figure 3.20(a) shows the normalized power flows for the reflection and SPP leakage of the whole structure, depending on the trench position (Δx). The reflection dips appear in periodic fashion and the period agrees with half of the SPP wavelength (227 nm, $n_{\text{SPP}} = 1.39$), as can be expected from Eq. (3.5). The reflected powers at $\Delta x = 300$ nm and 530 nm are 1.0% and 0.4%, respectively. The peaks of the SPP leakage also appear periodically due to Fabry-Perot resonance between the trenches, but the peak values near the near-zero reflection dips are below 0.8%. The loss of the overall structure is lower than 10% in both cases. Thus, an efficient out-coupler without

reflection and SPP leakage is successfully designed.

Figure 3.20(b) shows the $|H_y|$ field profile when the trenches are removed from the optimized structure. Leakage SPPs and the beating pattern inside the nano-slit, due to backward reflection, are clearly visible. In contrast to this, in the $|H_y|$ field profiles of the optimized structures shown in Figs. 3.20(c) and 3.20(d), leakage SPP and the beating are barely visible.

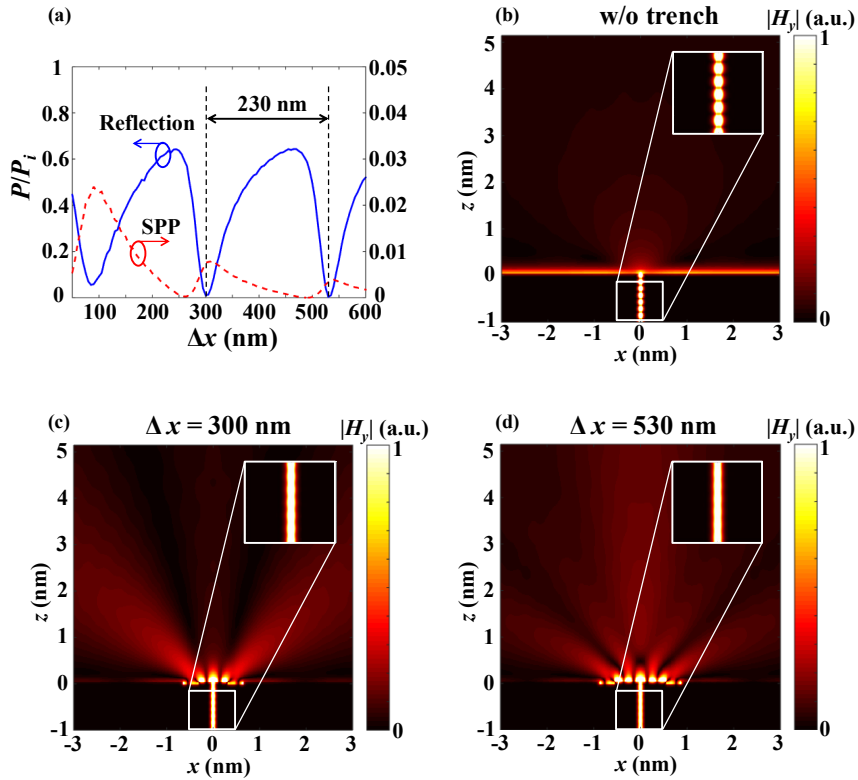


Figure 3.20 (a) Normalized power flows of the reflection (solid line) and SPP leakage (dashed line) varying with the trench position (Δx). $|H_y|$ field distributions when (b) the trenches are removed from the optimized structure, and for the two optimized cases when (c) $\Delta x = 300$ nm and (d) $\Delta x = 530$ nm.

Though two values of Δx give similar out-coupling performance in terms of reflection and SPP leakage, their radiation patterns are quite different and such difference should be taken into account in practice, because the numerical aperture of optical measurement system is limited. While the total out-coupling powers are almost the same, the main lobe strength is stronger when Δx is chosen as 530 nm, rather than 300 nm. The dependence of radiation pattern on Δx can be understood from the fact that total radiation is the sum of three wave components: the radiation of MIM plasmonic mode from the nano-slit when the trenches are absent, the scattering of the returning SPPs at the exit of the nano-slit and the scattering at the trenches. As Δx increases, the relative phase of the scattered wave from the trenches is delayed and the phase delay, in turn, changes the interference pattern.

3.6 Conclusion

In this chapter, I proposed a design scheme for compact mode converter with asymmetric transmission and reflection characteristics. The design scheme uses mode-selective blockers and asymmetric configuration of the mode-selective blockers in a plasmonic waveguide led to unidirectional mode conversion. Mode-selective filters, one of which exploits side-coupled cavity resonances and the other one based on cut-off of anti-symmetric plasmonic waveguide mode, have been designed separately and configured on the both sides of simple stub mode converter. The unidirectional mode conversion characteristic has been verified by simulation. By adjusting the cavity lengths, it was found that the reflection of the anti-symmetric mode can be annihilated by destructive interference. The designed structure occupies only $1.35\text{ }\mu\text{m}$ in its longitudinal direction and has conversion efficiency of 47% while the sum of all residual output power is below 0.5%. In addition to plasmonic waveguide mode converter, the design strategy using mode-selective blockers and destructive interference has been applied to the out-couplers for nanoslits proving that the proposed design scheme can be applied to various mode converter design problems. Potentially, the proposed scheme can open a way to integration of asymmetric mode converters. For instance, the proposed plasmonic mode converter can be used for preventing amplification of residual reflection, thereby relaxes the need for optical isolators required in active nanoscale photonic systems.

Chapter 4 Unidirectional launching of polarization–converted waves from bilayer metasurfaces

4.1 Introduction

4.1.1 Properties of thin, single layer metasurfaces and the symmetry of scattering characteristics

In this subsection, I review some basic properties of thin, single layer metasurface and introduce notations to be used throughout this chapter. As shown in Fig. 4.1(a), consider a metasurface embedded in a homogeneous medium and assume that a polarization eigenmode is normally incident on the metasurface from the bottom. Here, I simply assume that polarization eigenmodes are x , y polarizations. Interestingly, it is known that the nanoantennas scatter the incident light in a symmetric fashion as follows:

$$\begin{aligned} t_{x,y} &= t_0 + p_{x,y}, \\ r_{x,y} &= r_0 + p_{x,y}, \end{aligned} \tag{4.1}$$

where t_0 and r_0 are background transmittance and reflectance which correspond to the t and r for metallic film without nanoantenna patterns. The reason for symmetric scattering can be attributed to planar induced current distribution. For this reason, two-dimensional thin nanoantenna arrays embedded in homogeneous medium generate the same wavefronts on both sides of the planar structure. In this chapter, I break this symmetry by using a

bilayer structure for a new type of multiplexing scheme.

To return back to the metasurface modelling, it can be easily found out that $t - r = t_0 - r_0$ regardless of the scattering amplitude p . Let's denote this antenna-independent parameter as Ψ . One observation that can be made on Ψ is that $|\Psi| \approx 1$ for thin surfaces. This condition can be derived by assuming negligible loss ($|t_0|^2 + |r_0|^2 \approx 1$) and exploiting the phase relation for symmetric configuration ($\angle t_0 - \angle r_0 = \pm\pi/2$).

Due to the energy conservation ($|t_0+p|^2 + |r_0+p|^2 \leq 1$) it can be found that the scattering amplitude should be confined in the following circle in the complex plane:

$$p = -\frac{t_0 + r_0}{2} + z \quad (|z| \leq 1/2). \quad (4.2)$$

By using Eq. (4.2), the transmittance and reflectances can be rewritten as follows:

$$\begin{aligned} t &= \Psi/2 + z, \\ r &= -\Psi/2 + z. \end{aligned} \quad (4.3)$$

The regions of realizable transmittance and reflectances are marked as shaded regions in Fig. 4.1(b). Figure 4.1(c) shows the region of realizable scattering amplitudes and typical trajectories of scattering amplitude p depending on a design parameter. Often, scattering amplitude exhibits Lorentzian-like response, i.e. $p(L) \approx p_0/(1+i(L - L_0)/\gamma)$ and consequently, the trajectory of p appears in circular shape. When the trajectory passes through the center of the realizable scattering amplitude region $(t_0 + r_0)/2$, the antenna is said to be critically coupled, since the central point corresponds to the

maximal absorption condition. Antennas that draw smaller trajectories than critically coupled antennas are said to be under-coupled and ones that draw larger trajectories are said to be over-coupled.

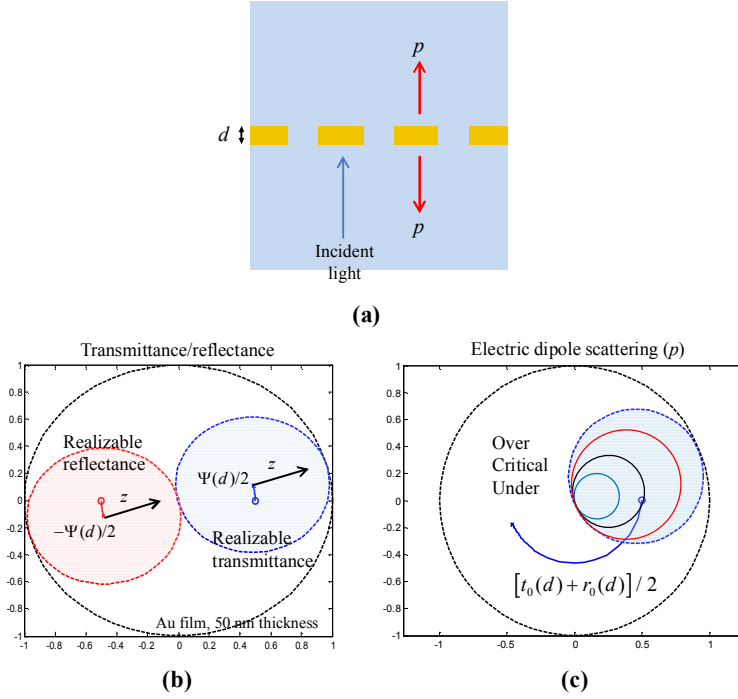


Figure 4.1 (a) Schematic of a thin metasurface where polarization eigenmode is incident from the bottom. Areas of realizable (b) transmittance, reflectance and (c) scattering amplitude for 50 nm-thick Au film at the wavelength of 980 nm.

When the material configuration surrounding the metasurface is asymmetric as depicted in Fig. 4.2(a), the scattering does not occur in symmetric fashion. Instead, the scattering amplitude ratio is related to the square root of the refractive indices. Due to this difference, the regions of realizable reflectance and transmittance have different sizes as shown in Fig. 4.2(b). Remarkably, substrate effect may give rise to asymmetric scattering

by metasurface, but the scattered power asymmetry cannot be large since naturally found materials have low refractive indices (e.g. $n_{\text{Si}} \approx 3.58$).

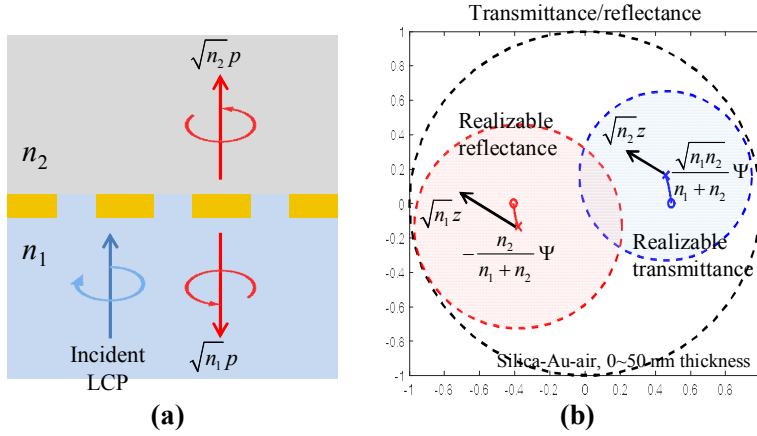


Figure 4.2 (a) Thin metasurface surrounded by heterogeneous materials where left-circular polarized (LCP) light is incident from the bottom. The polarization converted components are emitted in asymmetric fashion. (b) Realizable transmittance and reflectance for silica-Au (50 nm)-air configuration at the wavelength of 980 nm.

4.1.2 Multiplexing of the transmitted and reflected wavefronts

In this subsection, I propose a multiplexing scheme by using directional emission from metasurfaces. Figure 4.3(a) shows the schematic of the transmission/reflection multiplexing. Assume one has managed to construct two types of subwavelength unit cell structures, one of which emits cross-polarization signal only in the forward direction (T-type) and the other does it in the backward direction (R-type). Since phase (or amplitude) of the cross-polarization signal can be adjusted by rotating the antenna on the plane, it would be possible to control the transmitted cross-polarization signal and

the reflected one independently by forming a supercell structure as shown in Fig. 4.3(a). This type of new multiplexing enabled by unidirectional launching of cross-polarization signal can be called the ‘transflective multiplexing’.

As will be found in the following sections, the T-type cell and the R-type cell can be realized by bilayer metasurface structure, the simplified version of which is depicted in Fig. 4.3(b). By cancelling the reflection of the cross-polarization signal of the bilayer metallic aperture structure, T-type cell can be realized. When T-type cell is constructed, the R-type cell can be immediately designed by blocking the upper layer of the bilayer structure. In the following sections, I focus on the design of the T-type cell composed of two identical metallic apertures. The simplicity of the structure is advantageous since the fabrication can be done by a single milling process.

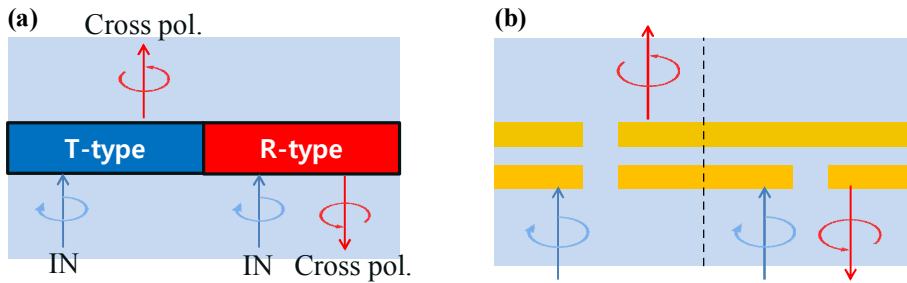


Figure 4.3 (a) Multiplexing scheme using transmission type (T-type) cells and reflection type (R-type) cells. (b) Schematic of the metallic bilayer based T-type cell and the R-type cell.

4.2 Numerical design

4.2.1 Configuration of the bilayer metasurface and reduction into a single layer metasurface design problem

Figure 4.4(a) shows the configuration of the proposed bilayer metasurface. Two identical metallic aperture arrays of thickness 50 nm are separated by a dielectric gap h . The dielectric material surrounding the metallic structure is assumed to be homogeneous SiO_2 ($n = 1.45$). Each metallic layer has unit cell structure as shown in Fig. 4.4(b) where the period is set to 760 nm which is smaller than the target design wavelength of 1550 nm. Since x and y polarizations are polarization eigenstates, single layer metasurface can be simply characterized by transmittances and reflectances for x and y polarizations: $(t_{x,y}, r_{x,y})$.

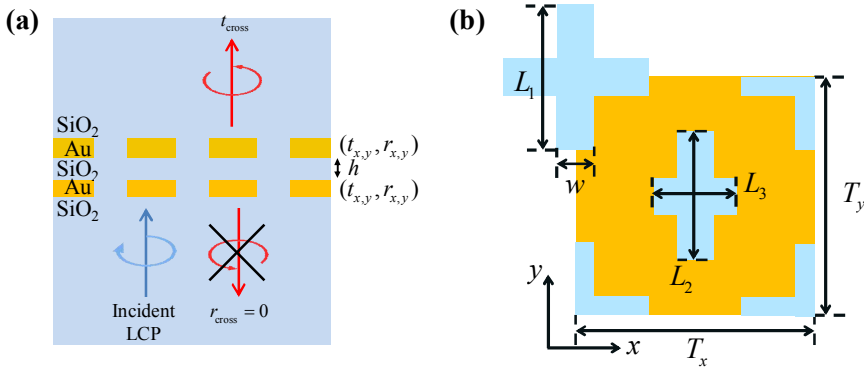


Figure 4.4 Schematic of the proposed bilayer metasurface. (a) The bilayer metasurface should be designed to emit right-circular polarized light (RCP) only in the upward direction when left-circular polarized (LCP) light is incident from the bottom. (b) Unit cell structure of the bilayer metasurface

The complex transmittance and reflectance for the whole structure can be derived by taking multiple reflections into account. Since I wish to cancel cross-polarization component in the reflection side, the total reflectance for x and y polarization must be the same. The condition can be written as follows:

$$r_x + \frac{t_x^2 r_x \zeta}{1 - r_x^2 \zeta} = r_y + \frac{t_y^2 r_y \zeta}{1 - r_y^2 \zeta}, \quad (4.4)$$

where $\zeta = \exp(2ink_0h)$ is the round trip phase factor and n is the refractive index of the spacer ($n=1.45$). $k_0 = 2\pi/\lambda$ is the wavenumber and λ is the incident wavelength. By using Eq. (4.1), Eq. (4.4) can be simplified as follows:

$$\gamma_x \gamma_y \tilde{\zeta}^2 + (1 + 2(\gamma_x + \gamma_y) + \gamma_x \gamma_y) \tilde{\zeta} + 1 = 0, \quad (4.5)$$

where $\tilde{\zeta} = \Psi^2 \zeta$, $r_{x,y} = \gamma_{x,y} \Psi$ and recall that $\Psi = t_{x,y} - r_{x,y} = t_0 - r_0$. Here, I note that it is desirable to have moderate gap distance h . If the gap distance decreases too much, the near field interaction between apertures come into play, making the Eq. (4.5) meaningless. On the other hand, when the gap distance increases too much, unwanted crosstalk between neighboring cells can occur due to the diffraction. Hence, I chose $\tilde{\zeta} = i$ so that the expected optimal gap distance is $h \approx 92$ nm ($\angle \Psi \approx 14^\circ$ for $\lambda = 1550$ nm). Choosing the phase factor gives an expression of γ_y in terms of γ_x :

$$\gamma_y = \frac{2i\gamma_x + 1 + i}{(1-i)\gamma_x - 2i}. \quad (4.6)$$

By parametrizing $\gamma_{x,y}$ with $\rho_{x,y}$ and $\phi_{x,y}$ as shown in Fig. 4.5(a), maps for ρ_y and ϕ_y can be obtained as shown in Figs. 4.5(c) and 4.5(d).

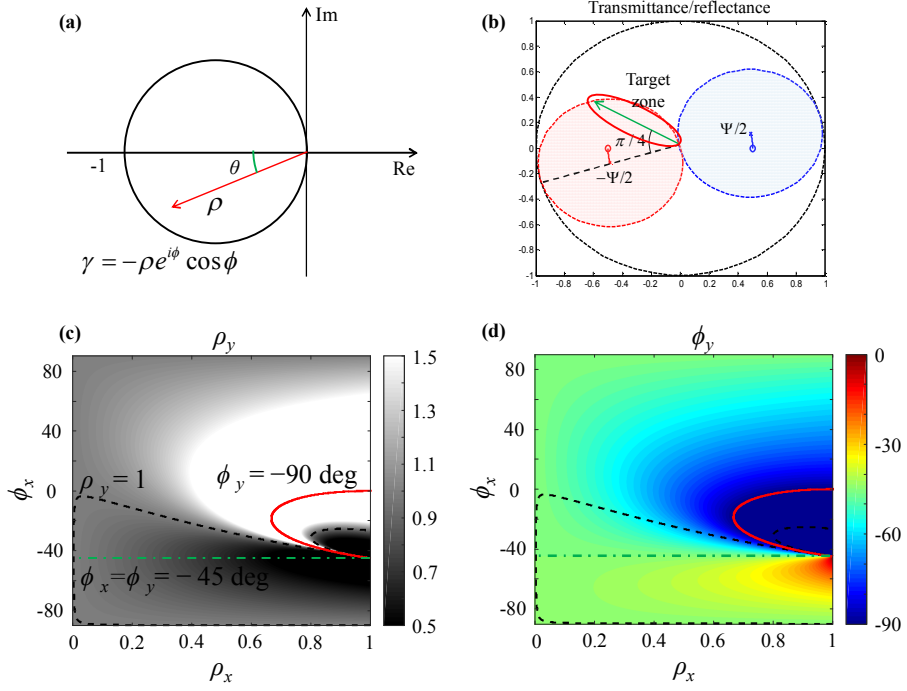


Figure 4.5 (a) Parametrization of the reflectance which covers region of realizable reflectances. (b) It can be found that the reflectance of single layer metasurface should be placed close to the green line. The maps for (c) ρ_y and (d) ϕ_y as functions of ρ_x and ϕ_x .

On the maps in Figs. 4.5(c) and 4.5(d), there are regions out of my concern in which ρ_y exceeds 1 or ϕ_y does not lie in the range from -90 deg . to 90 deg . Hence, I neglect the right side of the red solid contour and the upper side of the black dashed contour. In the region below the black dashed line, it can be found that the desired set of reflectances is found near the line $\phi = -45 \text{ deg}$, which is marked as green line on Fig. 4.5(b). Therefore, it is required to bring the reflectance of the single layer to the upper-right side of the green line.

4.2.2 Unit cell structure and gap distance optimization

As have been analyzed in the previous subsection, the reflectance for the single layer metasurface should be brought close to the $\phi = -45$ deg. line. Since the reflectance of metallic film is generally large, strong coupling of nanoantenna is necessary. For strong coupling, the antennas should be closely packed to enhance transmittance at the resonance. Therefore, I employed the unit cell shown in Fig. 4.4 which consists of anisotropic antennas which generate cross-polarization and isotropic antennas to enhance background transmission. Actually, alternative arrangement of anisotropic antenna and isotropic antenna is advantageous in terms of amplitude distortion compensation which will be explained in the subsection 4.2.3.

I set the target design wavelength at 1550 nm and the gold is selected for metallic material. For modelling of permittivity, I used the experimental data reported by Palik [71]. The widths of apertures (w) are fixed to 100 nm. Transmittance and reflectance depending on geometrical parameters have been investigated by numerical simulations which are done by frequency domain analysis of COMSOL software. The optimization procedure for the single layer metasurface is shown in Fig. 4.6. Firstly, I set the length parameters L_1, L_2, L_3 all the same and searched for the reflectance dip.

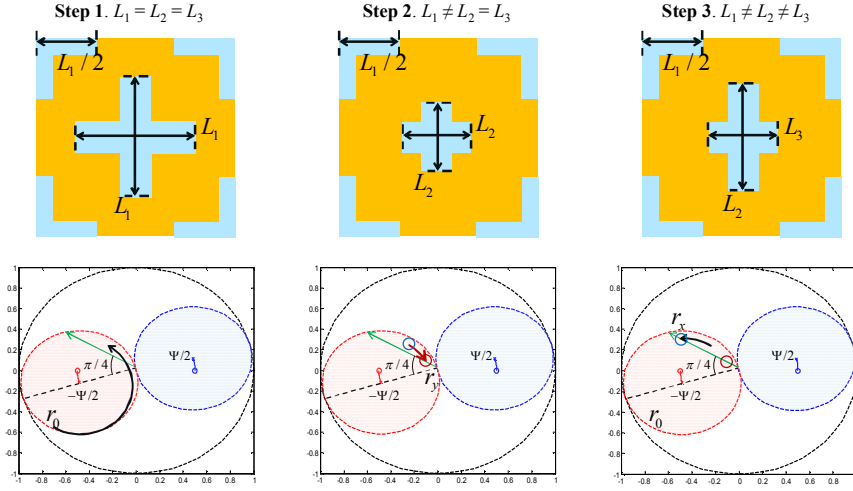


Figure 4.6 Conceptual diagrams of single layer design procedure.

Figures 4.7(a) and 4.7(b) show the reflectance of the single layer metasurface depending on the antenna length when $L_1 = L_2 = L_3$. It was found that the reflectance enters into the target reflectance region when L_1 is in the range from 420 nm to 540 nm. In my case, I set L_1 at 460 nm (Step 1). Then, L_2 and L_3 are adjusted to give anisotropy to the structure (Step 2, 3). As a result, L_3 is set at 400 nm and L_2 is set at 550 nm.

Lastly, I optimized the gap distance h by monitoring power flow of the transmitted and the reflected cross-polarization components as shown in Fig. 4.7(c). The incident polarization is set to a circularly polarized light. As expected from the analytic calculation, the optimal gap distance is found to be 90~100 nm where slight discrepancy can be attributed to the near field coupling. At the optimum, the normalized power flow of the cross-polarization component reaches 10.1% while one for the reflected cross-polarization component is only 0.53%. Therefore, the ratio of transmission and reflection is as high as 19.2.

I note that the reflected power flow for the co-polarization component is as small as the reflected power flow of the cross-polarization component (0.9%). The optimized structure is essentially an anisotropic metallic bilayer structure with low reflection which can be easily converted to reflective structure by blocking one of two layers.

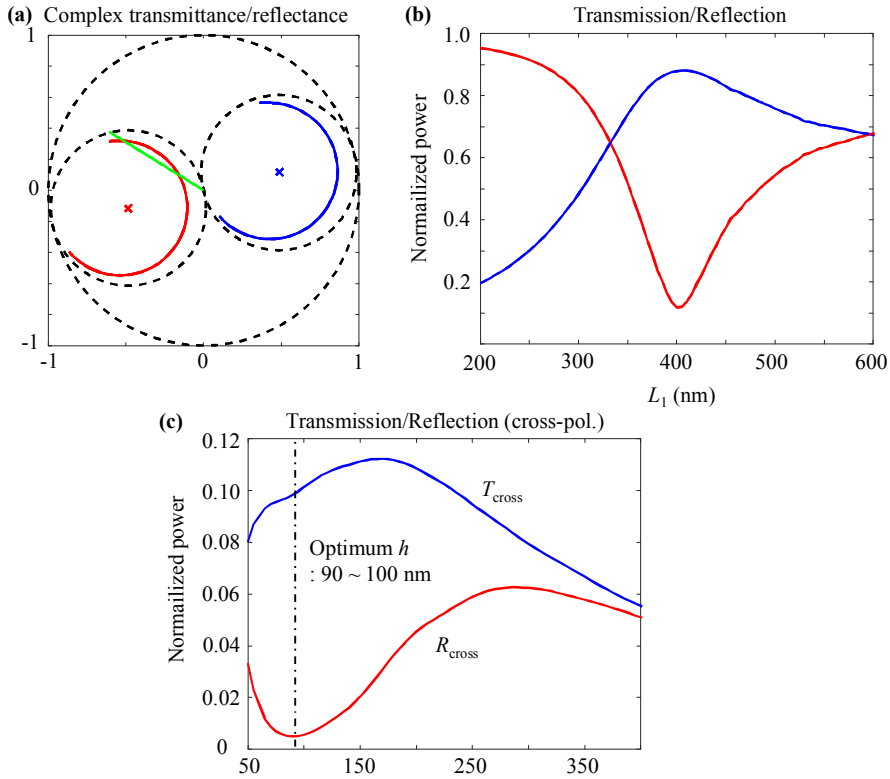


Figure 4.7 Transmittance (blue) and reflectance (red) (a) trajectories on complex plane and (b) the graph of normalized power. Normalized power flow of the cross-polarization component for the bilayer metasurface.

4.2.3 Effective material parameter point of view

The design condition for the bilayer metasurface can also be expressed in terms of effective material parameters. Assume x and y polarizations are the eigenstates of polarization which is true for the structure which I designed. The zero reflection of cross-polarization can be expressed in terms of wave impedance: $Z_x = Z_y$. If $Z_x = Z_y \neq Z_{\text{out}}$, the reflection of co-polarization would be non-zero, but no reflected cross-polarization wave can be generated by the slab. Even though the impedance condition is satisfied, it is possible to make the slab have anisotropy, i.e. $n_x \neq n_y$. In this case cross-polarization component exists in the transmitted light.

Figures 4.8(b) and 4.8(c) show the refractive index and the wave impedance of the bilayer metasurface when $L_1 = L_2 = L_3 = L$. It was found that in the neighborhood of the design condition $L = 460$ nm, the refractive index monotonically increases while the wave impedance varies slowly.

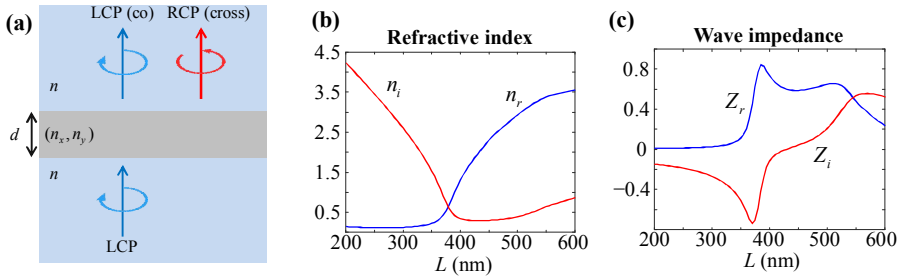


Figure 4.8 (a) Schematic diagram when the metasurface is modeled as a metamaterial slab. Effective (b) refractive index and (c) wave impedance of the bilayer structure when $L_1 = L_2 = L_3 = L$.

4.2.4 Amplitude distortion and its compensation

Though the reflection is minimized for the unit cell structure shown in Fig. 4.4(b), it does not guarantee small reflection when the anisotropic antenna is rotated as shown in the Fig. 4.9(a). When antennas are separated far enough to scatter light independently and circularly polarized light is incident, the magnitude of cross-polarization transmittance and reflectance would not change even if antenna orientation is changed. However, when antennas are closely packed, near field coupling between antennas should be taken into account [47]. Figure 4.9(b) shows that the reflected power of the cross-polarization increases up to 11.7% as the central antenna is rotated by 45 degrees. This implies that the designed unit cell structure does not work as a unidirectional cross-polarization emitter.

A simple way to compensate this distortion is to change polarization basis. In order to investigate the amplitude distortion of the designed geometric metasurface, full transmittance and reflectance matrices have been calculated for varying antenna orientation angle θ as shown in Fig. 4.9(c)-(f). From these data, one can extract cross- and co-polarization component with respect to arbitrary polarization basis $\{\mathbf{e}_i\}$.

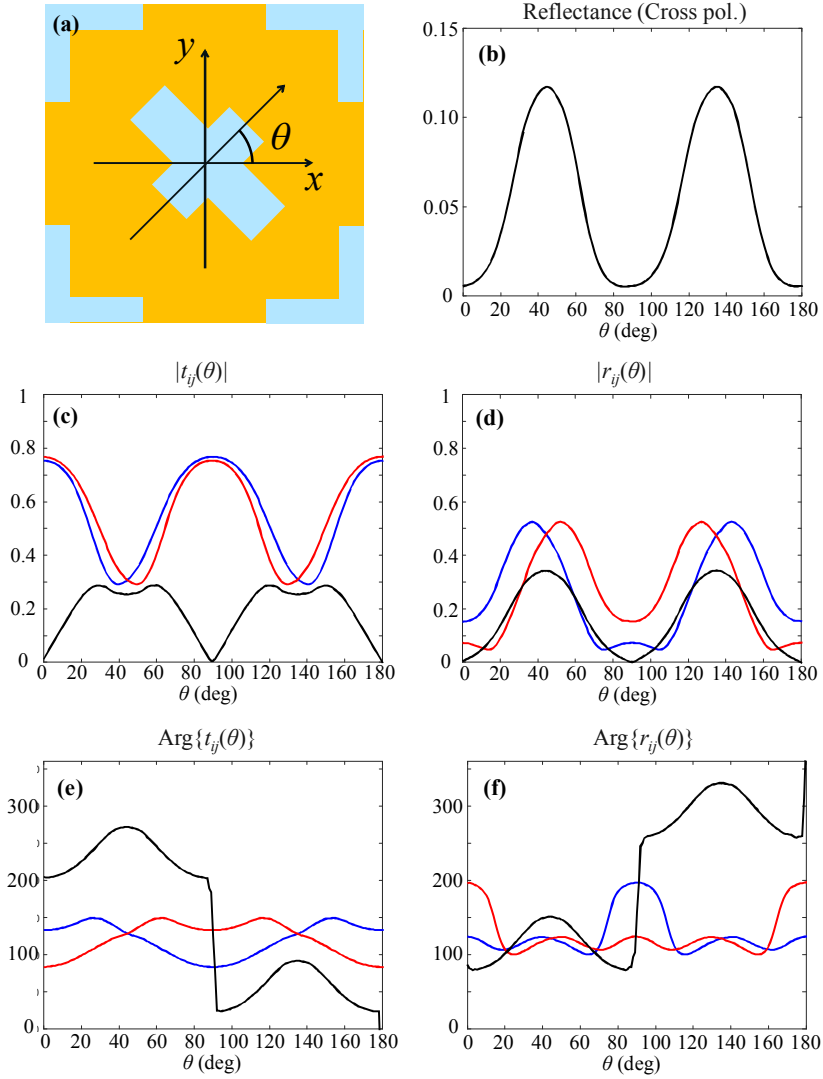


Figure 4.9 (a) Schematic of the unit cell structure with rotated anisotropic antenna. (b) Amplitude distortion of the designed metasurface. (c), (d) Amplitude and (e), (f) phase (unwrapped) of the transmittance and reflectance matrix elements. Blue, red, black lines represent the cases $i=j=x$, $i=j=y$, $i=x, j=y$, respectively.

For a geometric metasurface with negligible amplitude distortion, use of linear polarization basis results in pure amplitude control while use of circular polarization basis results in pure phase control. When elliptical polarization basis is used, the amplitude-phase dependence on antenna orientation is somewhere in between the pure amplitude control and pure phase control as expressed in Fig. 4.10(a). Therefore, proper choice of polarization basis can reduce the effect of amplitude distortion caused by near field couplings.

I found that amplitude distortion compensation can be done by using the elliptical polarization basis which can be expressed as:

$$\begin{aligned}\mathbf{e}_{45^\circ} &= \frac{1}{\sqrt{1+e^2}} \left(\frac{1}{\sqrt{2}} \begin{bmatrix} 1 \\ 1 \end{bmatrix} + \frac{ie}{\sqrt{2}} \begin{bmatrix} -1 \\ 1 \end{bmatrix} \right), \\ \mathbf{e}_{135^\circ} &= \frac{1}{\sqrt{1+e^2}} \left(\frac{e}{\sqrt{2}} \begin{bmatrix} 1 \\ 1 \end{bmatrix} - \frac{i}{\sqrt{2}} \begin{bmatrix} -1 \\ 1 \end{bmatrix} \right).\end{aligned}\tag{4.7}$$

The linear polarization basis corresponds to $e = 0$ and circular polarization basis corresponds to $e = 1$. As e decreases, the amplitude fluctuation is significantly reduced as shown in Fig. 4.10(b).

Note that the nearest antennas for every anisotropic antenna are the isotropic-type antennas which are not rotated for wavefront synthesis. This allows consistent amplitude compensation even when inhomogeneous antenna orientation distribution is given.

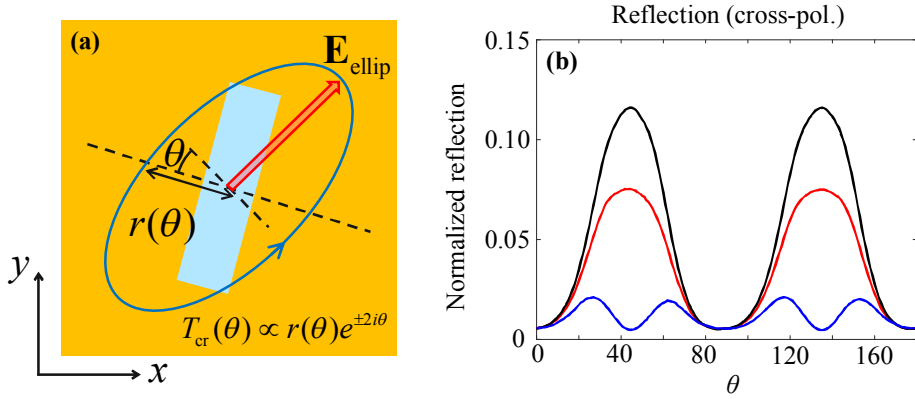


Figure 4.10 (a) Aperture antenna under elliptically polarized light incidence. (b) Reflected power flow of cross-polarization component. The blue, red and black lines represent the cases $e = 0.1$, $e = 0.5$ and $e = 0.9$, respectively.

4.3 Experiment

4.3.1 Fabrication and experimental setup

The fabrication of the proposed structure can be done by sequential deposition of Au (50 nm), SiO₂ (100 nm), and Au (50 nm) on a glass substrate followed by single step of focused ion beam (FIB, Quanta 200 3D, FEI Company) milling. For gold deposition, e-beam evaporator is used and PECVD (PlasmaPro System 100) is used for SiO₂ deposition. In order to fabricate sample as large as tens of micrometer size, patches of 8 by 8 cells (6.08 μm x 6.08 μm) are aligned as shown in Fig. 4.11. Since FIB milling results in tapered structure, I labeled fabrication conditions by the bottom aperture antenna length.

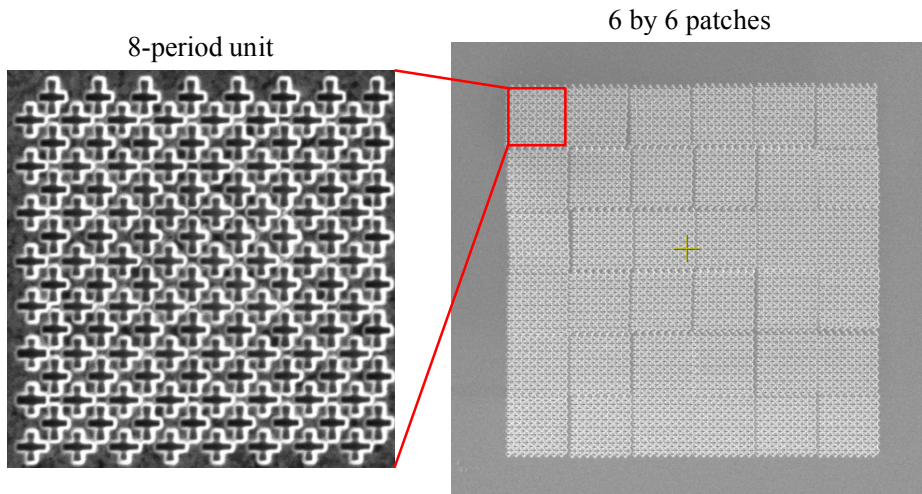


Figure 4.11 Fabricated nanoaperture array of 48 by 48 unit cells.

Figure 4.12 shows the experimental setup for measurement of transmitted and reflected signals. The 1550 nm CW laser source (fiber coupled output with collimator, 180 mW) is filtered by a linear polarizer and then converted to elliptical or circular polarization by using a quarter wave plate. The laser beam is focused on the fabricated metasurface structure by an objective lens. Then the transmitted signal and reflected signal are collected by objective lenses and imaged to IRCCD camera.

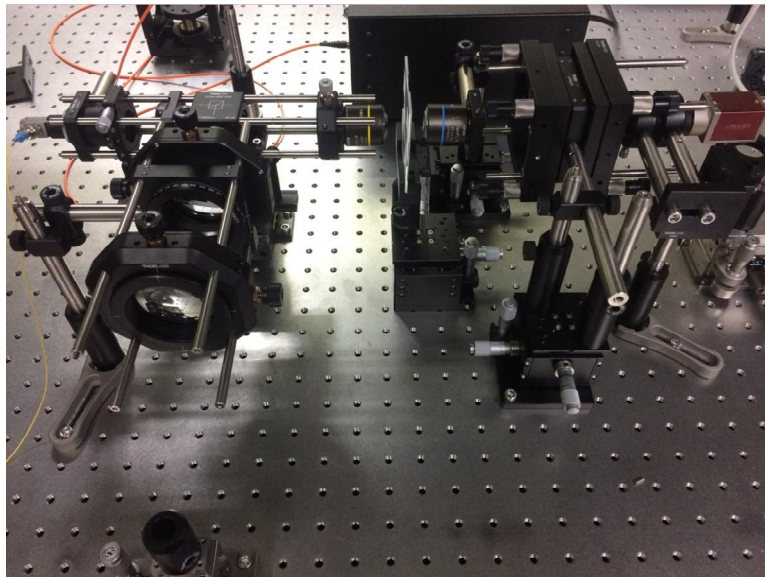
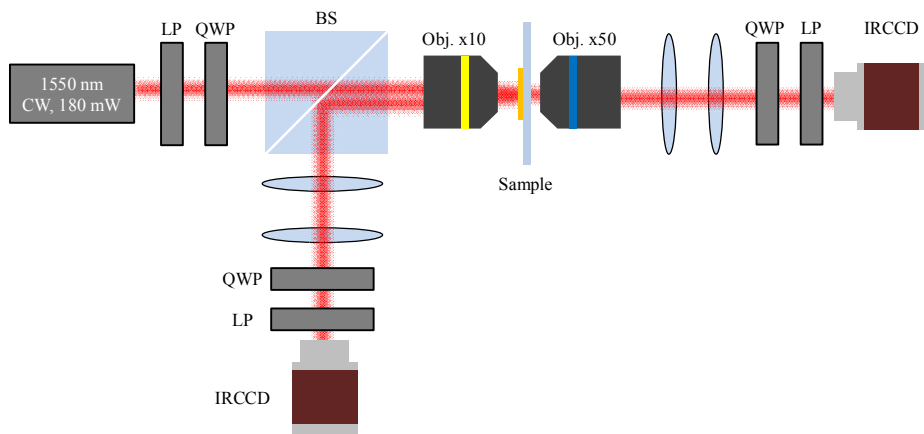


Figure 4.12 Schematic and actual realization of experimental setup for measurement of transmitted and reflected signal. The position of IRCCD and polarization filter at the detecting end are switched depending on the type of measurement.

4.3.2 Antenna resonance condition specification

Due to the difference between simulated structure and actually fabricated structure, it is necessary to search resonant condition of aperture antennas by experiment. Hence, isotropic antenna arrays ($L_1 = L_2 = L_3$) are fabricated in various aperture length conditions. The antennas are carved on Au-SiO₂-Au tri-layer and acrylate is spin coated after FIB milling for symmetric refractive index configuration. Figure 4.13 shows the fabricated sample for aperture resonance condition test. Four copies of 8 by 8 arrays are made for each of 9 antenna length conditions ranging from 300 nm to 540 nm.

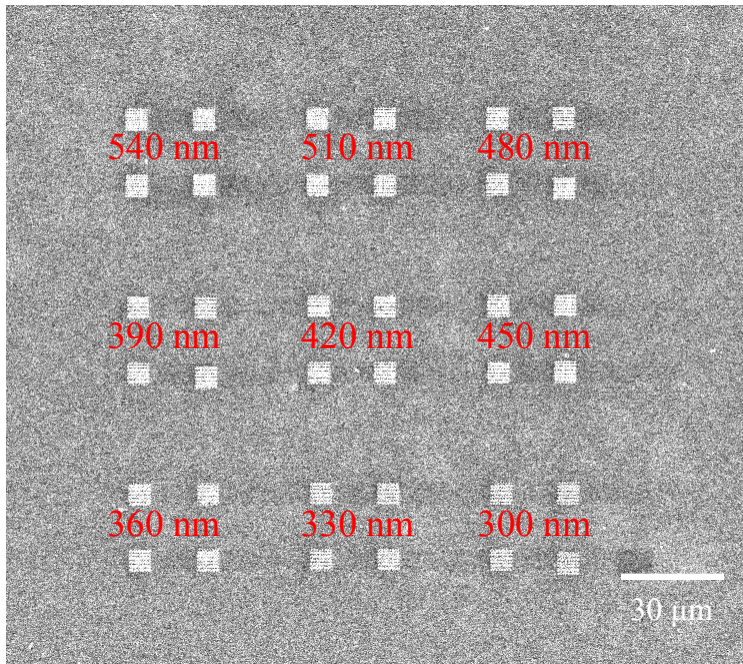


Figure 4.13 FIB image of the fabricated sample. Antenna length condition is varied from 300 nm to 540 nm and 4 copies have been fabricated for averaging.

The laser beam was illuminated from the glass substrate side and focused on the fabricated structure as shown in Fig. 4.14(b). The signs of low reflectance can be clearly observed in the form of dark images on the focused beam.

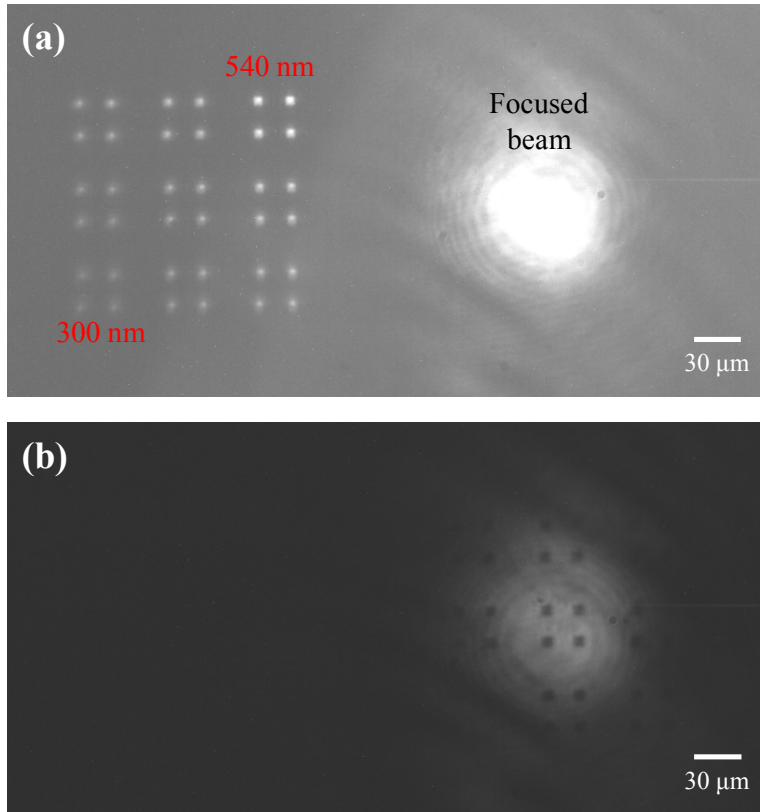


Figure 4.14 (a) Focused laser beam and the fabricated sample. Light from the fabricated antenna array came from white light source illuminated from the behind of the sample. (b) Dark images of the fabricated antenna array.

By aligning the optical beam with the center of 4 copies of antenna arrays for each antenna length condition, nine CCD images including ones in Fig. 4.15(a) and 4.15(b) were obtained. As Fig. 4.14(a) and 4.14(b) shows,

there is a noticeable difference of reflectance. Figure 4.15(c) shows the average CCD level (without dc-level elimination) inside the dark images. The result shows that the reflectance dip is in the range of 450 nm ~ 480 nm. Hence, I chose the antenna parameter L_1 as 480 nm.

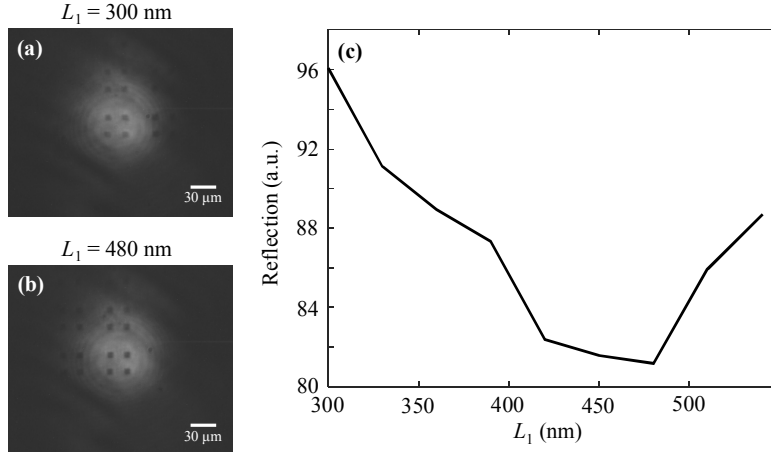


Figure 4.15 CCD images when the focused optical beam is aligned to the antenna array with the fabrication condition (a) $L_1 = 300$ nm and (b) $L_1 = 480$ nm. (c) Reflection that depends on the aperture antenna length L_1 .

4.3.3 Transmission and reflection characterization

After fixing L_1 at 480 nm, L_2 and L_3 are set at 560 nm and 420 nm, respectively. Then, 40 by 40 array sample shown in Fig. 4.16 was fabricated. In this sample, linear distribution of anisotropic antenna orientation is applied where the anisotropic antenna rotates 180 deg in an 8-period cycle. This final sample was not spin-coated with acrylate after the FIB milling process to avoid complications related to dielectric under-filling. Regarding illumination direction, I illuminated the sample from the opposite side of the glass substrate. It was observed that reflection is smaller than the case in

which the sample is illuminated from the opposite direction. This can be expected from the tapered structure of aperture antennas.

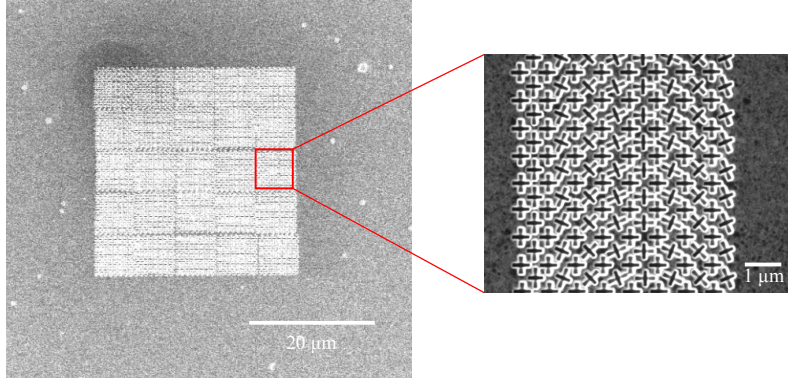


Figure 4.16 Fabricated 40 by 40 array of nanoantennas. Anisotropic antenna tilt distribution is given to induce anomalous refraction.

Figure 4.17(a) shows the image of transmitted light when no polarization filters are placed in front of the CCD camera. When polarization filtering elements are placed, fringes which signify emission in oblique direction can be clearly observed.

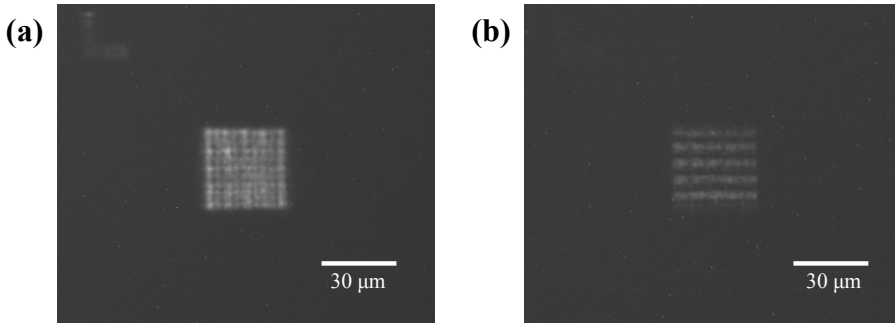


Figure 4.17 Transmitted image of the 40 by 40 cell array when (a) no polarization filtering components are placed and (b) when a linear polarizer and a quarter wave plate are placed in front of IRCCD camera.

Now, I quantify the reflection of the fabricated structure in order to confirm that the reflection has been successfully eliminated. Figure 4.18 shows the dark image of the illuminated sample. Under circularly polarized light illumination, the reflectance calculated from the CCD data in Fig. 4.18 is 8~11%. There are two main sources of reflection, one of which is the misalignment of 8 by 8 array patches. In order to avoid overlap of patches, I chose to spare a margin space (typically < 100 nm) whenever it becomes impossible to nicely align the patches due to the limit of FIB stage motor resolution. This issue can be resolved by employing fabrication method which allows large area fabrication such as electron beam lithography. The other reason for non-zero reflection is the amplitude distortion discussed in the subsection 4.2.4. Though the simulation data cannot be directly compared with the experimental data, the amplitude ripple due to near field coupling can be as high as several tenth of the reflectance minimum.

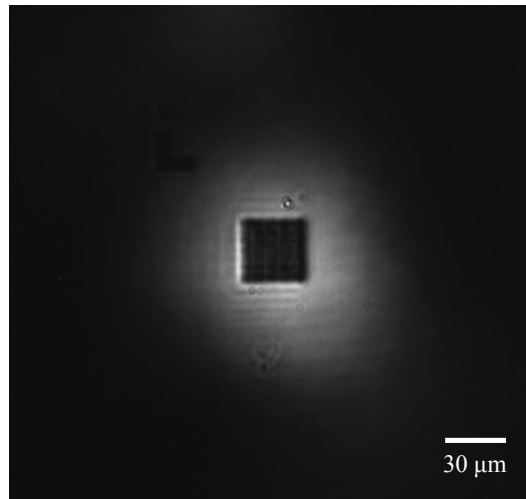


Figure 4.18 Reflected image of the 40 by 40 cell array.

4.3.4 Amplitude distortion and its reduction by polarization basis change

When co-polarized reflection is filtered out by using a linear polarizer and a quarter wave plate, a fringe which is a result of amplitude distortion can be observed. When the quarter wave plate in front of the laser input is rotated, the principal axis of elliptical polarization and eccentricity changes simultaneously. Figure 4.19 shows the images of cross-polarized reflection obtained by tuning the quarter wave plate and a linear polarizer angle at the detector side. It can be observed that the brightness and number of fringes differ depending on the polarization basis. The number of fringes changes between 5 and 10 alternatively. This phenomenon can be predicted by using numerical analysis. When the principal axes of elliptical polarization basis components are tilted by 45 deg with respect to the linear polarization eigenbasis, the numerical simulation result predicts 10 fringes. If the tilt angle of the principal axes is 22.5 deg., the numerical simulation predicts 5 fringes.

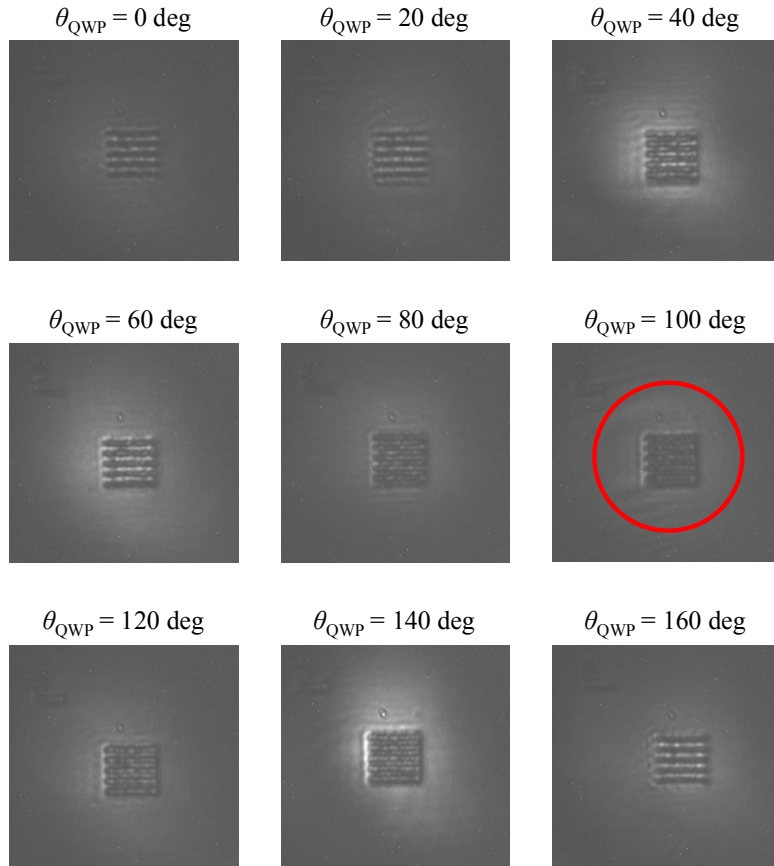


Figure 4.19 Fringe patterns of cross-polarized reflection when the quarter wave plate in front of laser source is rotated.

Regarding the brightness, the fringe pattern becomes almost invisible when the quarter wave plate is rotated by 100 deg. as marked by red circle in Fig. 4.19. Compared to other cases with 10 fringes, the amplitude ripple is significantly reduced. Hence, the concept of amplitude ripple reduction by polarization basis change has been found to be valid.

4.4 Conclusion

In this chapter, I proposed a concept of bilayer metasurface which can be used for multiplexing of transmission and reflection. In particular, I designed a transmission-type metasurface which is composed of two thin metasurfaces of 50 nm thickness separated by a SiO_2 spacer of 100 nm thickness. Since the two layers have the same shape, the bilayer design problem can be reduced to a single layer design problem by using multiple reflection calculation. The reflectance region that a single layer metasurface should access has been revealed by numerical analysis and alternating cross-antenna apertures have been used to access the target reflectance. It was found that bilayer property can be successfully designed by assembling the single layer metasurfaces and the issue of amplitude distortion is also addressed. The proposed structure has been experimentally fabricated by gold- SiO_2 -gold deposition followed by a single step FIB milling process. The measurement shows that the reflection of the bilayer structure is successfully suppressed and the amplitude distortion can be reduced by polarization basis change. The proposed structure can open a new way of metasurface function multiplexing.

Chapter 5 Summary

This dissertation covers design of asymmetric transmission and reflection characteristics of photonic mode converters in waveguide and metasurface platform. In chapter 2, a design scheme to exploit photonic dark-mode for Lorentz reciprocal, adjustable asymmetric mode converter has been proposed. After brief introduction to the dark-mode which is a photonic analogue of atomic dark-state, a design scheme using the stationary property of the dark-mode has been explained. Then, I proposed a photonic interband transition-based asymmetric mode converter in reflectionless three-mode waveguide system. Firstly, I analytically calculated the mode conversion characteristics to reveal the mechanism and design procedure of the cascaded grating mode converter. Then, I designed a grating which couples a waveguide mode to the other two modes simultaneously. The dark-mode for the waveguide grating could be specified by its stationary property. Lastly, I investigated the mode conversion characteristics both in the forward direction and the backward direction and showed that the transmission characteristics for only one direction can be controlled without disturbing the transmission characteristics for the opposite direction by tuning the length of grating which defines the dark-mode. I expect that the proposed scheme can be applied to tunable asymmetric mode converters where de-coupling of control is highly desirable.

In chapter 3, the main focus is the footprint of the plasmonic waveguide mode converters with asymmetric transmission and reflection characteristics. Firstly, the design strategy to exploit mode-selective blockers for unidirectional transmission has been explained. Then, mode-selective barriers which transmit only one of the two modes have been designed and a stub mode converter with in-complete conversion efficiency has been inserted between the two mode-selective barriers. Due to the mode-selective transmission, asymmetric transmission characteristics could be easily obtained. In addition, it was found that the backreflection toward the input port could be eliminated by adjusting the distances between barriers and stub converter. As another application of the proposed design strategy, an out-coupler for nanoslit has been designed. By using trench structure that blocks SPP leakage, the out-coupling efficiency could be boosted up to 89%. The proposed design scheme would be useful for design of compact spatial mode converter especially when residual noises are undesirable.

In chapter 4, a bilayer metasurface structure which unidirectionally launches cross-polarization component is proposed. More specifically, a metallic bilayer structure which does not emit cross-polarization component in the backward direction has been designed. The proposed structure is composed of two gold films with aperture patterns and a SiO₂ spacer. By using multiple reflection calculation, the bilayer design problem could be reduced to a single layer thin metasurface design problem. By numerical analysis and analytic calculation, the target reflectance for the single layer metasurface was found and the target reflectance can be accessed by using alternating cross-aperture cell. The structure was fabricated by film

deposition processes and a FIB milling process. By measuring the transmission and reflection characteristics, it was found that the reflection from the bilayer structure could be successfully suppressed. The issue of amplitude distortion in geometric metasurface is also discussed and the experimental verification of amplitude ripple reduction by polarization basis change was presented. The proposed bilayer can be easily re-designed to reflective structure and it is possible to multiplex transmitted signal and reflected signal by forming a supercell of transmission-type cell and reflection-type cell.

Bibliography

1. Z. Yu and S. Fan, “Complete optical isolation created by indirect interband photonic transitions,” *Nat. Photon.* **3**, 91-94, (2008).
2. H. Lira, Z. Yu, S. Fan, and M. Lipson, “Electrically driven nonreciprocity induced by interband photonic transition on a silicon chip,” *Phys. Rev. Lett.*, **109**, 033901, (2012).
3. D. L. Sounas, C. Caloz, and A. Alù, “Giant non-reciprocity at the subwavelength scale using angular momentum-biased metamaterials,” *Nat. Commun.* **4**, 2407, (2013).
4. D. L. Sounas and A. Alù, “Angular-momentum-biased nanorings to realize magnetic-free integrated optical isolation,” *ACS Photonics* **1**, 198-204, (2014).
5. L. Fan, J. Wang, L. T. Varghese, H. Shen, B. Niu, Y. Xuan, A. M. Weiner, M. Qi, “An all-silicon passive optical diode,” *Science* **335**, 447-450, (2012).
6. L. Bi, J. Hu, P. Jiang, D. H. Kim, G. F. Dionne, L. C. Kimerling, and C. A. Ross, “On-chip optical isolation in monolithically integrated non-reciprocal optical resonators,” *Nat. Photon.* **5**, 758-762, (2011).
7. L. Feng, M. Ayache, J. Huang, Y.-L. Xu, M.-H. Lu, Y.-F. Chen, Y. Fainman, and A. Scherer, “Nonreciprocal light propagation in a silicon photonic circuit,” *Science* **333**, 729-733, (2011).
8. L. Feng, Y.-L. Xu, W. S. Fegadolli, M.-H. Lu, J. E. B. Oliveira, V. R. Almeida, Y.-F. Chen, and A. Scherer, “Experimental demonstration of a

- unidirectional reflectionless parity-time metamaterial at optical frequencies,” *Nat. Mater.* **12**, 108-113, (2013).
9. S. Fan, R. Baets, A. Petrov, Z. Yu, J. D. Joannopoulos, W. Freude, A. Melloni, M. Popović, M. Vanwolleghem, D. Jalas, M. Eich, M. Krause, H. Renner, E. Brinkmeyer, and C. R. Doerr, “Comment on Nonreciprocal light propagation in a silicon photonic circuit”, *Science* **335**, 38, (2011).
 10. L. Feng, M. Ayache, J. Huang, Y.-L. Xu, M.-H. Lu, Y.-F. Chen, Y. Fainman, and A. Scherer, “Response to comments on Nonreciprocal light propagation in a silicon photonic circuit,” *Science* **335**, 38, (2012).
 11. Y. Huang, G. Veronis, and C. Min, “Unidirectional reflectionless propagation in plasmonic waveguide-cavity systems at exceptional points,” *Opt. Express*, **23**, 29882-29895, (2015).
 12. V. A. Fedotov, P. L. Mladyonov, S. L. Prosvirnin, A. V. Rogacheva, Y. Chen, and N. I. Zheludev, “Asymmetric propagation of electromagnetic waves through a planar chiral structure,” *Phys. Rev. Lett.* **97**, 167401, (2006).
 13. A. S. Schwanecke, V. A. Fedotov, V. V. Khardikov, S. L. Prosvirnin, Y. Chen, and N. I. Zheludev, “Nanostructured metal film with asymmetric optical transmission,” *Nano Lett.* **8**, 2940-2943, (2008).
 14. R. Singh, E. Plum, C. Menzel, C. Rockstuhl, A. K. Azad, R. A. Cheville, F. Lederer, W. Zhang, and N. I. Zheludev, “Terahertz metamaterial with asymmetric transmission,” *Phys. Rev. B* **80**, 153104, (2009).
 15. C. Menzel, C. Helgert, C. Rockstuhl, E.-B. Kley, A. Tünnermann, T. Pertsch, and F. Lederer, “Asymmetric transmission of linearly polarized light at optical metamaterials,” *Phys. Rev. Lett.* **104**, 253902, (2010).

16. M. Mutlu, A. E. Akosman, A. E. Serebryannikov, and E. Ozbay, “Asymmetric transmission of linearly polarized waves and polarization angle dependent wave rotation using a chiral metamaterial,” *Opt. Express* **19**, 14290-14299, (2011).
17. M. Kang, J. Chen, H.-X. Cui, Y. Li, and H.-T. Wang, “Asymmetric transmission for linearly polarized electromagnetic radiation,” *Opt. Express* **19**, 8347-8356, (2011).
18. E. Plum, V. A. Fedotov, and N. I. Zheludev, “Asymmetric transmission: a generic property of two-dimensional periodic patterns,” *J. Opt.* **13**, 024006, (2011).
19. C. Huang, Y. Feng, J. Zhao, Z. Wang, and T. Jiang, “Asymmetric electromagnetic wave transmission of linear polarization via polarization conversion through chiral metamaterial structures,” *Phys. Rev. B* **85**, 195131, (2012).
20. M. Mutlu, A. E. Akosman, A. E. Serebryannikov, and E. Ozbay, “Diodelike asymmetric transmission of linearly polarized waves using magnetoelectric coupling and electromagnetic wave tunneling,” *Phys. Rev. Lett.* **108**, 213905, (2012).
21. J. Shi, X. Liu, S. Yu, T. Lv, Z. Zhu, H. F. Ma, and T. J. Cui, “Dual-band asymmetric transmission of linear polarization in bilayered chiral metamaterial,” *Appl. Phys. Lett.* **102**, 191905, (2013).
22. C. Pfeiffer, C. Zhang, Vishva Ray, L. J. Guo, and A. Grbic, “High performance bianisotropic metasurfaces: asymmetric transmission of light,” *Phys. Rev. Lett.* **113**, 023902, (2014).
23. S. Cakmakyapan, A. E. Serebryannikov, H. Caglayan, and E. Ozbay,

- “One-way transmission through the subwavelength slit in nonsymmetric metallic gratings,” *Opt. Lett.* **35**, 2597-2599, (2010).
24. J. Xu, C. Cheng, M. Kang, J. Chen, Z. Zheng, Y.-X. Fan, and H.-T. Wang, “Unidirectional optical transmission in dual-metal gratings in the absence of anisotropic and nonlinear materials,” *Opt. Lett.* **36**, 1905-1907, (2011).
 25. S. Cakmakyapan, H. Caglayan, A. E. Serebryannikov, and E. Ozbay, “Experimental validation of strong directional selectivity in nonsymmetric metallic gratings with a subwavelength slit,” *Appl. Phys. Lett.* **98**, 051103, (2011).
 26. E. Battal, T. A. Yogurt, and A. K. Okyay, “Ultrahigh contrast one-way optical transmission through a subwavelength slit,” *Plasmonics* **8**, 509, (2012).
 27. M. Stolarek, D. Yavorskiy, R. Kotyński, C. J. Z. Rodríguez, Jerzy Lusakowski, and T. Szoplik, “Asymmetric transmission of terahertz radiation through a double grating,” *Opt. Lett.* **38**, 839-841, (2013).
 28. Z. Cao, X. Qi, G. Zhang, and J. Bai, “Asymmetric light propagation in transverse separation modulated photonic lattices,” *Opt. Lett.* **38**, 3212-3215, (2013).
 29. A. E. Serebryannikov, E. Ozbay, and S. Nojima, “Asymmetric transmission of terahertz waves using polar dielectrics,” *Opt. Express* **22**, 3075-3088, (2014).
 30. T. Xu and H. J. Lezec, “Visible-frequency asymmetric transmission devices incorporating a hyperbolic metamaterial,” *Nat. Commun.* **5**, 4141, (2014).

31. C. Lu, X. Hu, Y. Zhang, Z. Li, X. Xu, H. Yang, and Q. Gong, "Ultralow power all-optical diode in photonic crystal heterostructures with broken spatial inversion symmetry," *Appl. Phys. Lett.* **99**, 051107, (2011).
32. C. Wang, C.-Z. Zhou, and Z.-Y. Li, "On-chip optical diode based on silicon photonic crystal heterojunctions," *Opt. Express* **19**, 26948-26955, (2011).
33. C. Lu, X. Hu, H. Yang, and Q. Gong, "Ultrahigh-contrast and wideband nanoscale photonic crystal all-optical diode," *Opt. Lett.* **36**, 4668-4670, (2011).
34. H. Kurt, D. Yilmaz, A. E. Akosman, and E. Ozbay, "Asymmetric light propagation in chirped photonic crystal waveguides," *Opt. Express* **20**, 20635-20646, (2012).
35. V. Liu, D. A. B. Miller, and S. Fan, "Ultra-compact photonic crystal waveguide spatial mode converter and its connection to the optical diode effect," *Opt. Express* **20**, 28388-28397, (2012).
36. V. Kuzmiak and A. A. Maradudin, "Asymmetric transmission of surface plasmon polaritons," *Phys. Rev. A* **86**, 043805, (2012).
37. C. Wang, X.-L. Zhong, and Z.-Y. Li, "Linear and passive silicon optical isolator," *Sci. Rep.* **2**, 674, (2012).
38. A. Cicek and B. Ulug, "Coupling between opposite-parity modes in parallel photonic crystal waveguides and its application in unidirectional light transmission," *Appl. Phys. B* **113**, 619, (2013).
39. S. Feng and Y. Wang, "Unidirectional reciprocal wavelength filters based on the square-lattice photonic crystal structures with the rectangular defects," *Opt. Express*, **21**, 220-228, (2013).

40. I. H. Giden, D. Yilmaz, M. Turduev, H. Kurt, E. Çolak, and E. Ozbay, “Theoretical and experimental investigations of asymmetric light transport in graded index photonic crystal waveguides,” *Appl. Phys. Lett.* **104**, 031116, (2014).
41. N. S. Nye, A. E. Halawany, A. Bakry, M. A. N. Razvi, A. Alshahrie, M. Khajavikhan, and D. N. Christodoulides, “Passive PT-symmetric metasurfaces with directional field scattering characteristics,” *IEEE J. Sel. Top. Quant.*, **22**, 5000608, (2016).
42. X. X. Liu, Y. Zhao, and A. Alù, “Nonlinearity-induced PT-symmetry without material gain,” *New J. Phys.* **18**, 065001, (2016).
43. M. Monticone, C. A. Valagiannopoulos, and A. Alù, “Aberration-free imaging based on parity-time symmetric nonlocal metasurfaces,” *Phys. Rev. X*, **6**, 041018, (2016).
44. A. V. Kildishev, A. Boltasseva, and V. M. Shalaev, “Planar photonics with metasurfaces,” *Science* **339**, 1232009, (2013).
45. F. Aieta, P. Genevet, M. A. Kats, N. Yu, R. Blanchard, Z. Gaburro, and F. Capasso, “Aberration-free ultrathin flat lenses and axicons at telecom wavelengths based on plasmonic metasurfaces,” *Nano Lett.* **12**, 4932-4936, (2012).
46. L. Huang, X. Chen, H. Mühlenbernd, G. Li, B. Bai, Q. Tan, G. Jin, T. Zentgraf, and S. Zhang, “Dispersionless phase discontinuities for controlling light propagation,” *Nano Lett.* **12**, 5750-5755, (2012).
47. G. Zheng, H. Mühlenbernd, M. Kenney, G. Li, T. Zentgraf, and S. Zhang, “Metasurface holograms reaching 80% efficiency,” *Nat. Nanotechnol.* **10**, 308-312, (2015).

48. E. Maguid, I. Yulevich, D. Veksler, V. Kleiner, M. L. Brongersma, and E. Hasman, "Photonic spin-controlled multifunctional shared-aperture antenna array," *Science* **352**, 1202, (2016).
49. S.-Y. Lee, K. Kim, G.-Y. Lee, and B. Lee, "Polarization-multiplexed plasmonic phase generation with distributed nanoslits," *Opt. Express* **23**, 15598-15607, (2015).
50. Z. H. Jiang, L. Lin, D. Ma, S. Yun, D. H. Werner, Z. Liu, and T. S. Mayer, "Broadband and wide field-of-view plasmonic metasurface-enabled waveplates," *Sci. Rep.* **4**, 7511, (2014).
51. J. M. Castro, D. F. Geraghty, S. Honkanen, C. M. Greiner, D. Iazikov, and T. W. Mossberg, "Demonstration of mode conversion using anti-symmetric waveguide Bragg gratings," *Opt. Express* **13**, 4180-4184, (2005).
52. E. Peral and A. Yariv, "Supermodes of grating-coupled multimode waveguides and application to mode conversion between copropagating modes mediated by backward Bragg scattering," *J. Lightwave Technol.* **17**, 942-947, (1999).
53. S.-Y. Tseng and M.-C. Wu, "Adiabatic mode conversion in multimode waveguides using computer-generated planar holograms," *IEEE Photon. Technol. Lett.* **22**, 1211-1213, (2010).
54. C.-S. Yeih, H.-X. Cao, and S.-Y. Tseng, "Shortcut to mode conversion via level crossing in engineered multimode waveguides," *IEEE Photon. Technol. Lett.* **26**, 123-126, (2014).
55. H. Zhang, Y. Li, N. Zhu, G. Jin, D. Zhang, and T. Mei, "Mode conversion in asymmetric dielectric/metal/dielectric plasmonic waveguide using

- grating coupler,” *Opt. Commun.* **310**, 217-221, (2014).
56. J. Kim, S.-Y. Lee, Y. Lee, H. Kim, and B. Lee, “Tunable asymmetric mode conversion using the dark-mode of three-mode waveguide system,” *Opt. Express* **22**, 28683-28696, (2014).
 57. V. Liu, D. A. B. Miller, and S. Fan, “Ultra-compact photonic crystal waveguide spatial mode converter and its connection to the optical diode effect,” *Opt. Express* **20**, 28388-28397, (2012).
 58. L. H. Frandsen, Y. Elesin, L. F. Frellsen, M. Mitrovic, Y. Ding, O. Sigmund, and K. Yvind, “Topology optimized mode conversion in a photonic crystal waveguide fabricated in silicon-on-insulator material,” *Opt. Express* **22**, 8525-8532 (2014).
 59. A. Y. Piggott, J. Lu, K. G. Lagoudakis, J. Petykiewicz, T. M. Babinec, and J. Vučković, “Inverse design and demonstrate of a compact and broadband on-chip wavelength demultiplexer,” *Nat. Photon.* **9**, 374-377, (2015).
 60. A. Yariv, “Couple-mode theory for guided-wave optics,” *IEEE J. Quantum Electron.* **9**, 919-933, (1973).
 61. H. A. Haus and W. Huang, “Coupled-mode theory,” in *Proc. IEEE* **79**, 1505-1518, (1991).
 62. H.-C. Liu and A. Yariv, “Grating induced transparency (GIT) and the dark mode in optical waveguides,” *Opt. Express* **17**, 11710-11718, (2009).
 63. H. Kim, J. Park, and B. Lee, *Fourier Modal Method and Its Applications in Computational Nanophotonics* (CRC, 2012).
 64. S. C. Rand, *Lectures on Light: Nonlinear and Quantum Optics using the*

Density Matrix (Oxford University Press, 2010).

65. J. Park, H. Kim, I.-M. Lee, S. Kim, J. Jung, and B. Lee, “Resonant tunneling of surface plasmon polariton in the plasmonic nano-cavity,” *Opt. Express* **16**, 16903-16915, (2008).
66. J. S. Q. Liu, J. S. White, S. Fan, and M. Brongersma, “Side-coupled cavity model for surface plasmon-polariton transmission across a groove,” *Opt. Express*, vol. 17, pp. 17837-17848, 2009.
67. M. Kuttge, F. J. García de Abajo, and A. Polman, “How grooves reflect and confine surface plasmon polaritons,” *Opt. Express* **17**, 10385-10392, (2009).
68. H. Kim, S.-Y. Lee, S. Koo, J. Kim, K. Park, D. Lee, L. A. Vazquez-Zuniga, N. Park, B. Lee, and Y. Jeong, “Theoretical study on the generation of a low noise plasmonic hotspot by means of a trench-assisted circular nano-slit,” *Opt. Express* **22**, 26844-26853, (2014).
69. R. Mehfuz, M. W. Maqsood, and K. J. Chau, “Enhancing the efficiency of slit-coupling to surface-plasmon-polaritons via dispersion engineering,” *Opt. Express* **18**, 18206-18216, (2010).
70. S.-Y. Lee, J. Park, I. Woo, N. Park, and B. Lee, “Surface plasmon beam splitting by the photon tunneling through the plasmonic nanogap,” *Appl. Phys. Lett.* **97**, 133113, (2010).
71. E. Palik, *Handbook of Optical Constants of Solids*, (Academic, 1998).

Appendix

Portions of the work discussed in this dissertation are also presented in the following publications:

[Chapter 2]

J. Kim, S.-Y. Lee, Y. Lee, H. Kim, and B. Lee, "Tunable asymmetric mode conversion using the dark-mode of three-mode waveguide system," *Optics Express*, vol. 22, no. 23, pp. 28683-28696, 2014.

[Chapter 3]

J. Kim, S.-Y. Lee, and B. Lee, "Near-complete radiation of plasmonic mode from nano-slit to free space," *Journal of Lightwave Technology*, vol. 34, no. 9, pp. 2251-2255, 2016.

J. Kim, S.-Y. Lee, H. Park, K. Lee, and B. Lee, "Reflectionless compact plasmonic waveguide mode converter by using a mode-selective cavity," *Optics Express*, vol. 23, no. 7, pp. 9004-9013, 2015

In addition, the author published the paper about slow light excitation:

J. Kim, S.-Y. Lee, H. Park, H. Kim, and B. Lee, "Slow surface plasmon pulse excitation in metal-insulator-metal plasmonic waveguide with chirped grating," *Optics Express*, vol. 22, no. 15, pp. 18464-18472, 2014.

초 록

본 논문에서는 도파로와 메타표면에서의 비대칭 광 모드 변환 현상에 대해 논한다. 좀 더 자세히는, i) 3 모드 도파로 시스템에서의 비대칭 모드 변환 특성 조절, ii) 단방향 플라즈모닉 모드 변환 장치의 소형화 그리고 iii) 이중형 메타표면에서의 단방향 편광 변환 성분 방출에 대해 설명한다.

첫째로, 모드 전이를 발생시키는 격자구조가 세 개의 도파로 모드가 존재하는 시스템에 새겨졌을 때, 로렌츠 역진성을 위배하지 않는 비대칭 모드 변환 특성을 설계하는 방법에 대해 제안한다. 특히, 원자의 암흑 상태에 해당되는 암흑 모드를 활용하여 광 입사 방향에 따른 비대칭 모드 변환 특성을 각각 독립적으로 설계할 수 있는 방법을 제시하였다. 먼저 암흑 모드가 도파로 모드 간 결합이 존재하는 상황에서도 모드 간 비율이 그대로 유지되는 성질을 활용하여 두 입사 방향 중 한 방향에 대한 투과 특성을 고정시킬 수 있음을 보였다. 이러한 성질을 활용하여 최종적으로 결합 세기 비율 조절을 통한 암흑 모드 설계와 격자 길이의 조절을 통해 모드 변환의 비대칭성을 조절할 수 있음을 보였다.

둘째로, 단방향 모드 변환 특성을 가지는 플라즈모닉 공간 광 모드 변환장치를 제안하였다. 모드 선택성 필터와 스텝형 모드 변환 장치의 조합을 통해 단방향 모드 변환 특성을 구현할 수 있었다. 여기서 더 나아가, 불필요한 산란 성분과 입사 포트로의 반사성분을 각각 모드 선택성 차단필터와 상쇄간섭을 통해 완전히 제거할 수 있음을 보였다. 이러한 설계방법의 활용사례로 파장보다

좁은 나노슬릿에서의 완전한 광 출사 안테나 설계문제를 제시하기도 하였다.

마지막으로, 편광 변환된 신호를 광 입사 방향으로만 방출하는 이층 메타표면 구조를 제안한다. 이층 메타표면 구조는 비교적 설계가 용이한 두 개의 얇은 메타표면 구조로 구성되며, 두 구조를 조합하는 방식으로 이층 구조를 설계하였다. 수치 해석을 통한 설계 이후, 설계된 소자를 실험적으로 제작하였고, 투과 및 반사 특성을 측정한 결과 제작된 구조의 반사율이 성공적으로 감소한 것을 확인하였다. 진폭 왜곡 현상과 이의 보상에 대한 문제도 다루어졌다.

암흑 모드를 이용한 비대칭 투과 소자는 비대칭 투과 특성 조절의 한 방법을 제시하는 것 이외에도 능동 비대칭성 조절 소자로의 발전에도 기여할 수 있을 것으로 생각된다. 나아가, 모드 선택성 필터를 이용한 비대칭 모드 변환장치 설계를 통해 나노광학에 적합한 수준으로 소형화하는 것도 가능할 것이다. 마지막으로 이층 메타표면 구조는 반사형 구조와 결합되어 투과단과 반사단의 멀티플렉싱에 이용될 수 있을 것으로 기대한다.

주요어: 광 모드 변환기, 메타표면, 로렌츠 역진성, 비대칭 광 모드 변환, 광 반사 제거, 멀티플렉싱, 편광.

학 번: 2012-20755